SPECTROSCOPIC INVESTIGATIONS OF SELECTED CYCLIC AND BICYCLIC MOLECULES

A Dissertation

by

KATHLEEN RAE MCCANN

Submitted to the Office of Graduate Studies of
Texas A&M University
in partial fulfillment of the requirements for the degree of

DOCTOR OF PHILOSOPHY

August 2009

Major Subject: Chemistry

SPECTROSCOPIC INVESTIGATIONS OF SELECTED CYCLIC AND BICYCLIC MOLECULES

A Dissertation

by

KATHLEEN RAE MCCANN

Submitted to the Office of Graduate Studies of
Texas A&M University
in partial fulfillment of the requirements for the degree of

DOCTOR OF PHILOSOPHY

Approved by:

Chair of Committee,	Jaan Laane
Committee Members,	Karl Aufderheide
	John Fackler
	Rand Watson
Head of Department,	David Russell

August 2009

Major Subject: Chemistry

ABSTRACT

Spectroscopic Investigations of Selected Cyclic and Bicyclic Molecules (August 2009)

Kathleen Rae McCann, B.S., Morningside College

Chair of Advisory Committee: Dr. Jaan Laane

Several cyclic molecules along with two bicyclic molecules were investigated using infrared (IR), Raman, ultraviolet (UV) absorption, fluorescence excitation (FES), and single vibronic level fluorescence (SVLF) spectroscopies.

The laser-induced fluorescence spectra (both fluorescence excitation and single vibronic level fluorescence) of jet-cooled 1,3-benzodioxan (13BZN) along with its ultraviolet absorption spectra have been recorded and analyzed in order to determine the vibrational quantum levels in both the ground and $S_1(\pi,\pi^*)$ electronic excited states. A detailed energy map was established and utilized to better understand the structural and conformational differences between the ground and excited electronic states. *Ab initio* and DFT calculations were also carried out to complement the experimental work. The data allowed one-dimensional potential energy functions in terms of the ring-twisting coordinate to be calculated.

A complete study of all of the vibrations of 13BZN in both its S_0 ground and $S_1(\pi,\pi^*)$ excited state was done utilizing several types of spectral data including infrared and Raman spectra. The vibrational frequencies of 13BZN were compared to those of the very similar 1,4-benzodioxan.

The Raman and infrared spectra of dipicolinic acid (DPA), a component of anthrax spores, and dinicotinic acid (DNic) and their salts (CaDPA, Na_2DPA, and CaDNic) have been recorded and the spectra have been assigned. *Ab initio* and DFT calculations were carried out to predict the structures and vibrational spectra and were compared to the experimental results. Theoretical calculations were also carried out for DPA dimers and DPA+2H_2O to better understand the intermolecular interactions.

3-Methylindole (3MI), which serves as a structural model for the tryptophan side chain in proteins, has been investigated using vapor phase Raman spectroscopy. The vapor phase spectrum of 3MI complements previously reported Raman studies of 3MI solutions and related tryptophan derivatives. The analysis of the Raman spectrum of 3MI vapor was also supported here with newly obtained vapor phase infrared data and *ab initio* calculation to refine previous vibrational assignments. The present results provide an improved basis for assessing the dependence on the indoyl Raman signature on the local environment of the tryptophan side chain of proteins.

ACKNOWLEDGEMENTS

The first person I need to thank is my research advisor, Dr. Jaan Laane, for all of his support and guidance through the years. Also, Dr. Karl Aufderheide, Dr. John P. Fackler, and Dr. Rand Watson deserve thanks as members of my committee.

Several people have my appreciation for their assistance in obtaining data. The 3-methylindole work was carried out in part by Amanda Combs, a summer NSF REU student. In addition, Daniel Autrey assisted with some of the experiments and Professor George J. Thomas, Jr. (University of Missouri, Kansas City) contributed to the analysis of the data. The Raman microscope data would have not been obtained if not for Hye-Jin Chun's proficiency.

Dr. John Villareal has my gratitude for the synthesis of 1,3-benzodioxan and Dr. Jaebum Choo for calculations of its excited state.

TABLE OF CONTENTS

Page

ABSTRACT iii

ACKNOWLEDGEMENTS v

TABLE OF CONTENTS vi

LIST OF FIGURES viii

LIST OF TABLES xi

CHAPTER

I INTRODUCTION 1

1,3-Benzodioxan 1
Dipicolinic Acid, Dinicotinic Acid, and Their Dianions 2
3-Methylindole 3

II EXPERIMENTAL 4

Infrared Spectra 4
Raman Spectra 4
Raman Microscope 6
Ultraviolet Absorption Spectra 6
Fluorescence Excitaiton and Single Vibronic Level Fluorescence Spectra 7

III SPECTROSCOPIC INVESTIGATIONS AND POTENTIAL ENERGY SURFACES OF THE GROUND AND EXCITED ELECTRONIC STATES OF 1,3-BENZODIOXAN 8

Introduction 8
Experimental Methods 9
Calculations 10
Assignment of Spectra 13
Vibrational Potential Energy Surface 29
Discussion 34

CHAPTER Page

IV VIBRATIONAL SPECTRA AND THEORETICAL CALCULATIONS OF 1,3-BENZODIOXAN IN ITS GROUND AND EXCITED ELECTRONIC STATES 37

Introduction 37
Experimental 37
Calculations 38
Molecular Structure 38
Results and Discussion 40
Conclusions 46

V RAMAN AND INFRARED SPECTRA AND THEORETICAL CALCULATIONS OF DIPICOLINIC ACID, DINICOTINIC ACID, AND THEIR DIANIONS 47

Introduction 47
Experimental 49
Calculations 50
Structures 50
Vibrational Modes 54
Vibrational Spectra 57
Spectroscopic Effects of Molecular Interactions 73
Conclusions 79

VI RAMAN SIGNATURE OF THE NON-HYDROGEN-BONDED TRYPTOPHAN SIDE CHAIN IN PROTEINS: EXPERIMENTAL AND *AB INITIO* SPECTRA OF 3-METHYLINDOLE IN THE GAS PHASE 82

Introduction 82
Materials and Methods 86
Results 87
Discussion and Conclusions 95

VII CONCLUSIONS 98

REFERENCES 100

VITA 106

LIST OF FIGURES

FIGURE		Page
1	Spectroscopic techniques	5
2	Calculated structures for 13BZN in its ground (left) and $S_1(\pi,\pi^*)$ excited (right) states. The twisting angles for the five-membered ring are calculated to 31° for S_0 and 24° for S_1.	11
3	Fluorescence excitation spectrum of jet-cooled 13BZN.	15
4	Ultraviolet absorption spectrum of 13BZN in a 15 cm cell at 25 °C compared to the FES and relative to the 0_0^0 band.	18
5	SVLF spectra of 13BZN from several excitation bands.	21
6	Energy levels for the low-frequency vibrations of 13BZN in its ground and $S_1(\pi,\pi^*)$ excited states.	27
7	Potential energy functions for the ring-twisting of 13BZN in its S_0 and $S_1(\pi,\pi^*)$ states	33
8	Skeletal structures of 13BZN in its S_0 and $S_1(\pi,\pi^*)$ electronic states.	39
9	Experimental and calculated infrared spectra of 13BZN.	41
10	Experimental and calculated Raman spectra of 13BZN.	42
11	Calculated structures for DPA and the DPA^{-2} anion using B3LYP/ 6-311++G(d,p). Geometrical parameters from the crystal structures of anhydrous DPA and DPA monohydrate are shown in parentheses and brackets, respectively.	51
12	Calculated structures for DNic and the $DNic^{-2}$ anion. Values in parentheses are from the crystal structure.	52
13A	Vector representation for the A_1 and A_2 vibrations of DPA based on C_{2v} symmetry	55

FIGURE Page

13B Vector representation for the B_1 and B_2 vibrations of DPA based on C_{2v} symmetry..... 56

14A Vector representation for the A_1 and A_2 vibrations of the DPA^{-2} anion based on C_{2v} symmetry 58

14B Vector representation for the B_1 and B_2 vibrations of the DPA^{-2} anion based on C_{2v} symmetry. 59

15 Raman spectrum of DPA powder compared to its computed spectrum..... 60

16 Infrared spectrum of DPA in a KBr pellet compared to its computed spectrum. 61

17 Raman spectra of the calcium and sodium salts of DPA^{-2} compared to the computed spectrum of free DPA^{-2}. 62

18 Infrared spectra of the calcium and sodium salts of DPA^{-2} compared to the computed spectrum of free DPA^{-2}. 63

19 Raman spectrum of DNic powder compared to its computed spectrum.... 64

20 Infrared spectrum of DNic in a KBr pellet compared to its computed spectrum 65

21 Raman spectrum of the calcium salt of $DNic^{-2}$ compared to the computed spectrum of free $DNic^{-2}$ 66

22 Infrared spectrum of the calcium salt of $DNic^{-2}$ compared to the computed spectrum of free $DNic^{-2}$. 67

23 Comparison of the DPA and DNic experimental Raman spectra 74

24 Comparison of the DPA and DNic experimental infrared spectra..... 75

25 Comparison of the DPA^{-2} and $DNic^{-2}$ calcium salt Raman spectra 76

26 Comparison of the DPA^{-2} and $DNic^{-2}$ calcium salt infrared spectra..... 77

27 Structures of 3-methylindole (left) and tryptophan (right). The numbering of ring and exocyclic atoms follows IUPAC-IUPAB nomenclature. 85

FIGURE Page

28 Raman spectra of 3-methylindole in the region 200-3600 cm^{-1}. (A) Neat liquid (melt at 100 °C). (B) Vapor at 300 °C. (C) Calculated (*ab initio*) using B3LYP/6-311++G**. 89

29 Calculated molecular structure of 3-methylindole using B3LYP/ 6-311++G** 91

30 Raman spectra of 3-methylindole in the region 1300-1375 cm^{-1} showing the Fermi doublet (mode *W7*). Experimental data (solid line) and curve fits of the deconvolved data for the neat liquid at 100 °C and vapor at 300 °C are shown in the top and bottom panels, respectively. Data are from Figures 28A and 28B 93

LIST OF TABLES

TABLE		Page
1	Calculated barriers to planarity of 1,3-BZD from different basis sets.	12
2	Experimental and calculated vibrational frequencies and assignments for 1,3-benzodioxan in its S_0 ground and S_1 excited states.	14
3	Fluorescence excitation spectra (cm^{-1}) of 1,3-benzodioxan.....	16
4	Hot band combinations of 1,3-benzodioxan in the ultraviolet absorption spectra.....	20
5	Single vibronic level fluorescence (SVLF) frequencies and assignments from various excitation bands of 1,3-benzodioxan.....	22
6	Low-frequency vibrations (cm^{-1}) of 1,3-benzodioxan	28
7	Observed and calculated ring-twisting energy levels (cm^{-1}) for 13BZN in its ground and $S_1(\pi,\pi^*)$ excited states.	32
8	Barriers to planarity (kcal/mole) and bending and twisting frequencies (cm^{-1}) of tetralin and its oxygen analogs.....	35
9	Experimental and calculated vibrational frequencies and assignments for 1,3-benzodioxan in its S_0 ground and S_1 excited states.	43
10	Calculated (scaled) and observed frequencies (cm^{-1}) for solid DPA and solid DNic.	69
11	Calculated (scaled) and observed frequencies (cm^{-1}) for solid CaDPA, solid Na_2DPA and solid CaDNic.	71

TABLE Page

12 Reported infrared spectra (cm^{-1}) of pyridinedicarboxylic acids 78

13 Calculated frequencies (cm^{-1}) of DPA in different environments 80

14 Experimental and calculated vibrational frequencies of 3-methylindole... 88

15 Raman solution spectra frequencies of the *W7* band..... 94

CHAPTER I

INTRODUCTION

Molecular spectroscopy has been a powerful tool for nearly a century for a better understanding of molecular bonding and molecular structures. It has also been invaluable for identifying and detecting a large variety of molecules including those in organic, inorganic, and biochemical systems.

In this work three different investigations were undertaken using several different kinds of spectroscopy. First, 1,3-benzodioxan (13BZN) was investigated in both its ground and electronic excited states using infrared, Raman, ultraviolet absorption, and laser induced fluorescence (LIF) spectroscopies. The aim was to determine potential energy functions which would elucidate the structure and energetics of this molecule. Second, dipicolinic acid and its salts, which are present in anthrax spores, were studied using infrared and Raman spectra in order to better find ways of identifying their presence in biological spores. Third, 3-methylindole, which is a model compound for tryptophan, was investigated by Raman spectroscopy to better understand the spectra arising in larger chemical systems.

1-3-BENZODIOXAN

1,3-Benzodioxan (13BDX) will be studied to gain a greater understanding of the structure and bonding forces in the ground S_0 state and the excited S_1 state and

---

This dissertation follows the style of The Journal of Chemical Physics.

understanding the differences between the two states. Laser-induced fluorescence and ultraviolet absorption spectra along with infrared and Raman spectra will be recorded to aid in the study of the low-frequency vibrations and conformational energetics of 13BZN. These results for 13BZN will be compared to those of 1,4-benzodioxan (14BZD) which contains $–CH_2-CH_2-$ torsional interactions but lacks the $[O-CH_2-O]$ linkage present in 13BZN which is expected to show the anomeric effect. The experimental data on 13BDX will be complemented by *ab initio* and DFT calculations. Additionally, the data acquired from the laser-induced fluorescence spectra and infrared and Raman spectra will be used along with *ab initio* and DFT calculations to present a comprehensive study of all of the S_0 ground and S_1 excited state vibrations of 13BZN.

DIPICOLINIC ACID, DINICOTINIC ACID, AND THEIR DIANIONS

Dipicolinic acid (DPA) and calcium dipicolinate (CaDPA) make up a significant portion of the anthrax spore. With the recent renewal of interest in bioterrorism and prevention many scientists are looking for quick, accurate methods to detect chemicals of interest. In the case of the anthrax spore, the end result would be a spectroscopic detector for anthrax contamination to replace current methods.

The study of dinicotinic acid (DNic) and its dianion will be undertaken to show how these very similar molecules are able to be distinguished spectroscopically from DPA and its dianion. In order to show this Raman and infrared spectra of DPA, DNic, and their dianions in the solid state will be collected and then compared to the

corresponding molecule as well as to calculated spectra. In addition, this data will be used to construct a comprehensive vibrational assignment of DPA, DNic and their dianions. Theoretical calculations of a DPA dimer and a DPA-water complex will also be undertaken to help understand the affect these environments can have on DPA and its vibrations.

3-METHYLINDOLE

3-Methylindole (3MI) will be studied as a model compound for tryptophan. Raman vapor spectra, approximating an environment free of intermolecular interactions, will be compared with Raman liquid spectra to determine which vibrational bands serve as indicators of a changing indolyl ring environment. Infrared and Raman spectra will be used to refine, if needed, previously reported vibrational assignments of 3MI. The Fermi doublet intensity ratio provides a way to quantify the environmental effect on the spectra of 3MI. Raman spectra of 3MI in various solvents will be collected to extend previous results as well as provide quantification for differing environments of the indolyl ring.

CHAPTER II

EXPERIMENTAL

The experimental spectroscopic techniques used in the following chapters are shown in Figure 1. Three of the techniques, infrared (IR), Raman, and single vibronic level fluorescence (SVLF) spectroscopy, are used for the determination of vibrational energy levels in the electronic ground state. Information on the vibronic energy levels of the electronic excited state is provided by ultravioled (UV) absorbtion and fluorescence excitation (FES) spectroscopy.

INFRARED SPECTRA

Infrared spectra were recorded on a Bomem DA8.02 or a BioRad FTS-60 or a Bruker Vertex 60 instrument. Vapor phase spectra at were recorded using a heatable 10 cm metal cell with KBr windows. Spectra of the solid samples as both Nujol mulls between KBr plates and as KBR pellets were recorded at 25 °C.

RAMAN SPECTRA

Raman spectra were collected on a Jobin Yvon U-1000 spectrometer (Instruments S. A., Edison, NJ). A Coherent Innova 20 argon ion laser (514.5 nm) or a Coherent Verdi V-10 Nd:YAG system (532 nm) was used for excitation. Vapor-phase spectra of approximately 1 atm of sample were obtained using a custom-designed

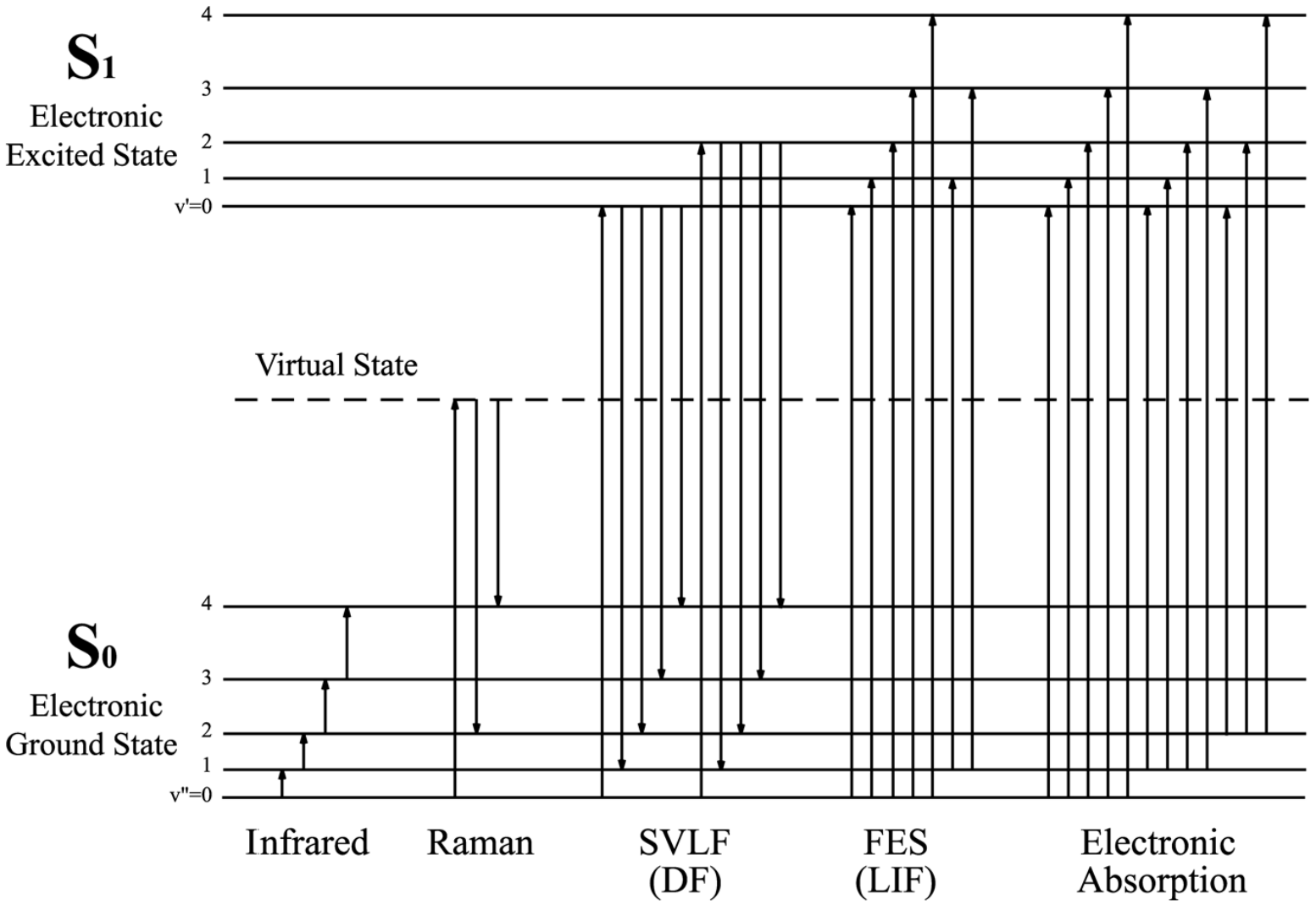

Figure 1. Spectroscopic techniques.

thermostatically controlled Raman cell[1] into which solid sample was transferred; the Raman cell was subsequently frozen with liquid nitrogen and sealed after evacuation on a vacuum line. Liquid phase spectra were obtained in a glass tube. Solution spectra were recorded using cuvettes to contain the samples. Either a charge-coupled device or a photomultiplier tube was used for detection of the Raman scattered light. The Raman spectra were collected and processed using standard software packages (SpectraMax, LabSpec, and BomemGrams).

RAMAN MICROSCOPE

Raman spectra were also recorded with a JY Horiba LabRam HRFTIR microscope equipped with CCD detection with spectral resolution of 0.3 cm^{-1}/pixel at 680 nm. A helium-neon laser operating at 633 nm with 17 mw of power was the excitation source.

ULTRAVIOLET ABSORBTION SPECTRA

Ultraviolet absorption spectra were recorded on a Bomem DA8.02 Fourier-transform spectrometer using a deuterium lamp source, a quartz beamsplitter, and a silicon detector in the 30,000-40,000 cm^{-1} region. The vapor-phase sample was contained in a 20 cm glass cell with quartz windows. Ultraviolet absorption spectra were collected at ambient temperatures and the vapor pressure within the cell was about 0.2 Torr. Resolutions of 0.25 and 0.5 cm^{-1} were used and five to ten thousand scans were typically averaged.

FLUORESCENCE EXCITATION AND SINGLE VIBRONIC LEVEL FLUORESCENCE SPECTRA

The fluorescence excitation spectra (FES) and the single vibronic level fluorescence (SVLF) spectra were recorded under jet-cooled conditions using a Continuum Powerlite 9020 Nd:YAG laser which pumped a Continuum Sunlite OPO and FX-1 ultraviolet extension unit. FES spectra were obtained at 0.5 cm^{-1} resolution and SVLF spectra were taken with a spectral resolution of 1 cm^{-1}.

CHAPTER III

SPECTROSCOPIC INVESTIGATIONS AND POTENTIAL ENERGY SURFACES OF THE GROUND AND EXCITED ELECTRONIC STATES OF 1,3-BENZODIOXAN

INTRODUCTION

For more than forty years the Laane research group has been investigating the potential energy surfaces for large-amplitude vibrations which govern the conformational properties of molecules.[2-6] Initially, far-infrared and low-frequency Raman spectroscopy were used to determine the excited vibrational quantum states in electronic ground states, but later the focus turned to electronic excited states utilizing fluorescence spectroscopy of jet-cooled molecules along with ultraviolet absorption spectroscopy. In recent years the group has investigated a number of bicyclic molecules containing the benzene ring including tetralin[7] (TET) and 1,4-benzodioxan[8] (14BZD). In our present study we will report our results for 1,3-benzodioxan (13BZN). This molecule has

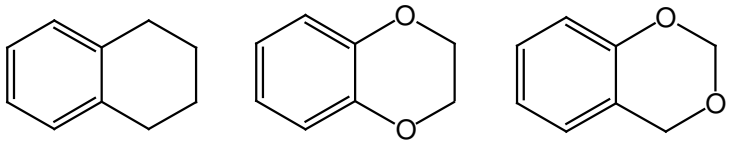

TET 14BZD 13BZN

been more difficult to analyze due to its reduced symmetry, but it is also more interesting in that it is expected to show the anomeric effect which is present in molecules which possess a –O–CH_2–O– linkage. As has been demonstrated

previously,[9-11] the anomeric effect results in a strong torsional force tending to twist or bend the molecular structure.

In the previous work a combination of spectroscopic data and DFT calculations on 14BZD showed the molecule to be twisted with barriers to planarity of 5000 ± 2000 cm^{-1} for the S_0 ground state and 3600 ± 2000 cm^{-1} for the $S_1(\pi,\pi^*)$ excited state.[8] The bent conformations of intermediate energy correspond to saddle points allowing hindered pseudorotation about the two-dimensional surface. The large uncertainties were present since the spectroscopic data extend to less than 1000 cm^{-1} above the vibrational ground state. For TET the barriers to planarity were determined to be 6000 ± 2000 cm^{-1} for the S_0 state and 4000 ± 2000 cm^{-1} for the S_1 state.[7] The bent conformation was calculated to be only 716 cm^{-1} higher in energy than the twisted conformation. The differences between the 14BZD and TET potential energy surfaces resulted primarily from two additional $–CH_2–CH_2–$ torsional interactions which were not present for 14BZD. In the present study of 13BZN no $–CH_2$-CH_2- torsional interactions are present, but the contribution from the anomeric effect is expected to be substantial.

EXPERIMENTAL METHODS

The sample of 1,3-benzodioxan was prepared at the University of Texas-Pan American according to the method of Chattaway and Irving.[12] It has a boiling point of 211° (60° at 5 Torr). Ultraviolet absorption spectra were recorded on a Bomem DA8.02 Fourier-transform spectrometer using a deuterium lamp source, a quartz beamsplitter, and a silicon detector in the 30,000-40,000 cm^{-1} region. The vapor-phase sample was

contained in a 20 cm glass cell with quartz windows. Ultraviolet absorption spectra were collected at ambient temperatures and the vapor pressure within the cell was about 0.2 Torr. Resolutions of 0.25 and 0.5 cm^{-1} were used and five to ten thousand scans were typically averaged. The fluorescence excitation spectra (FES) and the single vibronic level fluorescence (SVLF) spectra were recorded using a Continuum Powerlite 9020 Nd:YAG laser which pumped a Continuum Sunlite OPO and FX-1 ultraviolet extension unit. FES spectra were obtained at 0.5 cm^{-1} resolution and SVLF spectra were taken with a spectral resolution of 1 cm^{-1}. Both spectra were recorded under jet-cooled conditions. More details are provided elsewhere.[2-8] Infrared spectra of the liquid film between KBr plates were recorded on a Bruker Vertex 60 and Raman spectra of the liquid in a glass tube were recorded using a JY U-1000 spectrometer and a Coherent Verdi-10 laser operating at 532 nm.

CALCULATIONS

Theoretical calculations were carried out using the GAUSSIAN 03 package.[13] For the excited state, TURBOMOLE was used for calculations. The bond distances and bond angles were calculated for the ground state S_0 structure using the B3LYP/6-311+G(d,p) basis set and for the $S_1(\pi,\pi^*)$ excited state using the CIS/6-311+G(d,p) basis set are shown in Figure 2. Table 1 lists the calculated barriers to planarity from different basis sets for 13BZN in its S_0 and $S_1(\pi,\pi^*)$ states relative to the energy minima at the twisted conformations.

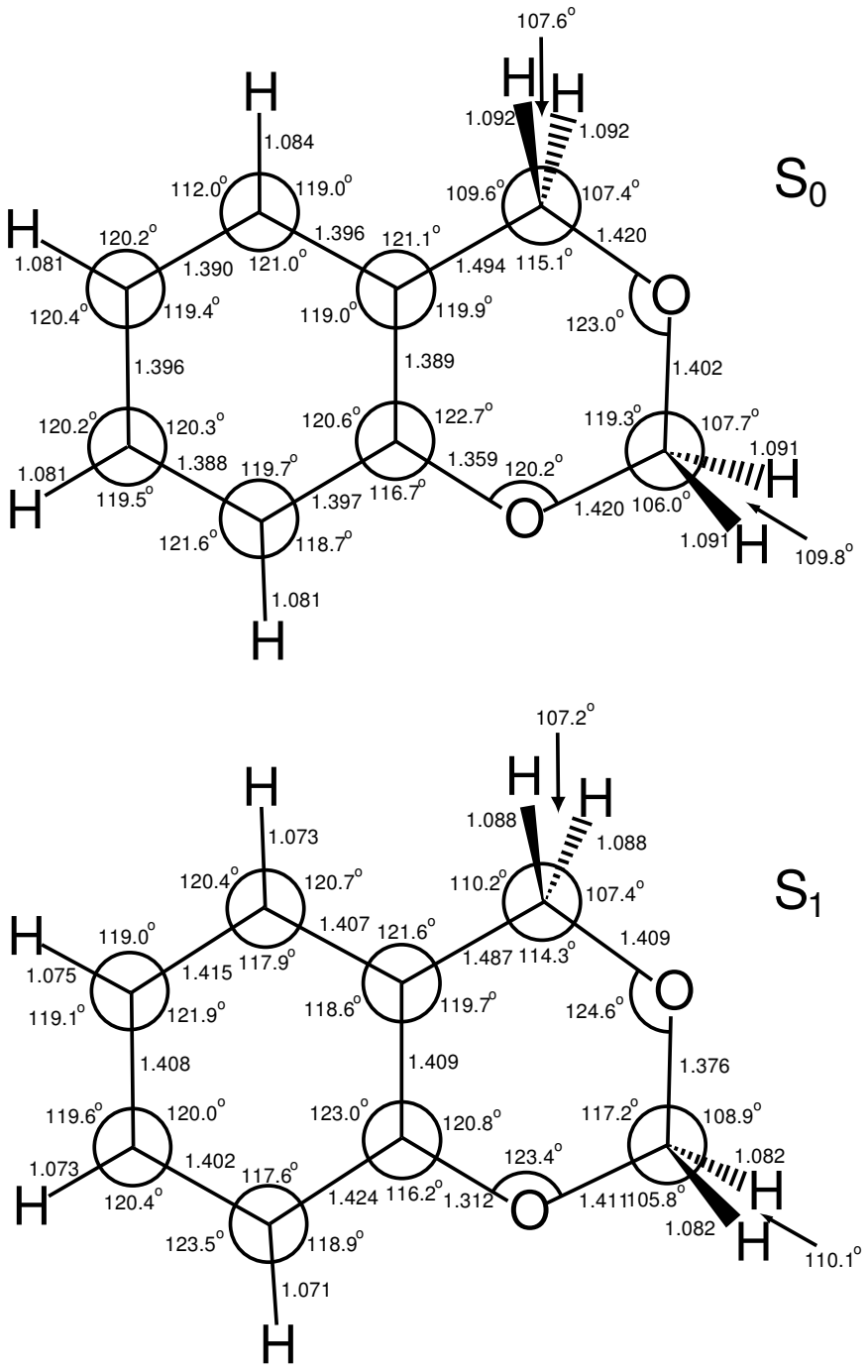

Figure 2. Calculated structures for 13BZN in its ground (left) and $S_1(\pi,\pi^*)$ excited (right) states. The twisting angles for the five-membered ring are calculated to be 33° for S_0 and 24° for S_1.

Table 1. Calculated barriers to planarity of 1,3-BZN from different basis sets.

Basis Set	S_0		S_1[a]	
	kcal/mole	kJ/mole	kcal/mole	kJ/mole
HF/6-31G(d)	9.63	40.3	8.92	37.3
HF/6-31+G(d)	9.83	41.1	9.12	38.2
HF/6-31+G(d,p)	9.81	41.0	9.08	38.0
HF/6-311+G(d,p)	10.05	42.0	9.29	38.9
MP2/cc-pVTZ	12.28	51.4	-	-

[a)] Computed using the CIS method.

The twisting angle τ and the bending angle θ used for the calculations for the potential energy surfaces (PESs) were defined previously[8] for 14BZD. The vibrational frequencies for the S_0 ground state were calculated by DFT methods using the B3LYP/6-311++G(d,p) basis set. A scaling factor[14] of 0.984 was used for frequencies below 2000 cm^{-1} and 0.964 for those above 2800 cm^{-1}. For the $S_1(\pi,\pi^*)$ excited state the CIS/6-311+G(d,p) basis set was utilized. The scaling factor of 0.94 for excited state frequencies below 2000 cm^{-1} was determined by adjusting it to best match the calculated frequencies to the observed experimental values. For frequencies above 2800 cm^{-1} a scaling factor of 0.90 was used.

ASSIGNMENT OF SPECTRA

To aid with the discussion to follow, Table 2 provides a listing of the vibrations of 13BZN according to both C_s (planar) and C_1 (twisted) symmetry. The A' modes in C_s symmetry correspond to the in-plane vibrations while the A" are out-of-plane modes. The vibrational numbering for C_1 will be utilized for the discussion to follow. The table also lists the vibrational frequencies for the S_0 ground state, based on the infrared and Raman data given in Chapter IV, and for the S_1 excited state based on the results here. Figure 3 shows the fluorescence excitation spectrum (FES) of jet-cooled 13BZN and Table 3 lists the observed bands up to 800 cm^{-1}. Additional data can be found in Chapter IV. The observed ultraviolet absorption spectrum of 13BZN near the band origin is shown in Figure 4 where it is also compared to the FES in this region. The absorption

Table 2. Experimental and calculated vibrational frequencies and assignments for 1,3-benzodioxan in its S_0 ground and S_1 excited states.

			Description	Wavenumber (cm^{-1})					Description	Wavenumber (cm^{-1})	
	C_s	C_1		S_0[a]	S_1[b]		C_s	C_1		S_0[a]	S_1[b]
A’	1	1	C-H sym. stretch	3081	[3047]	A’	26	35	Benzene stretch	756	722
	2	2	C-H stretch	[3072]	[3028]		27	37	Benzene ring bend	712	682
	3	3	C-H stretch	3060 R	[3020]		28	39	Benzene ring bend	588	525
	4	4	C-H stretch	3031 R	[3005]		29	41	Sat. ring bend	520	482
	5	7	CH_2 sym. stretch (ip)	[2868]	[2855]		30	42	Sat. ring bend	464	442
	6	8	CH_2 sym. stretch (op)	2862	[2765]		31	44	Sat. ring bend	369 R	345
	7	9	Benzene stretch	1614	[1665]						
	8	10	Benzene stretch	1587	[1608]	A’’	32	5	CH_2 antisym. stretch	3012	[2994]
	9	11	Benzene stretch	1503 F	[1559]		33	6	CH_2 antisym. stretch	2957	[2892]
	10	12	CH_2 deformation (ip)	1492	[1528]		34	19	CH_2 twist	1275	[1329]
	11	13	CH_2 deformation (op)	1479 R	[1507]		35	21	CH_2 twist	1232	[1265]
	12	14	Benzene stretch	1460	[1481]		36	25	CH_2 rock	1100	[1111]
	13	15	CH_2 wag	1409	[1460]		37	29	CH_2 rock	994	[1008]
	14	16	CH_2 wag	1359	[1405]		38	30	C-H wag	[965]	[987]
	15	17	CH_2 twist	1309	[1381]		39	31	C-H wag	949 R	[890]
	16	18	CH_2 twist	1291	[1341]		40	34	C-H wag	851 F	[744]
	17	20	Sat. ring stretch	1238	[1277]		41	36	C-H wag	752	[635]
	18	22	C-H wag *	1210	[1234]		42	38	Benzene ring bend	698	[574]
	19	23	C-H wag	1157 R	[1186]		43	40	Benzene ring bend	536	374
	20	24	C-H wag	1150	[1160]		44	43	Benzene ring bend	435	255
	21	26	Sat. ring stretch	1079	[1071]		45	45	Sat. ring twist	356 R	339
	22	27	Sat. ring stretch	1035	[1051]		46	46	Sat. ring flap	284 R	194
	23	28	Ring stretch *	1011	[1023]		47	47	Sat. ring twist	178 R	102
	24	32	Sat. ring stretch	[934]	[865]		48	48	Sat. ring bend	108 F	96
	25	33	Benzene ring bend	853	[750]						

[a] Values from IR unless indicated. R=Raman values, F = SVLF values, [ ] = calculated values using b3lyp/6-311++G(d,p); scaling factors are 0.985 for vibrations below 2800 cm^{-1} and 0.964 for vibrations above 2800 cm^{-1}.

[b] Values from FES unless indicated. [ ] = calculated values using CIS/6-311++G(d,p); scaling factor are 0.940 for vibrations below 2800 cm^{-1} and 0.900 for vibrations above 2800 cm^{-1}.

* Coupled vibrations.

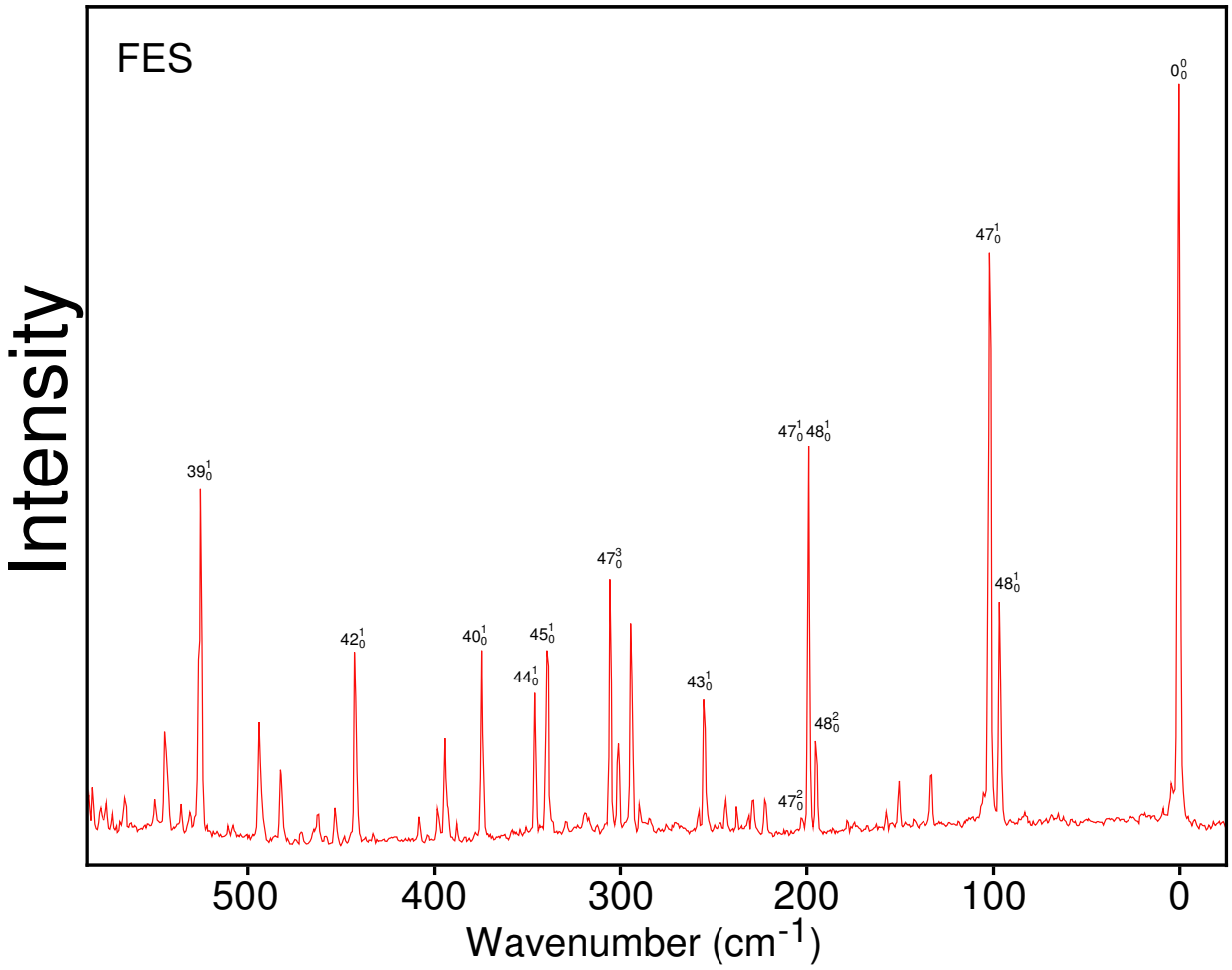

Figure 3. Fluorescence excitation spectrum of jet-cooled 13BZN. Wavenumbers are relative to the band origin at 38,885.6 cm^{-1}.

Table 3. Fluorescence excitation spectra (cm^{-1}) of 1,3-benzodioxan.

FES[a]		UV		Inferred [b]	Assignment	SVLF match [c]		Calc.[d]
0.0	(100)	0.0	vs	0.0	0_0^0			
96.3	(24)	96.0	mw		48_0^1	108.4	48_1^0	98
101.7	(64)	101.9	m		47_0^1	158.5	47_1^0	111
194.9	(7)	194.0	vw		46_0^1	274.4	46_1^0	192
199.1	(44)	199.5	m	198.0	$47_0^1 48_0^1$	316.8	47_2^0	
202.8	(2)			203.4	47_0^2			
255.0	(15)	255.7	vw		43_0^1	430.4	43_1^0	231
284.3	(1)							
		286.6	vw		48_0^3			
289.7	(2)	290.0	vw	291.2	$46_0^1 48_0^1$			
294.1	(26)	294.6	w	296.6	$46_0^1 47_0^1$			
301.1	(9)	301.3	vw	299.1	$47_0^2 48_0^1$			
305.6	(29)	305.9	vw	305.1	47_0^3			
339.0	(21)	338.9	w		45_0^1	351.2	45_1^0	192
345.0	(16)	345.4	vw		44_0^1	361.2	44_1^0	353
374.3	(22)	373.3	vw		40_0^1	535.1	40_1^0	375
387.6	(2)			389.8	46_0^2			
394.1	(12)	393.4	vw	392.9	$46_0^1 47_0^1 48_0^1$			
397.9	(3)			397.7	$46_0^1 47_0^2$			
403.4	(1)							
407.8	(2)	407.8	vw	405.6/406.8	47_0^4			
441.9	(21)	441.7	vw		42_0^1	461.3	42_1^0	451
452.4	(4)	452.4	w	453.0	$43_0^1 47_0^1 48_0^1$			
461.8	(3)							
471.3	(1)	471.6	vw	481.5	48_0^5			
482.1	(8)	481.9	w		41_0^1	519.4	41_1^0	502
493.6	(13)	492.5	w					
507.7	(1)	506.7	vw					
510.3	(1)	510.0	vw					
525.2	(39)	524.7	m		39_0^1	587.3	39_0^1	521
543.5	(11)	543.3	w					
594.5	(9)	594.2	vw					
596.5	(7)	596.5	vw					
621.1	(7)							
626.9	(14)							

Table 3. Continued.

FES[a]		UV		Inferred [b]	Assignment	SVLF match [c]		Calc.[d]
659.3	(3)	659.7	w					
663.7	(1)	663.3	vw					
676.3	(41)	676.1	mw		45_0^2			
681.8	(3)				37_0^1	711.9	37_1^0	672
691.9	(2)							
705.8	(1)	706.4	m					
719.3	(36)	719.3	mw					
722.1	(80)	721.3	m		35_0^1	752.8	35_1^0	697
726.0	(11)	726.2	vw					
728.7	(23)	728.4	vw					
781.1	(16)							

s- strong; m-medium; w-weak; v-very

[a] Relative to 0_0^0 band at 38,885.6 cm^{-1}; relative intensities are given in parentheses

[b] Calculated from other transitions

[c] Correlation to strongest SVLF band from excitation of S_1 state

[d] Calculated at the CIS/6-311++G** level; a scaling factor of 0.94 was used.

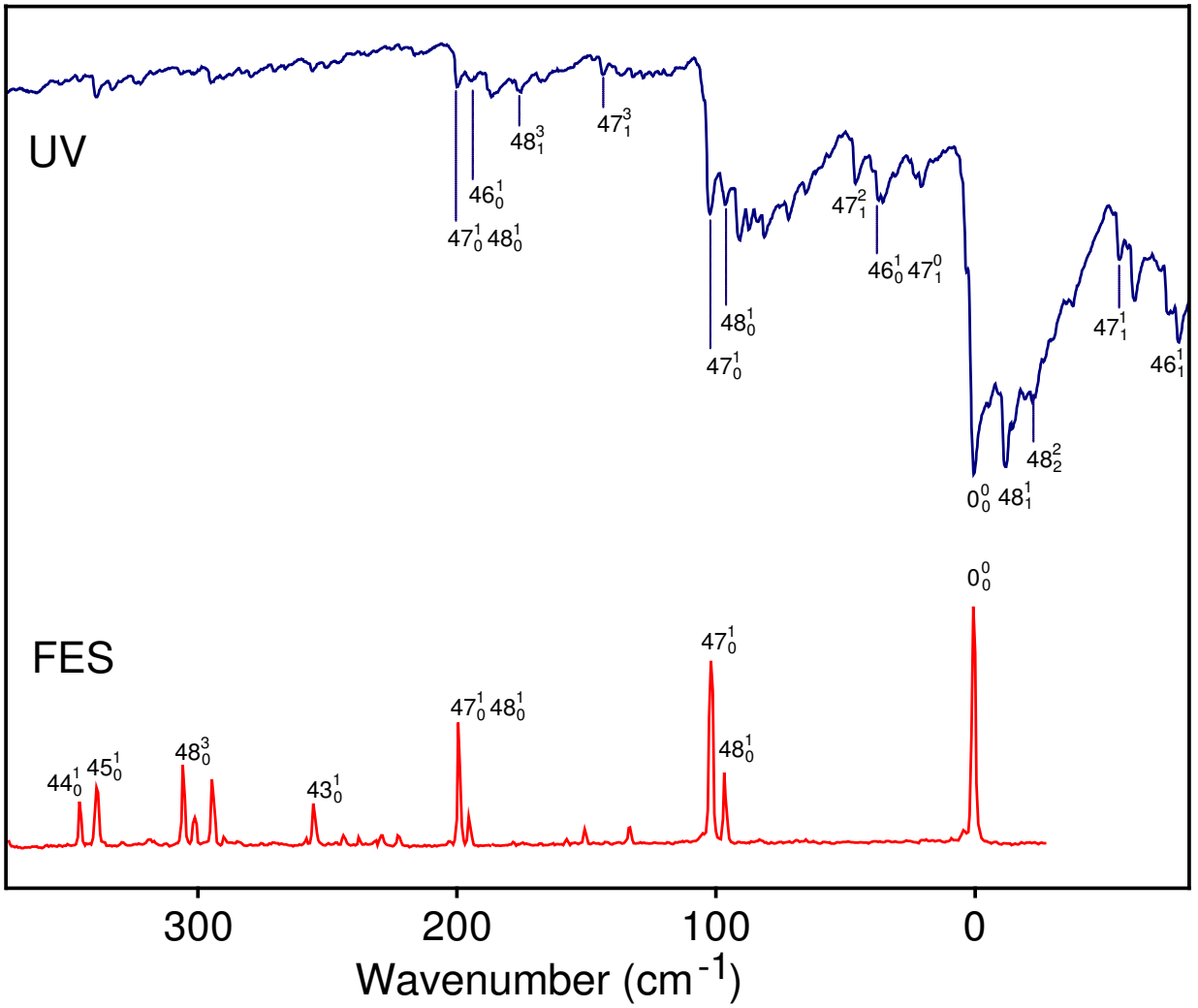

Figure 4. Ultraviolet absorption spectrum of 13BZN in a 15 cm cell at 25 °C compared to the FES and relative to the 0_0^0 band.

bands corresponding to the FES are also listed in Table 3. Additional hot band absorptions along with their assignments are shown in Table 4.

Figure 5 and Table 5 show and tabulate several of the single vibronic level fluorescence (SVLF) spectra of the molecule. The most intense bands are shown in bold type. Where appropriate the band positions are compared to the ultraviolet, infrared, and Raman spectral bands. The infrared and Raman spectra are available in Chapter IV. Figure 6 shows an energy diagram for the six lowest frequency vibrations of 13BZN. The bending (ν_{48}) and twisting (ν_{47}) vibrations of the five-membered ring are of greatest interest as the conformational dynamics of the molecule are primarily governed by their potential energy surface. The other four vibrations shown are a ring-flapping (ν_{46}), a benzene ring twisting (ν_{45}), an in-plane ring-bending (ν_{44}), and an out-of-plane ring bending (ν_{43}). Table 6 lists the observed and calculated vibrational wavenumbers for the low-frequency vibrations. As can be seen, the agreement between experimental and theoretical frequencies is very good, especially for the S_0 ground state. As shown in Figure 6, five excited states of ν_{48} can be seen in S_0 and four in S_1. Five excited states of ν_{47} in S_0 and four in S_1 can be seen. In addition, several combination levels between ν_{47} and ν_{48} can be observed. Other combinations are also evident in the figure and interactions between ν_{46} and ν_{48} are prominent.

The most significant changes in the quantum state energies between the S_0 and S_1 electronic states occur with the ν_{47} and ν_{46} twisting vibrations and the ν_{43} benzene ring bending vibration which drop significantly in energy in the $S_1(\pi,\pi^*)$ state as the $\pi \rightarrow \pi^*$

Table 4. Hot band combinations of 1,3-benzodioxan in the ultraviolet absorption spectra.

cm^{-1}	Assignment	Inferred[a]
-214.5 w	48_2^0	-216.8
-178.7 mw	$46_1^0 48_0^1$	-178.1
-127.6 mw	48_3^2	-127.1
-118.2 m	48_2^1	-118.2
-112.6 w	$47_0^1 48_2^0$	-112.3
-79.1 s	46_1^1	-79.6
-62.1 0s	$47_1^0 48_0^1$	-61.3
-56.2 s	47_1^1	-55.4
-22.4 w	48_2^2	-22.6
-12.2 vs	48_1^1	-11.6
	$47_0^2 48_2^0$	-11.7
-6.4 w	$47_0^1 48_1^0$	-5.7
20.3 mw	$47_1^0 48_1^3$	21.4
35.1 m	$47_1^0 48_0^2$	34.3
36.8 m	$46_0^1 47_1^0$	36.7
45.7 m	47_1^2	45.2
65.0 w	$45_0^1 46_1^0$	65.3
71.6 mw	48_2^3	72.4
80.9 mw	$47_0^1 48_2^2$	79.8
83.4 w	48_1^2	84.0
86.8 mw	$46_0^1 48_1^0$	86.4
90.4 s	$47_0^1 48_1^1$	90.6
131.4 vw	$47_1^0 48_0^3$	129.3
136.2 vw	$47_1^1 48_0^2$	136.5
143.1 w	47_1^3	144.0
175.1 w	48_1^3	179.0

s- strong; m-medium; w-weak; v-very

a) Inferred from other spectroscopic transitions (FES, SVLF, IR, Raman, UV)

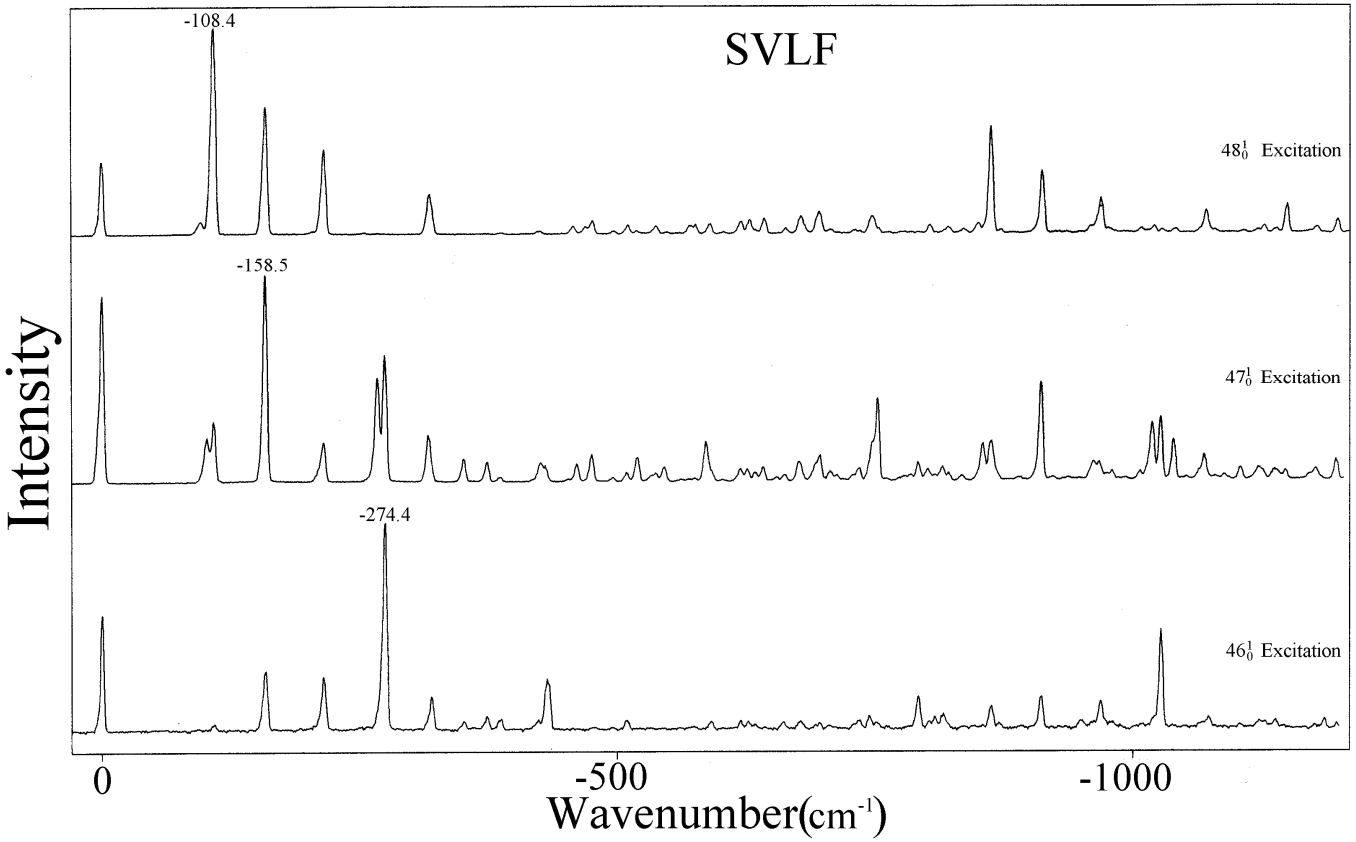

Figure 5. SVLF spectra of 13BZN from several excitation bands.

Table 5. Single vibronic level fluorescence (SVLF) frequencies[a] and assignments from various excitation bands of 1,3-benzodioxan.

FES[a]	0	96.3	101.7	199	525.2	627.2	676.6	722.1			
Assignment	0_0^0	48_0^1	47_0^1	46_0^1	39_0^1	$39_0^1 47_0^1$	47_0^2	35_0^1	Ave.	UV	IR/Raman[b]
48_1^0	**-108.4**	**-108.7**	**-107.4**	**-108.5**	-108.4	-108.9	-108.4	**-108.3**	-108.4	-107.9	
47_1^0	**-158.2**	**-158.5**	**-157.6**	-158.1	-158.2	-158.1	-158.3	**-158.2**	-158.2	~-157.6	178
48_2^0	-215.0	**-215.2**	**-213.8**	-214.4		-214.8	-214.8	-215.0	-214.7	-214.5	
$47_1^0 48_1^0$	-266.7		**-266.4**	-266.1	-266.9		-266.6	-266.8	-266.6		
46_1^0			**-272.0**	**-272.3**		-270.4	-273.2	-273.8	-272.3	-273.9	284
47_2^0	**-317.0**	**-317.0**	**-316.1**	**-316.8**		-316.8	-317.2	-318.4	-317.0	-315.9	
45_1^0	**-350.9**		-350.1	-351.2		-351.6	-351.2	-351.2	-351.0	-350.6	356
44_1^0	-360.0			-360.5			-361.1	-360.8	-360.6	-358.8	369
$47_1^0 48_2^0$			-372.3	**-373.2**	-373.6	-373.2	-373.9	-373.6	-373.3		
$46_1^0 48_1^0$	-385.9		-385.4	**-386.3**				-386.6	-386.1		
$47_2^0 48_1^0$		-423.0	-426.3	-422.7	-422.4				-423.6		
43_1^0	**-429.6**		-426.3		-431.4	**-430.3**	-436.4	-430.3	-430.7	-429.7	435 IR
$45_1^0 48_1^0$		-456.6		-456.1			-457.4		-456.7		
42_1^0	**-461.1**		-459.7		-460.5	-460.4		-462.0	-460.7	-460.4	464 IR
$44_1^0 48_1^0$	-468.9	-468.0					-468.3	-468.1	-468.3		
47_3^0		-473.8	-473.9	**-475.3**		-475.7	-478.3		-475.4		
$46_1^0 48_3^0$	-495.3	-494.9	-494.2	-495.5	-496.0		-496.5	-496.0	-495.5		
$45_1^0 47_1^0$		-509.4	-507.8			-509.6	-509.0		-509.0		
41_1^0	**-518.3**	-519.1	-517.9	-522.0	**-519.2**	-519.9	-524.1	**-519.2**	-520.0	-518.0	520 IR

Table 5. Continued.

FES[a]	0	96.3	101.7	199	525.2	627.2	676.6	722.1			
Assignment	0_0^0	48_0^1	47_0^1	46_0^1	39_0^1	$39_0^1 47_0^1$	47_0^2	35_0^1	Ave.	UV	IR/Raman[b]
40_1^0	**-535.1**	-536.0	-534.3	-535.2	-535.9	-534.9	-537.1	-536.1	-535.6	-533.7	536 IR
46_2^0	-547.4		-543.8		-547.9	-548.2	-548.2	-547.3	-547.1	-547.0	
$45_1^0 48_2^0$				-560.7	-560.3		-562.8	-559.7	-560.9		
$42_1^0 48_1^0$	572.0		-571.6	-569.7	-571.4			-574.1	-571.8		
39_1^0	**-587.3**		**-585.4**	-586.9	**-586.9**	**-587.6**	-587.0	**-587.8**	-587.0	-588.6	588 IR
$46_1^0 48_4^0$					-602.5	-601.9			-602.2		
$45_1^0 47_1^0 48_1^0$			-622.5	-619.1	**-615.0**	-620.3		-616.0	-618.6		
$45_1^0 46_1^0$	-624.2		-622.5	-619.1		-620.3	-624.6	-622.4	-622.2		
$44_1^0 47_1^0 48_1^0$	-624.2		-622.5		-628.3				-625.0		
47_4^0				-632.0		-632.7			-632.4	-633.8	
$40_1^0 48_1^0$	-641.2		-639.4		-638.6	-642.5		-641.2	-640.6	-646.7	
$46_2^0 48_1^0$					-654.0	-657.3	-659.7		-657.0		
	-662.5		-660.2		-663.4		-659.7		-661.5	-662.8	
$45_1^0 47_2^0$				-667.9				-665.8	-666.9		
$41_1^0 47_1^0$	-676.5		-675.1		-678.4	**-678.9**	-678.6	-677.8	-677.6		
38_1^0	-696.2		-693.7	-694.4	-695.9	**-695.8**		**-697.9**	-695.7		698 IR
45_2^0							**-701.1**		-701.1		
$46_2^0 47_1^0$			-705.3		-704.6				-705.0		
37_1^0	-710.0				**-712.9**	**-713.8**	**-712.9**	-713.5	-712.6		712 IR
$45_1^0 46_1^0 48_1^0$			-731.7	-736.2	-733.6	**-732.7**	-731.5	-732.6	-733.1		

Table 5. Continued.

FES[a]	0	96.3	101.7	199	525.2	627.2	676.6	722.1			
Assignment	0_0^0	48_0^1	47_0^1	46_0^1	39_0^1	$39_0^1 47_0^1$	47_0^2	35_0^1	Ave.	UV	IR/Raman[b]
36_1^0			**-749.4**	-748.8		-745.5			-747.9		752 IR
35_1^0	**-752.4**			-748.8	**-752.7**			**-754.1**	-752.0	-752.5	756 IR
							-762.8		-762.8	-764.8	
$45_1^0 47_2^0 48_1^0$			-777.1	-775.9		-775.7			-776.2		
$45_1^0 46_1^0 47_1^0$			-777.1		-781.4			-779.0	-779.2		
47_5^0			-790.1	-791.2	-781.4	-792.3	-793.9	-791.3	-790.0		
$38_1^0 48_1^0$			-800.1	-802.3	-802.3	-802.8		-803.4	-802.2		
							-809.8		-809.8		
			-814.5	-819.7	-821.6	-823.1	-821.2	-822.1	-820.4		
$41_1^0 47_2^0$			-832.9	-835.1	-836.8	-836.6	-837.2	-838.0	-836.1		
34_1^0				-848.1	**-850.8**		-851.6		-850.2		853
33_1^0	**-860.1**		**-860.2**			**-858.5**			-859.6		
43_2^0	**-863.1**			**-861.0**	**-861.2**	**-862.9**	-863.3	-863.3	-858.0		
$42_1^0 46_1^0 47_1^0$			-888.2	-885.7				**-880.8**	-884.9		
$36_1^0 47_1^0$				-904.8		-904.8			-904.8		
$35_1^0 47_1^0$	-911.0		**-909.1**		-907.5	**-912.8**			-911.4		
				-920.7					-920.7		
32_1^0	-936.5			-935.4	-936.9	-938.5			-936.8		[934]
31_1^0	-947.2					-949.7		-952.3	-949.7		949
30_1^0	-964.1		-962.8	-961.8	-959.4	**-966.4**			-962.9		[965]

Table 5. Continued.

FES[a]	0	96.3	101.7	199	525.2	627.2	676.6	722.1			
Assignment	0_0^0	48_0^1	47_0^1	46_0^1	39_0^1	$39_0^1 47_0^1$	47_0^2	35_0^1	Ave.	UV	IR/Raman[b]
	-977.7			-973.3	-969.5	**-982.8**			-975.8		
29_1^0				-992.1					-992.1		994 IR
28_1^0			-1004.4	-1007.9	-1009.4	**-1009.5**			-1007.8		1011 IR
	-1017.9		**-1016.9**		-1019.4				-1018.1		
			-1025.6	-1025.2		**-1022.7**			-1024.5		
27_1^0	**-1040.0**		**-1037.8**	-1039.2	-1046.0				-1040.8		1035
					-1046.0	-1049.3			-1047.7		
40_2^0	**-1068.6**		-1066.8	**-1068.2**	-1066.8	-1066.7		-1057.9	-1065.8		
26_1^0	**-1088.6**		-1086.6					-1086.9	-1087.4		1079 IR
25_1^0	-1104.8		-1102.3		-1104.2				-1103.8		1100 R
	-1122.6		-1121.4	-1124.9	-1121.6	**-1126.4**			-1123.4		
$37_1^0 46_1^0 47_1^0$			-1135.5	**-1138.5**	-1141.3	-1138.7			-1138.5		
24_1^0	-1148.1		-1145.8	-1146.8	-1141.3				-1145.5		1150 IR
23_1^0				-1163.0					-1163.0		1157
	-1179.5		-1175.5	-1175.7	**-1174.5**	**-1176.2**			-1176.3		
$27_1^0 47_1^0$	-1197.4		**-1196.0**		-1201.1	**-1176.2**			-1198.2		
22_1^0	**-1215.3**		-1212.8	-1208.7	-1209.8	-1211.3			-1211.6		1210 IR
21_1^0	**-1235.9**		**-1231.6**	-1227.2	-1233.8	-1231.6		-1229.6	-1231.6		1232 IR
20_1^0	**-1247.4**		-1246.4	-1247.4	-1250.1	-1253.2		-1255.2	-1250.0		1238 IR
$36_1^0 41_1^0$	-1269.9			-1262.0	-1271.9	-1263.7		-1268.9	-1267.3		

Table 5. Continued.

FES[a]	0	96.3	101.7	199	525.2	627.2	676.6	722.1			
Assignment	0_0^0	48_0^1	47_0^1	46_0^1	39_0^1	$39_0^1 47_0^1$	47_0^2	35_0^1	Ave.	UV	IR/Raman[b]
19_1^0	-1288.1		-1284.4	-1284.7		-1283.0			-1285.1		1275 IR
18_1^0					-1298.2	-1299.2			-1298.7		1291 IR
17_1^0	-1308.6		-1305.1						-1306.9		1309
16_1^0	-1356.1		-1353.8	**-1355.0**	-1356.1				-1355.3		1359 IR
15_1^0				-1410.9		-1409.1			-1410.0		1409 IR
14_1^0	-1463.1			-1459.2					-1461.1		1460 IR
12_1^0	-1495.1								-1495.1		1492 IR
11_1^0	**-1503.4**								-1503.4		[1501]
10_1^0	-1587.7								-1587.7		1587 IR

[a] All frequencies are in units of relative wavenumbers (cm^{-1})

[b] Values taken from Table II. Values are assumed to be Raman unless denoted by an IR when values are from the IR or by a [ ] when values are from calculations.

[c] Assigned twice.

Bolded values represent the more intense bands.

The 48_0^1 spectrum was not extended beyond -540 cm^{-1}.

Above 1300 cm^{-1} only SVLF bands corresponding to fundamentals are listed.

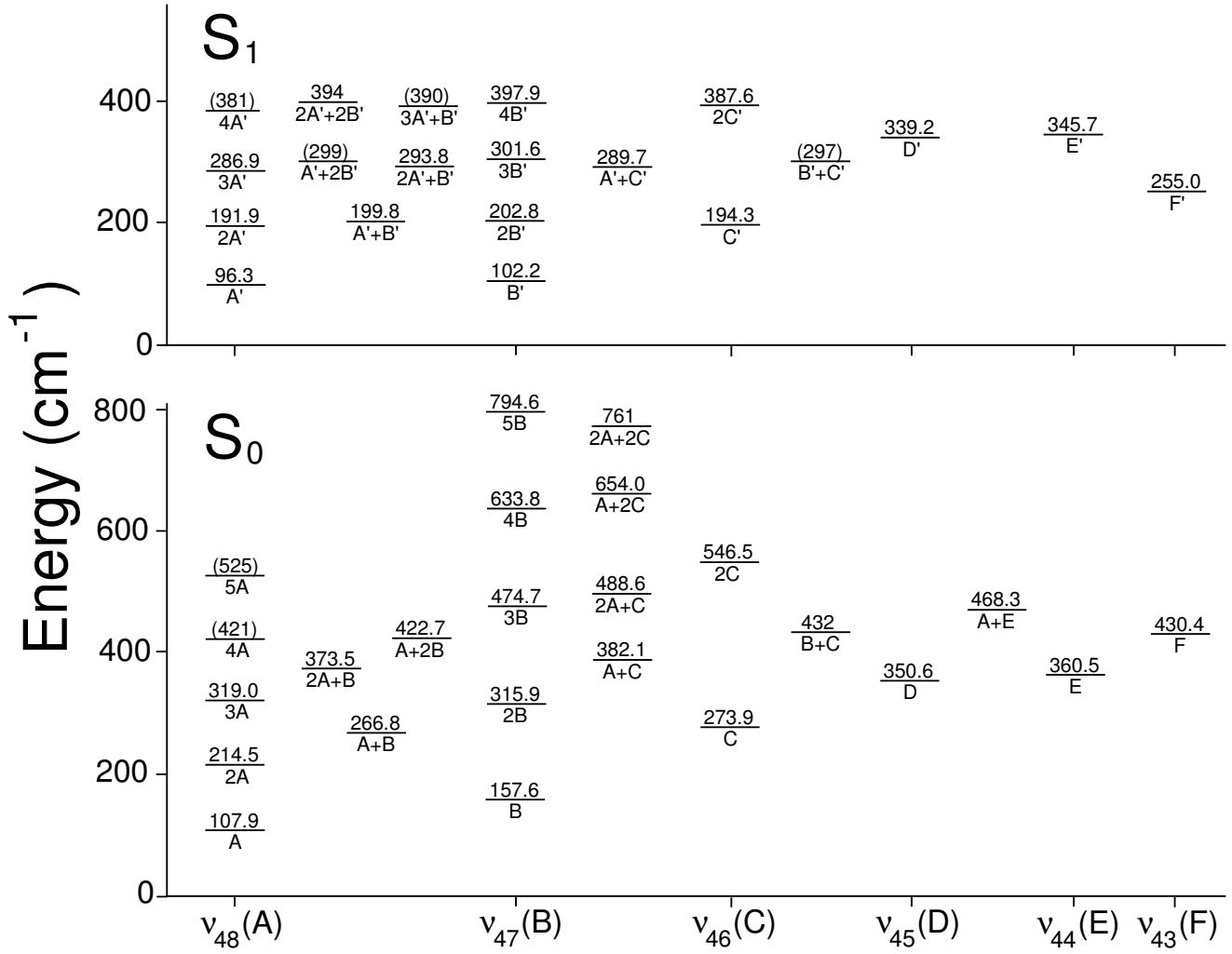

Figure 6. Energy levels for the low-frequency vibrations of 13BZN in its ground and $S_1(\pi,\pi^*)$ excited states.

Table 6. Low-frequency vibrations (cm^{-1}) of 1,3-benzodioxan.

		S_0		S_1	
Vibration	Approx. Description	Observed	Calculated[a]	Observed	Calculated[b]
43 (F)	Bz ring-bending (o.p.)	430.4	436	255.0	241
44 (E)	Ring-bending (i.p.)	360.5	360	345.7	367
45(D)	Bz ring-twisting	350.6	347	339.2	353
46 (C)	Ring-flapping	273.9	275	194.3	200
47 (B)	Ring-twisting	157.6	158	102.2	116
48 (A)	Ring-bending (o.p.)	107.9	106	96.3	102

i.p. = in-plane; o.p. = out-of-plane
[a]B3LYP/6-311++G(d,p); scaling factor = 0.985
[b]CIS/6-311+G**; scaling factor = 0.980

transition results in reduced π bonding in the excited state. Vibration ν_{47} drops from 157.6 to 102.2 cm^{-1} and ν_{46} drops from 273.9 to 194.3 cm^{-1}. The ν_{43} out-of-plane benzene bending vibration also has a large decrease in frequency, from 430.4 to 255.0 cm^{-1}.

VIBRATIONAL POTENTIAL ENERGY SURFACE

Ideally, it would be desirable to use the experimental data for ν_{47} and ν_{48} to calculate two-dimensional potential energy surfaces (PESs) in terms of these two vibrations. We have been able to do this in the past for a number of bicyclic molecules for both ground and excited states.[2-6] However, for tetralin[7] and 1,4-benzodioxan[8] the barriers to planarity were so high that only one-dimensional potential functions for the twisting motion could be calculated, and these had significant uncertainties for the calculated barriers (± 2000 cm^{-1}). The situation for 13BZN is similar so only a one-dimensional calculation was carried out.

The vibrational Hamiltonian for the one-dimensional potential energy calculation is

$$\mathcal{H} = -\frac{\hbar^2}{2}\frac{\partial}{\partial\tau}g_{44}(\tau)\frac{\partial}{\partial\tau} + V(\tau) \qquad (1)$$

where τ is the twisting coordinate and $g_{44}(\tau)$ is the reciprocal reduced mass expression as a function of coordinate. These have previously been defined along with the methodology for their calculation.[15] The potential energy function for this type of double-minimum problem that has worked well in the past is of the form

$$V(\tau) = a\tau^4 + b\tau^2 \tag{2}$$

where a and b are potential energy parameters. As discussed in the previous study of 14BZD, the calculation of g_{44} by previous methods was not very successful since the one-dimensional model neglects the significant interaction between ν_{48} and ν_{47}. For 13BZN the reduced symmetry almost certainly increases this interaction. Hence, it was practical to calculate the potential energy function in reduced coordinates[15] defining the dimensionless coordinate z by

$$z = \left(\frac{2A}{g_{44}}\right)^{\frac{1}{2}} \tau / \hbar . \tag{3}$$

This transforms Eq. (2) into

$$V = A(z^4 + Bz^2) \tag{4}$$

where

$$A = (\hbar^2 g_{44} / 2)^{2/3} a^{1/3} \tag{5}$$

and

$$B = (\hbar^2 g_{44} / 2)^{-1/3} a^{-2/3} b . \tag{6}$$

Utilizing previously described[2-6] computer programs, the A and B potential energy parameters can then be adjusted to fit the experimental data for the ring-twisting (ν_{47}). For the S_0 ground state, the barrier to planarity is so high that the separations between the degenerate pairs of quantum states are expected to be nearly the same and appear to be nearly harmonic. In fact, as is evident in Figure 6 for the ν_{47} in the S_0 state, the twisting level separations slightly increase with quantum number. This is sometimes the

case for very high barriers depending on the shape of the potential energy curve near the bottom of the double minimum wells. When the levels get closer to the top of a barrier, the separations begin to decrease at an increasingly rapid pace. What this means is that the experimental data here is insufficient for calculating the barrier height. However, previous experience[2-6] has shown that *ab initio* calculations at a high level of theory do an excellent job of predicting barriers for electronic ground states. Typically the calculated barriers are slightly on the high side. For 13BZN we assume the barrier to be 4300 cm^{-1} (12.3 kcal/mole) based on the calculated values in Table 1. Using this value and the observed $0 \rightarrow 2$ frequency (coincident with $1 \rightarrow 3$) at 157.6 cm^{-1}, the reduced potential energy function is calculated to be

$$V(cm^{-1}) = 8.34(z^4 - 45.3z^2). \quad (7)$$

The calculated wavenumbers for the ring-twisting quantum states from this function are compared to the observed values in Table 7. As is evident, the observed values show a spread in the separations as described above. For the S_1 excited state the calculated potential energy function can be determined nicely from the four observed energy states since the barrier is much lower. This function is

$$V(cm^{-1}) = 6.66(z^4 - 30.1z^2), \quad (8)$$

and the barrier is calculated to be 1509 cm^{-1}. The calculated energies for the twisting states in S_1 are also shown in Table 7 and compared to the observed values. Figure 7 shows the calculated potential energy functions for the two electronic states. As is evident, the experimental data are only available for quantum states below 1000 cm^{-1}.

Table 7. Observed and calculated ring-twisting energy levels (cm^{-1}) for 13BZN in its ground and $S_1(\pi,\pi^*)$ excited states.

	S_0		S_1	
ν	Observed	Calculated[a]	Observed	Calculated[b]
1	158.4	158.4	102.2	102.0
2	315.9	314.1	202.8	202.6
3	474.7	469.4	301.6	301.7
4	633.8	623.6	397.9	399.2
5	794.6	776.5	------	495.0

[a] $V(cm^{-1}) = 8.34\ (z^4 - 45.3z^2)$; barrier = 4300 cm^{-1}

[b] $V(cm^{-1}) = 6.66\ (z^4 - 30.1z^2)$; barrier = 1509 cm^{-1}

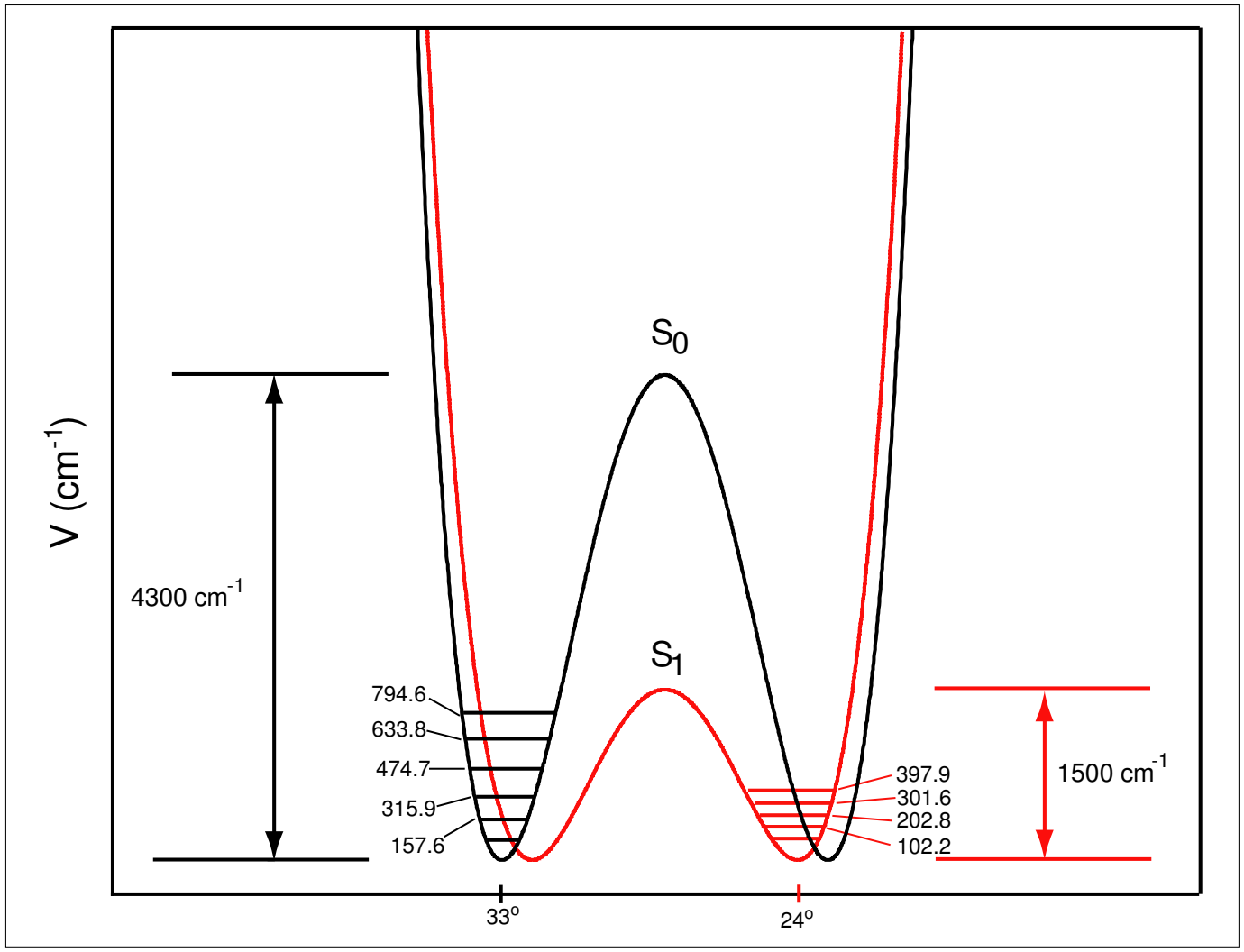

Figure 7. Potential energy functions for the ring-twisting of 13BZN in its S_0 and $S_1(\pi,\pi^*)$ states.

Nonetheless, it is clear that in the $S_1(\pi,\pi^*)$ state the barrier to planarity along the twisting coordinate is much lower than in the S_0 ground state. The energy minima for the S_0 state are labeled to be at ± 33° which is the value calculated from the *ab initio* computation. For the $S_1(\pi,\pi^*)$ twisting vibration, the twisting minima are calculated to be at ± 24° in the excited state.

DISCUSSION

The experimental results show 13BZN to have a twisted six-membered ring for both its S_0 and $S_1(\pi,\pi^*)$ states. The *ab initio* calculation predicts the barrier to planarity for the ground state to be 4300 cm^{-1}, and we consider this value to be quite reliable (± 500 cm^{-1}). Analysis of the experimental ring-twisting quantum states for $S_1(\pi,\pi^*)$ allows a one-dimensional potential function with a barrier of 1509 cm^{-1} to be calculated. The uncertainty, based on the approximations intrinsic to a one-dimensional calculation, is estimated to be ± 200 cm^{-1}.

Table 8 compares the barriers to planarity of 13BZN to those of 14BZD and TET. There are rather larger uncertainties in these numbers but the trends from S_0 to S_1 and between the three molecules should be reliable. The table also compares the vibrational frequencies for the six-membered ring bending and twisting. The barriers to planarity are determined by three factors: angle strain, $-CH_2-CH_2-$ torsional interactions, and the anomeric effect, if present. For all three molecules the angle strain will tend to twist or bend the molecules as the interior ring angles strive to become less than 120°. The torsional interactions will also tend to twist the six-membered ring attached to t

Table 8. Barriers to planarity (kcal/mole) and bending and twisting frequencies (cm^{-1}) of tetralin and its oxygen analogs.

	S_0			S_1		
Molecule	Barrier	ν_{BEND}	ν_{TWIST}	Barrier	ν_{BEND}	ν_{TWIST}
TET	17.1	94.3	141.7	11.4	85.1	94.5
14BZD	14.3	104.3	165.6	10.3	79.8	139.6
13BZN	12.3	107.9	157.6	4.3	96.3	102.2

benzene ring so as to move away from eclipsing CH_2 groups. These two factors readily explain the S_0 structures and high barriers for TET and 14BZD. TET has three -CH_2-CH_2- torsional interactions while 14BZD has one, so the latter molecule has a smaller barrier to planarity. The 13BZN molecule studied in the present work has a somewhat lower barrier to planarity, but given that it has no -CH_2-CH_2- torsional interactions, it still is quite large. This can be explained by the anomeric effect due to the presence of the -O-CH_2-O- linkage in the molecule which has been shown[9-11] to result in bending of the molecular structure. For the $S_1(\pi,\pi^*)$ excited state all three of the molecules have lower barriers to planarity which are most likely due to the angle strain effects as the $\pi \rightarrow \pi^*$ transition of the benzene ring results in a less rigid conformation. This is reflected also by the large decrease of the ring-twisting frequency for all of these molecules. The large drop in the barrier for 13BZN to about 1500 cm^{-1}, however, is surprising. For 1,3-benzodioxole,[9] which shows a strong anomeric effect in its five-membered ring, the barrier to planarity increased in its $S_1(\pi,\pi^*)$ state as the suppression of the anomeric effect was decreased. As is evident, this is not the case for 13BZN. It may be that the $S_1(\pi,\pi^*)$ state has reduced interaction between the benzene ring and the adjacent oxygen atom, thereby affecting the conformational dynamics of the attached ring.

CHAPTER IV

VIBRATIONAL SPECTRA AND THEORETICAL CALCULATIONS OF 1,3-BENZODIOXAN IN ITS GROUND AND EXCITED ELECTRONIC STATES

INTRODUCTION

The laser-induced fluorescence (LIF) spectra and theoretical calculations of 1,3-benzodioxan (13BZN) focusing on its low-frequency vibrations and conformational energetics have been described in Chapter III of this work. In this chapter a comprehensive study of all the vibrations of 13BZN in both its S_0 ground and $S_1(\pi,\pi^*)$ excited states is presented. Data from infrared and Raman spectra, fluorescence excitation spectra (FES), and single vibronic level fluorescence (SVLF) or dispersed spectra will be utilized along with *ab initio* and DFT calculations to assign the vibrations. Of particular interest will be the differences in the vibrational frequencies between the S_0 and $S_1(\pi,\pi^*)$ states resulting from the $\pi \rightarrow \pi^*$ transition.

EXPERIMENTAL

Raman spectra of the liquid sample were recorded using a Jobin-Yvon U-1000 spectrometer equipped with a CCD. A Coherent Verdi V-10 Nd:YAG system (532 nm, 0.5w) was used for excitation. Infrared spectra of the the liquid sample between KBr discs were recorded with a Bruker Vertex 70. The single vibronic level fluorescence (SVLF) spectra were recorded using a Continuum Powerlite 9020 Nd:YAG laser which pumped a Continuum Sunlite OPO and FX-1 ultraviolet extension unit. SVLF spectra

were taken with a spectral resolution of 1 cm^{-1} and were recorded under jet-cooled conditions. Dr. Martin Wagner assisted with the recording of the fluorescence spectra.

CALCULATIONS

Theoretical calculations for the ground state were carried out using the GAUSSIAN 03 package.[13] For the excited state, TURBOMOLE calculations were carried out by Dr. Jaebum Choo of Hanyang University. The ground state S_0 structure using the B3LYP/6-311+G(d,p) basis set and for the $S_1(\pi,\pi^*)$ excited state using the CIS/6-311+G(d,p) basis set were determined. The vibrational frequencies for the S_0 ground state were calculated by DFT methods using the B3LYP/6-311++G(d,p) basis set. For the $S_1(\pi,\pi^*)$ excited state the CIS/6-311+G** basis set was utilized.

MOLECULAR STRUCTURE

The complete calculated molecular structures for the S_0 and $S_1(\pi,\pi^*)$ states were presented in Chapter III of this work. The bond distances for the skeletal structures for the two electronic states are shown in Figure 8. Reference to this figure will help to understand some of the differences in the vibrational energy levels in the two electronic states. As can be seen the benzene bond distances increase from an average of 1.393 Å to 1.411 Å as expected from the $\pi \rightarrow \pi^*$ transition. In the saturated ring a C-O bond distance is significantly reduced from 1.402 to 1.376 Å while the oxygen atom to benzene ring C-O bond decreases from 1.359 to 1.312 Å. The other three bonds change

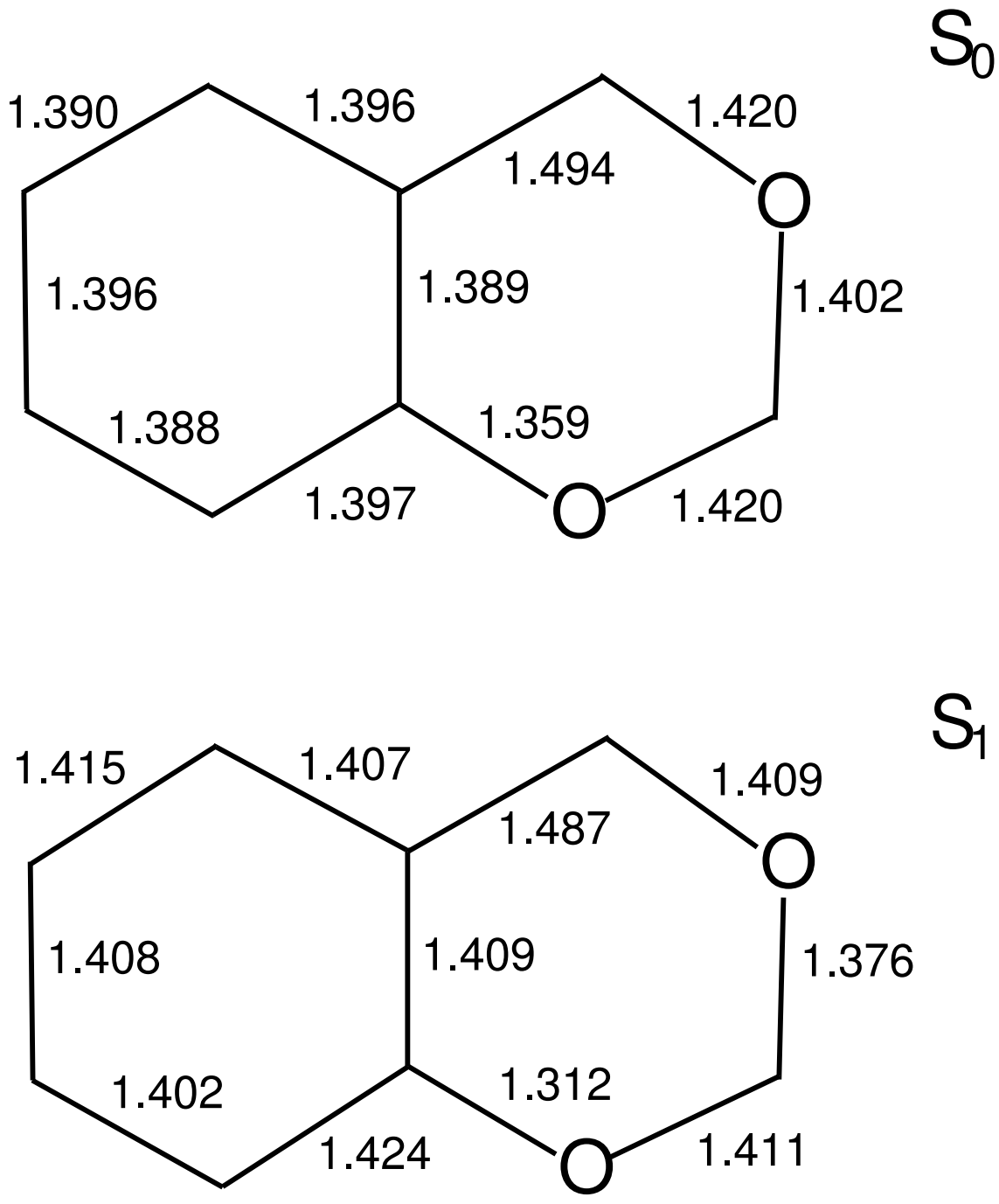

Figure 8. Skeletal structures of 13BZN in its S_0 and $S_1(\pi,\pi^*)$ electronic states.

by no more than 0.011 Å. As noted in Chapter III the twisting angle of the five-membered ring is reduced from 33° in the ground state structure to 24° in $S_1(\pi,\pi^*)$.

RESULTS AND DISCUSSION

Figure 9 compares the experimental infrared spectrum of 13BZN liquid to the calculated one and Figure 10 compares the experimental and calculated Raman spectra. The frequency agreement can be seen to be excellent. The calculated intensities are fairly good, but as is usually the case, the agreement is somewhat poorer. Table 9 summarizes all of the essential data including the experimental and calculated infrared and Raman spectra. The SVLF spectra, which also provide data for the S_0 ground state, are also tabulated. The vibrations of 13BZN are very similar to those of 1,4-benzodioxan (14BZD)[16] so these frequencies are also listed for comparison. The table also lists the calculated vibrational frequencies for the $S_1(\pi,\pi^*)$ state and compares these to those determined from the FES spectra.[16]

Not surprisingly, the 13BZN and 14BZD frequencies are very similar for the electronic ground state. Even the lowest five frequencies which are very sensitive to even small differences in binding interactions are very similar for the two molecules. For 13BZN these are 360, 351, 274, 158, and 108 cm^{-1} while for 14BZD they are 377, 317, 297, 166, and 104 cm^{-1}, respectively.

Table 9 also lists the calculated frequencies for the $S_1(\pi,\pi^*)$ state of 13BZN. From the FES spectra presented in Chapter III twelve frequencies were determined and these were used to calculate a scaling factor of 0.940 which provides reasonably good

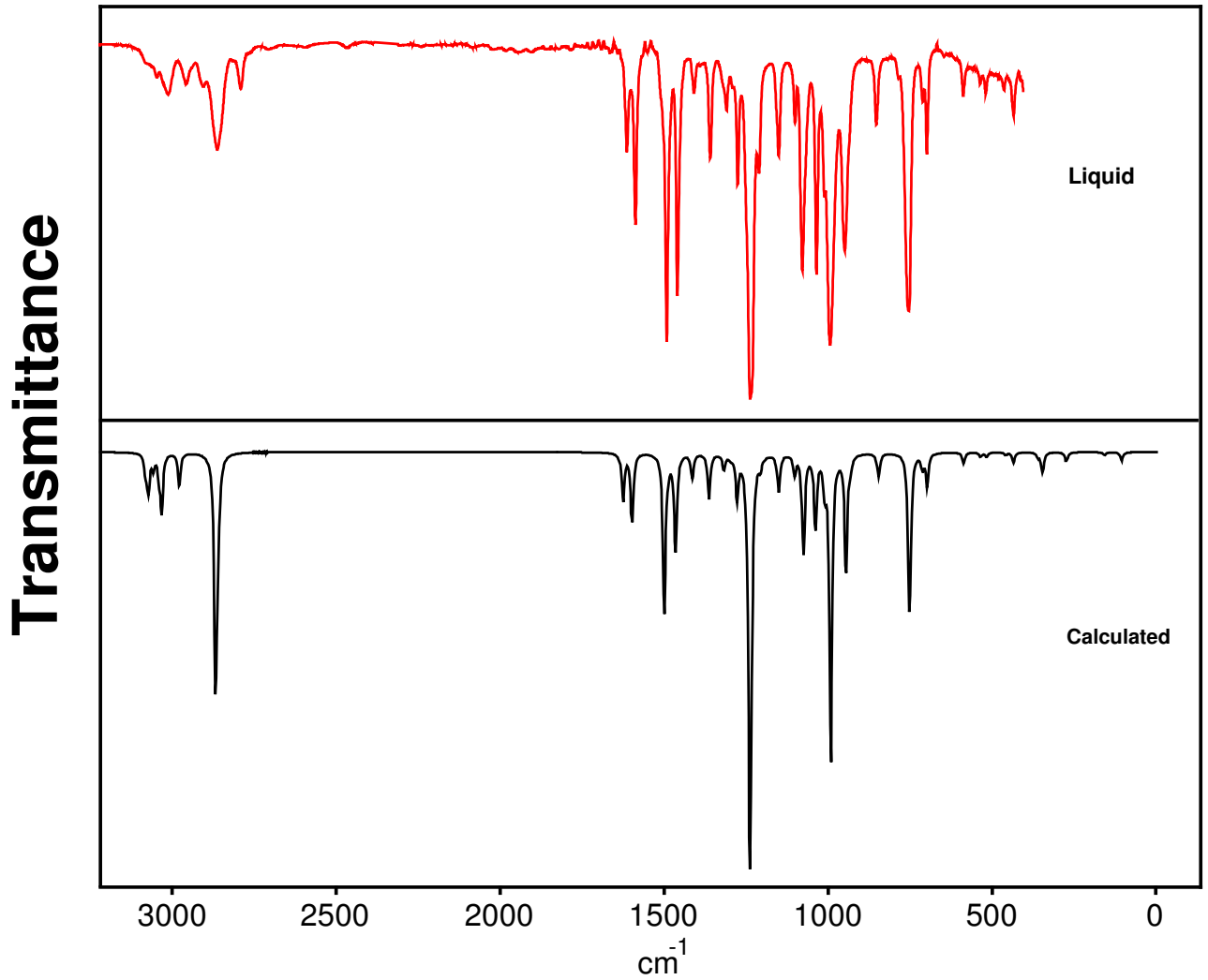

Figure 9. Experimental and calculated infrared spectra of 13BZN.

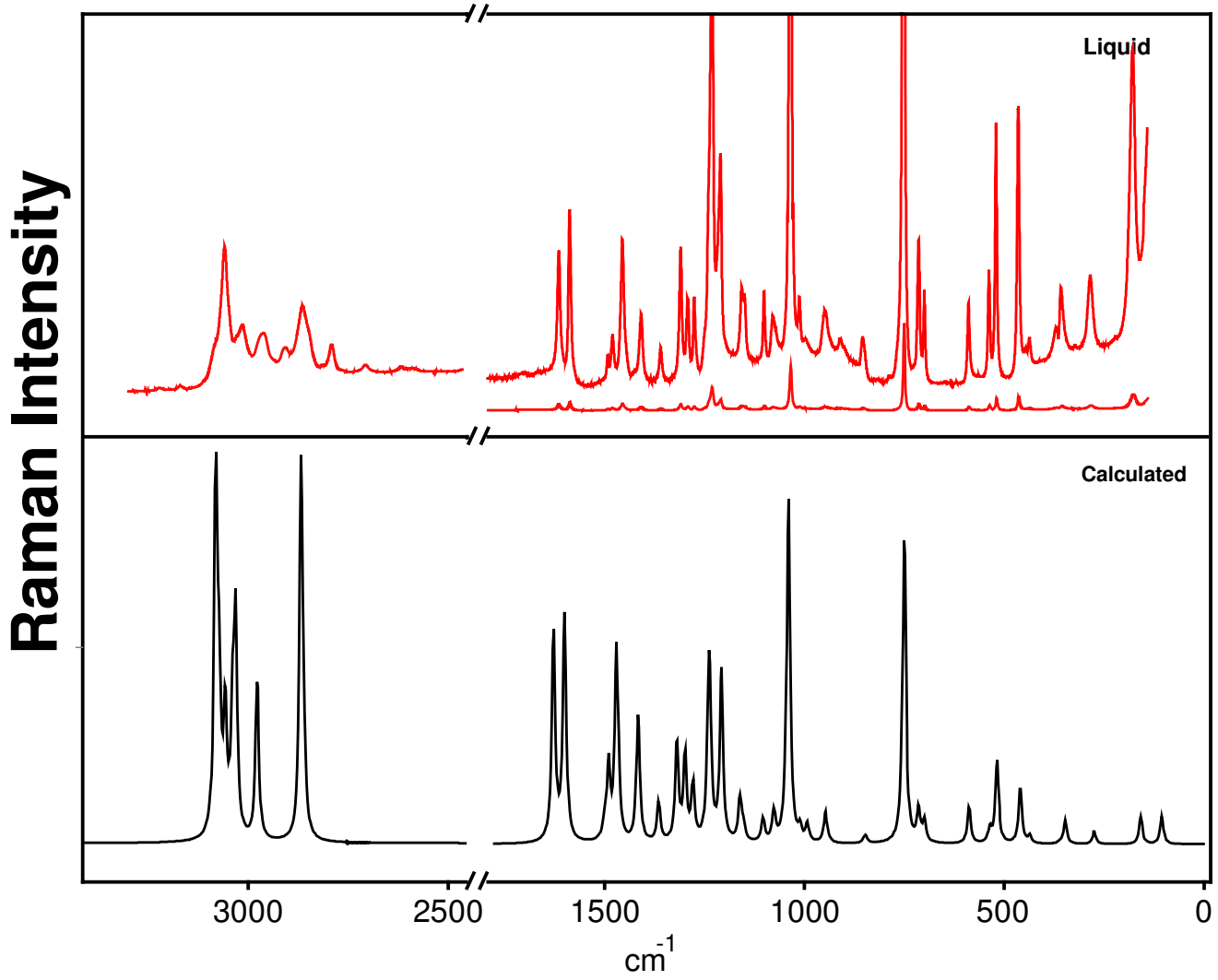

Figure 10. Experimental and calculated Raman spectra of 13BZN.

Table 9. Experimental and calculated vibrational frequencies(cm^{-1}) and assignments for 1,3-benzodioxan in its S_0 ground and S_1 excited states.

				Ground State (S_0)						Excited State (S_1)		
			Description	IR	Raman	SVLF	Calculated[a]		14BZD[b]	Obs	Calc[c]	14BZD[b]
	C_s	C_1					C_1	C_s				
A’	1	1	C-H sym. stretch	3081 w			3081 (6,903)	3081	3082 (A_1)		3047	
	2	2	C-H stretch				3072 (12,337)	3073	3082 (B_2)		3028	
	3	3	C-H stretch		3060 (38)		3057 (5,307)	3057	3070 (A_1)		3020	
	4	4	C-H stretch	3030 sh	3031 (11)		3039 (6,285)	3039	3058 (B_1)		3005	
	5	7	CH_2 sym. stretch (ip)				2868 (70,939)	2907	2886 (B_1)		2855	
	6	8	CH_2 sym. stretch (op)	2862 mw	2864 (18)		2861 (29,168)	2898	2885 (A_1)		2765	
	7	9	Benzene stretch	1614 m	1614 (7)		1627 (16,61)	1626	1602 (A_1)		1665	
	8	10	Benzene stretch	1587 ms	1587 (9)		1599 (22,65)	1611	1599 (B_1)		1608	
	9	11	Benzene stretch				1501 (52,4)	1517	1500 (A_1)		1559	
	10	12	CH_2 deformation (ip)	1492 s	1492 (2)		1490 (2,22)	1506	1469 (A_1)		1528	
	11	13	CH_2 deformation (op)		1479 (2)		1471 (3,53)	1488	(1469) (B_1)		1507	
	12	14	Benzene stretch	1460 s	1455 (8)		1466 (30,7)	1468	1462 (B_1)		1481	
	13	15	CH_2 wag	1409 w	1410 (4)		1415 (8,37)	1445	1381 (A_1)		1460	
	14	16	CH_2 wag	1359 m	1359 (2)		1364 (15,11)	1381	1362 (B_1)		1405	
	15	17	CH_2 twist	1309 mw	1309 (7)		1319 (5,29)	1326	1307 (A_1)		1381	
	16	18	CH_2 twist	1291 w	1292 (4)		1299 (1,25)	1289	1289 (B_1)		1341	
	17	20	Sat. ring stretch	1238 s	1240 sh		1240 (99,25)	1259	1250 (A_1)		1277	
	18	22	C-H wag *	1210 m	1210 (11)		1208 (3,50)	1219	1195 (B_1)		1234	
	19	23	C-H wag		1157 (4)		1161 (0.2,12)	1159	1150 (A_1)		1186	1253
	20	24	C-H wag	1150 m	1150 (4)		1152 (13,4)	1130	1114 (B_1)		1160	
	21	26	Sat. ring stretch	1079 ms	1078 (2)	-1070	1077 (32,8)	1100	1074 (A_1)		1071	
	22	27	Sat. ring stretch	1035 ms	1035 (50)	-1041	1040 (24,100)	1046	1061 (B_1)		1051	
	23	28	Ring stretch *	1011 m	1012 (2)		1011 (9,4)	1023	1028 (A_1)		1023	
	24	32	Sat. ring stretch			-939	934 (3,0.2)	906	893 (A_1)		865	951
	25	33	Benzene ring bend	853[d] m	853[d] (2)	-849[d]	852 (1,1)	848	834 (B_1)		750	702
	26	35	Benzene stretch	756 s	751[d] (100)	-753[d]	753 (48,2)	759	735 (A_1)	722	697	
	27	37	Benzene ring bend	712 mw	713 (7)	-712	714 (5,9)	710	643 (B_1)	682	672	
	28	39	Benzene ring bend	588 mw	588 (4)	-588	588 (4,11)	581	566 (A_1)	525	521	531
	29	41	Sat. ring bend	520 w	519 (14)	-519	518 (1,24)	504	494 (B_1)	482	502	483
	30	42	Sat. ring bend	464 w	463 (14)	-461	459 (1,17)	453	463 (A_1)	442	451	493
	31	44	Sat. ring bend		369 (2)	-361	360 (2,1)	350	377 (B_1)	345	353	

Table 9. Continued.

				Ground State (S_0)						Excited State (S_1)		
	C_s	C_1	Description	IR	Raman	SVLF	Calculated[a] C_1	C_s	14BZD[b]	Obs	Calc[c]	14BZD[b]
A',	32	5	CH_2 antisym. stretch	3012 w	3015 (16)		3032 (18,537)	2941	2991 (A_2)		2994	
	33	6	CH_2 antisym. stretch	2957 w	2963 (14)		2978 (11,416)	2921	2893 (B_2)		2892	
	34	19	CH_2 twist	1275 m	1275 (4)		1279 (14,16)	1263	1282 (A_2)		1329	1413
	35	21	CH_2 twist	1232 s	1231 (26)		1237 (52,36)	1232	1243 (B_2)		1265	
	36	25	CH_2 rock	1100 mw	1100 (4)		1103 (6,7)	1101	1105 (A_2)		1111	
	37	29	CH_2 rock	994 s			993 (100,5)	1008	936 (B_2)		1008	948
	38	30	C-H wag			-966	965 (0.1,0.1)	964	953 (A_2)		987	
	39	31	C-H wag	979 ms	949 (2)	-949	947 (39,9)	931	924 (B_2)		890	
	40	34	C-H wag	853[d] m	853[d] (2)	-849[d]	847 (7,2)	846	843 (A_2)		744	888
	41	36	C-H wag	752 s	751[d] (100)	-753[d]	750 (5,89)	748	747 (B_2)		635	706
	42	38	Benzene ring bend	698 m	699 (5)	-696	699 (11,6)	704	717 (A_2)		574	
	43	40	Benzene ring bend	536 w	537 (6)	-535	536 (1,4)	522	553 (A_2)	374	375	363
	44	43	Benzene ring bend	435 mw	436 (1)	-430	436 (3,2)	433	(463) (B_2)	255	231	
	45	45	Sat. ring twist		356 (4)	-351	347 (6,7)	233	297 (B_2)	339	338	306
	46	46	Sat. ring flap		284 (4)	-274	275 (3,4)	155	317 (A_2)	194	192	
	47	47	Sat. ring twist		178 (14)	-158	158 (1,8)	-	166 (A_2)	102	111	139
	48	48	Sat. ring bend			-108	106 (3,8)	-	104 (B_2)	96	98	80

[a] b3lyp/6-311++G(d,p). Scaling factors are 0.985 for vibrations below 2800 cm^{-1} and 0.964 for vibrations above 2800 cm^{-1}.
[b] Values are taken from reference 16.
[c] CIS/6-311++G(d,p). Scaling factors are 0.940 for vibrations below 2800 cm^{-1} and 0.900 for vibrations above 2800 cm^{-1}.
[d] Assigned twice.
* Coupled vibrations.

agreement with the experimental data. However, it appears that a scaling factor as low as 0.9 would be required to match the higher frequencies. As before the 13BZN and 14BZD frequencies for the excited state are quite similar. For both molecules it should be noted that the frequency ordering changes in the excited state. This has been verified by examination of the SVLF spectra which provide strong evidence for the vibrational assignments. For example, excitation of the 255 cm^{-1} FES band results in a strong SVLF band at -430 cm^{-1} which corresponds to a benzene ring bending mode. At the same time the 345 cm^{-1} FES band results in a strong band at -361 cm^{-1} (saturated ring bending), confirming that the benzene ring bending mode has dropped below this one in frequency.

For most of the vibrations in the $S_1(\pi,\pi^*)$ state there is a modest frequency drop in the excited state reflecting a small decrease in the magnitude of the force constants. However, as can be seen, there are four low-frequency vibrations for which the frequency decrease is substantial. These include the skeletal twisting from 536 to 374 cm^{-1} and the benzene ring bending from 435 to 255 cm^{-1}. Both of these are the results of reduced π bonding within the benzene ring system. Similarly, the ring flapping drop from 274 to 194 cm^{-1} results from the reduced stiffness of the benzene ring. The fourth vibration which drops significantly is the twisting of the saturated ring from 158 to 102 cm^{-1}. As described in our LIF study of the low-frequency modes, this is due to the lower barrier to planarity in the S_1 state.[3]

CONCLUSIONS

Analysis of the infrared, Raman, LIF, and SVLF spectra of 13BZN along with *ab initio* and DFT calculations has allowed us to achieve a complete vibrational assignment for the S_0 electronic ground state. We have also been able to provide experimental vibrational assignments for a dozen modes in the $S_1(\pi,\pi^*)$ state and to provide calculated values for the others. In the $S_1(\pi,\pi^*)$ state the largest frequency changes are the result of the decreased π bonding of the benzene ring in the excited state.

CHAPTER V

RAMAN AND INFRARED SPECTRA AND THEORETICAL CALCULATIONS OF DIPICOLINIC ACID, DINICOTINIC ACID, AND THEIR DIANIONS*

INTRODUCTION

The infrared and Raman spectra of crystalline dipicolinic acid (DPA), also named 2,6-pyridinedicarboxylic acid, and its calcium salt as a trihydrate (CaDPA) were originally reported by Carmona[17] in 1980. With the help of a d_2 isotopomer and group frequency considerations a tentative vibrational assignment was proposed. In recent years there has been renewed interest in detecting the presence of DPA and its salts due to their presence in bacterial spores. DPA in biological systems was first discovered by Udo[18] in 1936 and its presence in bacterial spores was reported by Powell[19] in 1953. Anthrax spores contain both DPA and CaDPA and interest in detecting these spores has resulted in recent Raman investigations by Ghiamati et al.[20] and Kolomenskii et al.[21,22]. Theoretical computations by Hameka et al.[23] and Xie and co-workers[24] have also been carried out for DPA and its anion.

Takusagawa and co-workers[25] determined the crystal structure of dipicolinic acid monohydrate (DPA·H_2O) in 1972 and found the pyridine ring in DPA to have C_{2v} symmetry. Hydrogen bonding of the water molecule to both the nitrogen atom and

---

*Reprinted with permission from "Raman and infrared spectra and theoretical calculations of dipicolinic acid, dinicotinic acid, and their dianions" by Kathleen McCann and Jaan Laane, 2008. Journal of Molecular Structure, 890, 346-358,

the C=O of the DPA was found as well as from the oxygen in water to the OH groups of the DPA. Thus, the intermolecular interactions were very strong. In 2002 Tellez et al.[26] reported the crystal structure of anhydrous DPA. For this structure the molecule is planar, but loses its C_{2v} symmetry as the carboxylic acid groups are oriented in opposite directions. There is extensive hydrogen bonding between the carboxylic acid groups on neighboring DPA molecules.

The CaDPA crystal structure was reported in 1968 by Straks and Dickerson[27]. For this system the presence of the calcium cation causes the CO_2 groups on the two sides of the pyridine ring to have somewhat different geometries, but on the whole, the dipicolinate ion was found to be essentially planar.

Dinicotinic acid (DNic), or 3,5-pyridinedicarboxylic acid, is very similar to DPA and only differs in where the two carboxylic acid groups are attached to the pyridine ring. This molecule is also of interest since it is desirable to distinguish it from DPA when the presence of anthrax spores is suspected. Takusagawa and co-workers[28] reported the crystal structure of DNic in 1973. The molecule in the crystal was found to have a nearly planar structure intermediate between the neutral molecule and the zwitter ion where hydrogen bonding from the OH groups to the pyridine nitrogen atom is present. This results in some asymmetry of the individual molecules which have nearly C_{2v} symmetry. A recent neutron diffraction study by Cowan and co-workers[29] is consistent with these results.

In the present study the investigation of DPA and DNic and their anions was undertaken with the goal of not only understanding their structures and spectra, but also

to aid in the detection of anthrax spores. These spores contain both DPA and CaDPA in a somewhat uncertain environment, and when detecting the spores an understanding of what spectral features can be expected to arise is needed.

Experimental results are reported on the Raman and infrared spectra of solid DPA and its calcium and sodium salts and compared with those of Carmona[17]. The analysis of the spectra were aided by high level DFT calculations on individual non-hydrated DPA and the DPA^{-2} anion. Since the actual spectra of DPA and DPA^{-2} include those of the hydrated forms in the solid state, intermolecular interactions between the carboxylate groups and water molecules are expected. Moreover, hydrogen bonding interactions between the individual DPA molecules (or between the DPA^{-2} molecules) are anticipated based on the crystal structures, and these will significantly affect the spectra of the DPA and DPA^{-2} solid samples. In order to investigate these effects and to understand why the experimental spectra of the solid agree more poorly than usual with the computed DPA spectra of the individual molecules, separate computations on DPA dimers as well as $DPA \cdot 2H_2O$ have been carried out. Additionally, experimental results and computations on dinicotinic acid (DNic) and its anion $DNic^{-2}$ are reported. These results will help show how DPA and DPA^{-2} can be distinguished spectroscopically from the very similar DNic and its anion.

EXPERIMENTAL

DPA and DNic were purchased from Aldrich and used without further purification. The DPA^{-2} and $DNic^{-2}$ anions were prepared from the acids by reaction

with stochiometric amounts of NaOH in solution. The calcium salts were prepared by further reaction of the anions with a stochiometric amount of powdered $CaCl_2$. Salt crystals formed as the solution was allowed to evaporate. The Raman spectra of solid samples were recorded using a Jobin-Yvon U-1000 spectrometer equipped with a CCD. A Coherent Innova 20 argon ion laser (514.5 nm, 0.5 w) or a Coherent Verdi V-10 Nd:YAG system (532 nm, 0.5w) was used for excitation. Raman spectra were also recorded with a JY Horiba LabRam HRFTIR microscope equipped with CCD detection with spectral resolution of 0.3 cm^{-1}/pixel at 680 nm. A helium-neon laser operating at 633 nm with 17 mw of power was the excitation source. Infrared spectra of KBr pellets of the samples were recorded with a Bruker Vertex 70.

CALCULATIONS

DFT calculations using the B3LYP hybrid functional were carried out using the Gaussian 03 program[13]. All structural optimizations and frequency calculations were done using the 6-311++G(d,p) basis set. Calculations were run for dipicolinic acid (DPA) and its dianion (DPA^{-2}), dinicotinic acid (DNic) and its dianion ($DNic^{-2}$) as well as the DPA dimer and a DPA-water complex.

STRUCTURES

Figure 11 shows the calculated structures for the single DPA molecule and its DPA^{-2} anion using the B3LYP/6-311++G(d,p) basis set. The computed bond distances

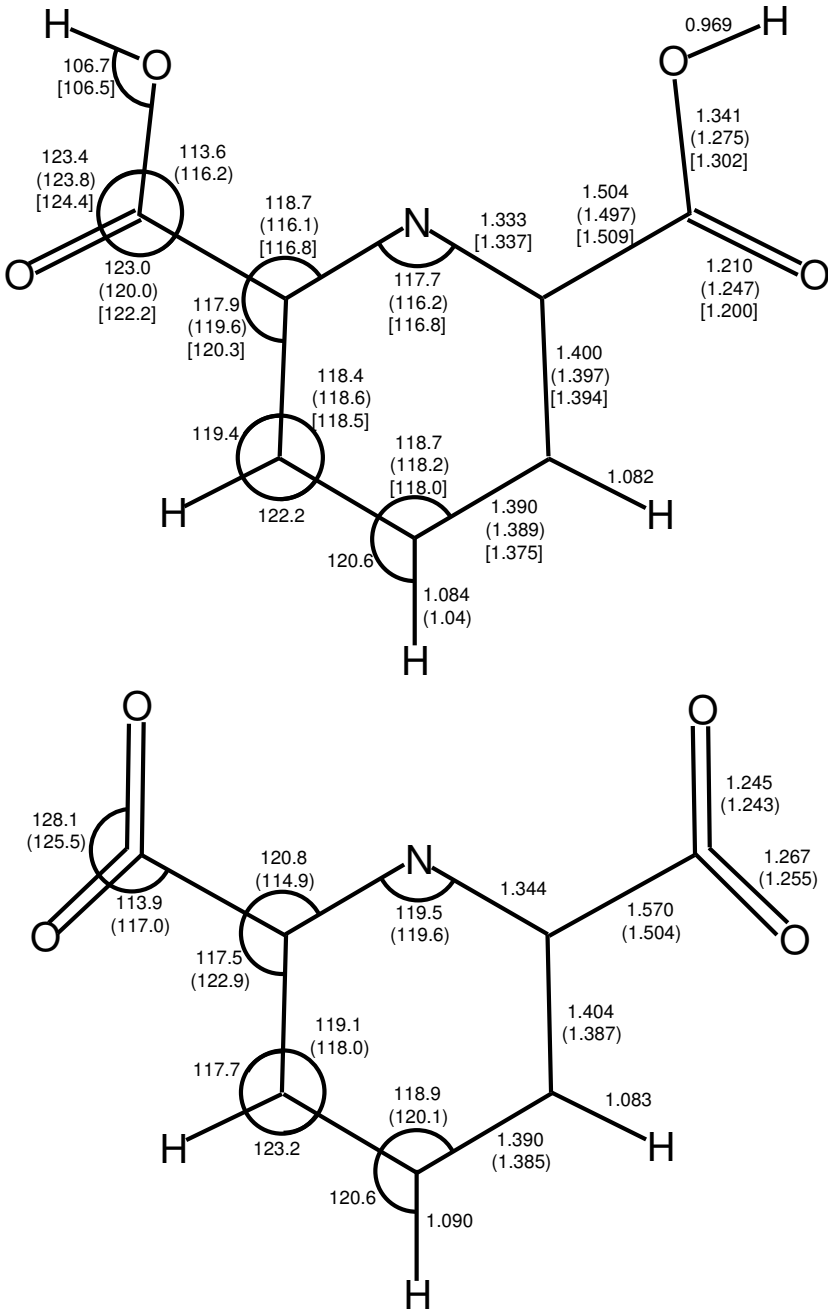

Figure 11. Calculated structures for DPA and the DPA^{-2} anion using B3LYP/6-311++G(d,p). Geometrical parameters from the crystal structures of anhydrous DPA and DPA monohydrate are shown in parentheses and brackets, respectively.

and angles are shown in the figure along with the values from the crystal structures[25] of the anhydrous DPA (in parentheses) and the DPA monohydrate [in brackets]. For DPA^{-2} the crystal structure values for the CaDPA trihydrate[27] are shown in parentheses. In the crystals of the $DPA \cdot H_2O$ and $CaDPA \cdot 3H_2O$ the individual molecules are asymmetrical so that bond lengths and bond angles are slightly different on one side of the pyridine ring as compared to the other. In the figures the values shown are the averages for the two sides. It should also be noted that in the crystals, because of intermolecular interactions with water or other DPA molecules, the two carboxylic acid groups are rotated with respect to each other destroying the C_{2v} symmetry. For our calculation, C_{2v} symmetry was used. Despite these differences the calculated geometrical parameters agree very nicely with the crystal structures. The main differences occur for the carboxylic acid groups, as expected, since these are involved in hydrogen bonding interactions with water or neighboring molecules in the crystals.

The calculated structural parameters for DPA^{-2} are also shown in Figure 11. The calculation was carried out for a single ion and ignored the interactions with the Ca^{+2} cation and the water molecules in the calcium DPA trihydrate. Nonetheless, the agreement between the calculation and the crystal structure determination can be seen to be very good.

In similar fashion Figure 12 shows the calculated structures for DNic and $DNic^{-2}$. In this case DNic for both the calculation and the crystal structure has very nearly C_{2v} symmetry with the same orientation for the two carboxylic acid groups. The agreement between experimental[28] and calculated values is again very good except at the carboxylic

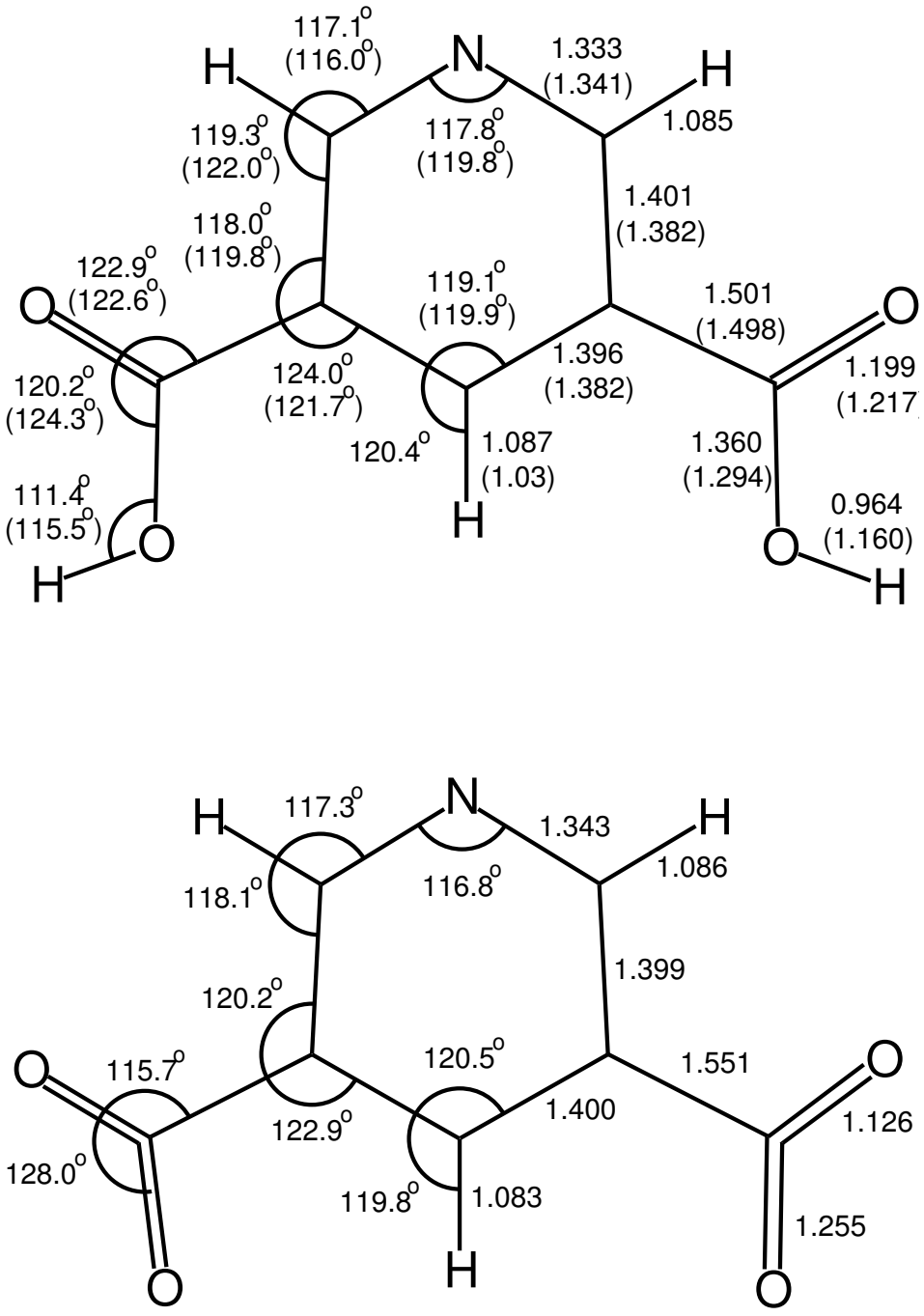

Figure 12. Calculated structures for DNic and the $DNic^{-2}$ anion. Values in parentheses are from the crystal structure.

acid groups which get involved in intermolecular hydrogen bonding. For example, C-OH and C=O calculated bond distances of 1.360 Å and 1.199 Å, respectively, can be compared to the crystal structure values of 1.294 Å and 1.217 Å reflecting these interactions. Figure 12 also shows the calculated structure of an individual $DNic^{-2}$ anion, for which no crystal structure determination has been reported, although Starosta and co-workers[30,31] have reported structures for DNic calcium complexes. The $DNic^{-2}$ values are similar to those of DPA^{-2} as expected.

VIBRATIONAL MODES

For the purpose of vibrational assignments the DPA molecule can be assumed to have C_{2v} symmetry and lie in the xy plane. Its vibrational symmetry species then are

$$16A_1 + 6A_2 + 8B_1 + 17B_2.$$

The A_1 and B_2 vibrations are the in-phase modes while A_2 and B_1 represent out-of-plane modes. All the vibrations are Raman active and all but the A_2 are infrared active. The A_1 modes are Raman polarized. The DNic molecule has exactly these same vibrational symmetry species.

Similarly, the vibrations of the DPA^{-2} and $DNic^{-2}$ anions in C_{2v} symmetry have the symmetry species

$$14A_1 + 4A_2 + 6B_1 + 13B_1.$$

All of the vibrational frequencies and infrared and Raman intensities for DPA, DPA^{-2}, DNic, and $DNic^{-2}$ were computed to assist in the analysis of the spectra. Figures 13A and 13B present vector pictures to represent all 45 vibrations of a single non-interacting

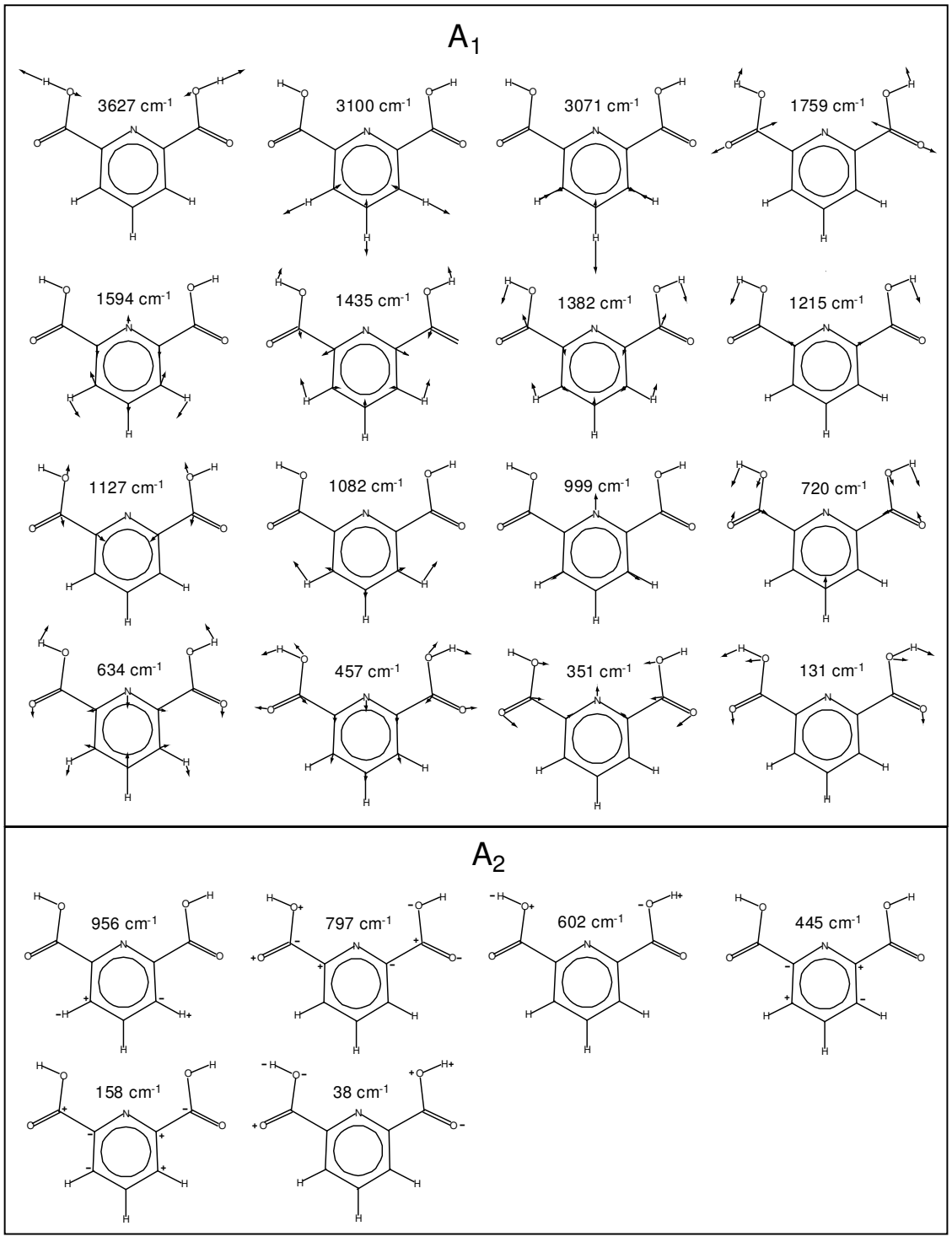

Figure 13A. Vector representation for the A_1 and A_2 vibrations of DPA based on C_{2v} symmetry.

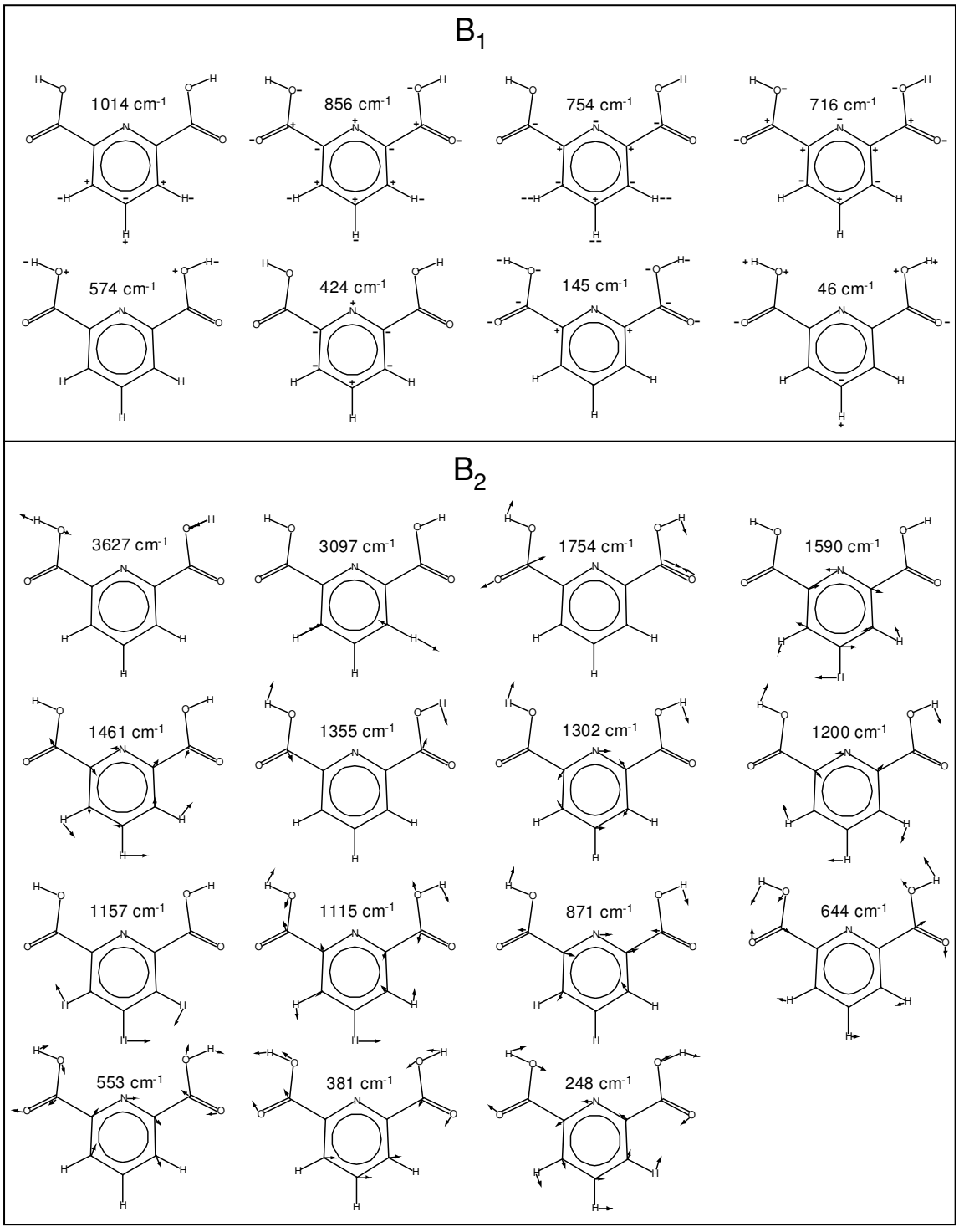

Figure 13B. Vector representation for the B_1 and B_2 vibrations of DPA based on C_{2v} symmetry.

DPA molecule. Figures 14A and 14B present representations for the 39 vibrations of the DPA^{-2} anion. The figures also show the corresponding calculated frequency for each vibrational mode. The vibrational modes for DNic and $DNic^{-2}$ are very similar.

VIBRATIONAL SPECTRA

Figures 15 to 22 show the experimental Raman and infrared spectra (KBr pellets) of DPA, DPA^{-2}, DNic, and $DNic^{-2}$. The Raman spectra shown are those collected with the Raman microscope. Those recorded with the JY U-1000 have higher resolution but also show a fluorescence background, especially for DNic. In each case the observed spectrum is compared to the computed spectrum. The infrared spectra of both the KBr pellets (shown) and the nujol mulls of these molecules show a number of broad features resulting from the presence of the hydrated water in these samples. For molecular systems which have studied previously[32-42] remarkably good agreement has typically been found between the observed and calculated spectra. Here, however, there are significant differences which can be attributed to the intermolecular hydrogen bonding. Some key features, such as the ring breathing of the pyridine ring which produces the most intense Raman band at 998 cm^{-1}, are predicted quite accurately. However, others are significantly shifted in frequency due to hydrogen bonding between neighboring molecules or with water molecules in the hydrates. In particular, the vibrations associated with the carboxylic acid groups are affected the most by these intermolecular interactions. Our spectra do not differ significantly from those of Carmona[17], which are of high quality, but we have the benefit of the DFT calculations in making the

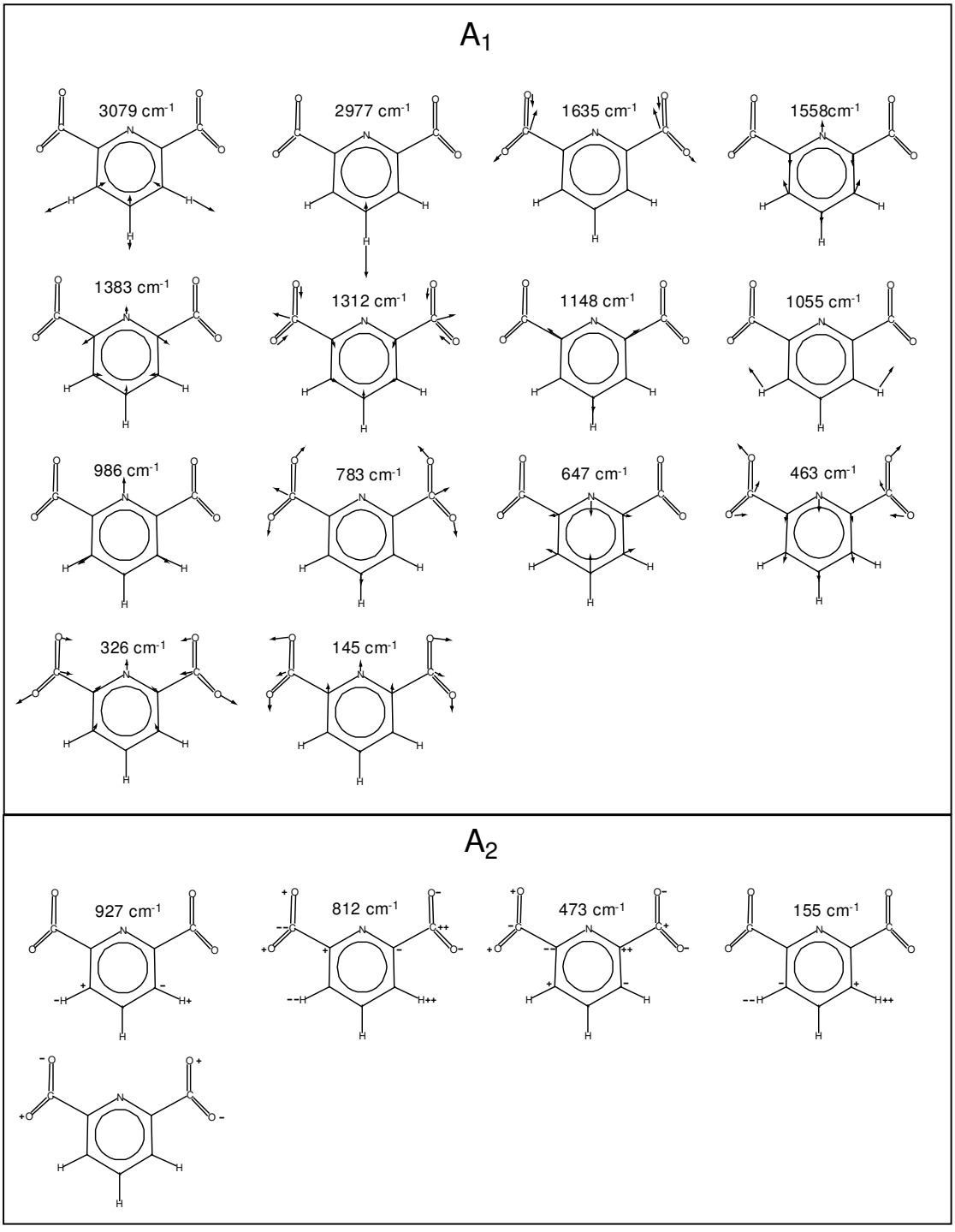

Figure 14A. Vector representation for the A_1 and A_2 vibrations of the DPA^{-2} anion based on C_{2v} symmetry.

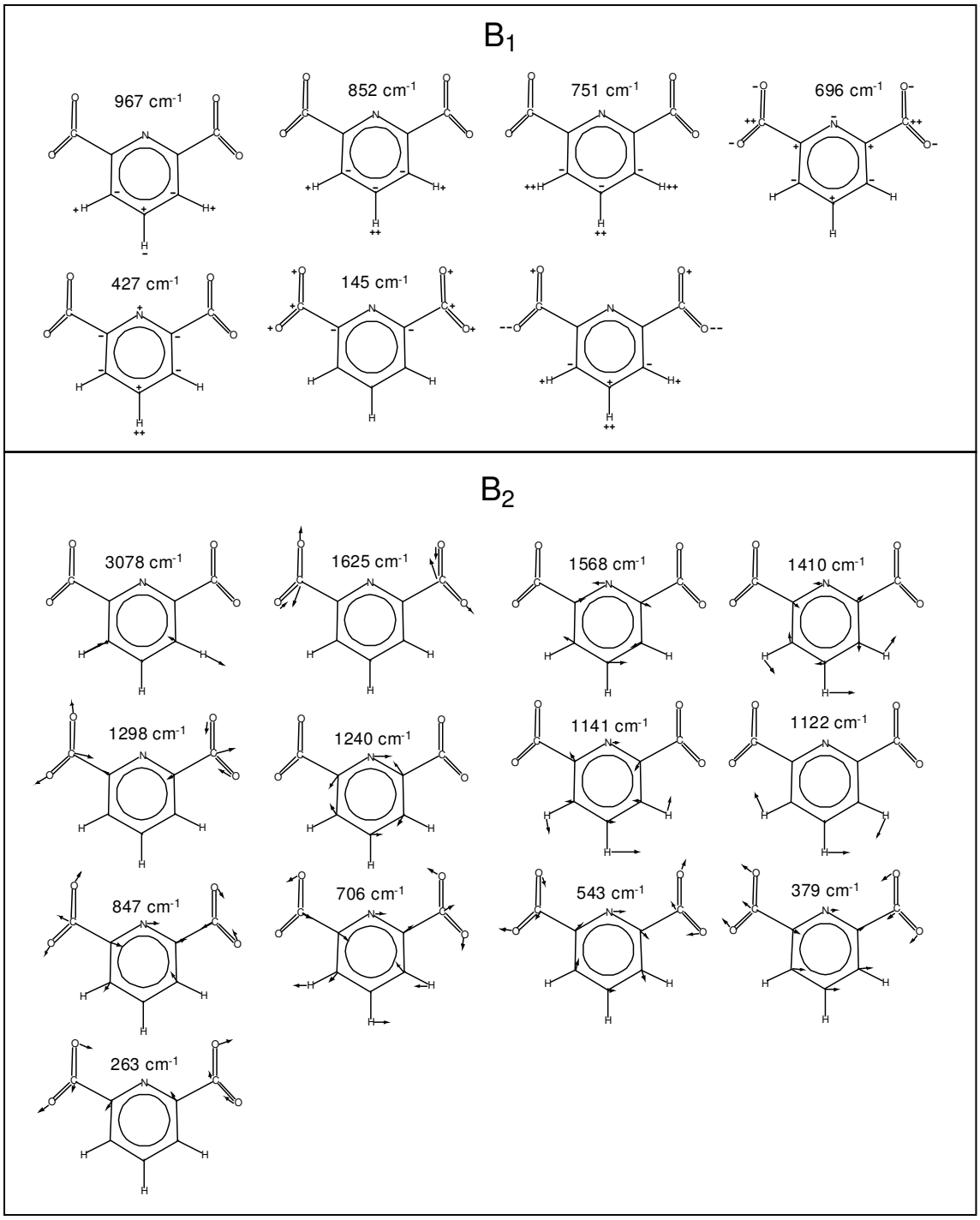

Figure 14B. Vector representation for the B_1 and B_2 vibrations of the DPA^{-2} anion based on C_{2v} symmetry.

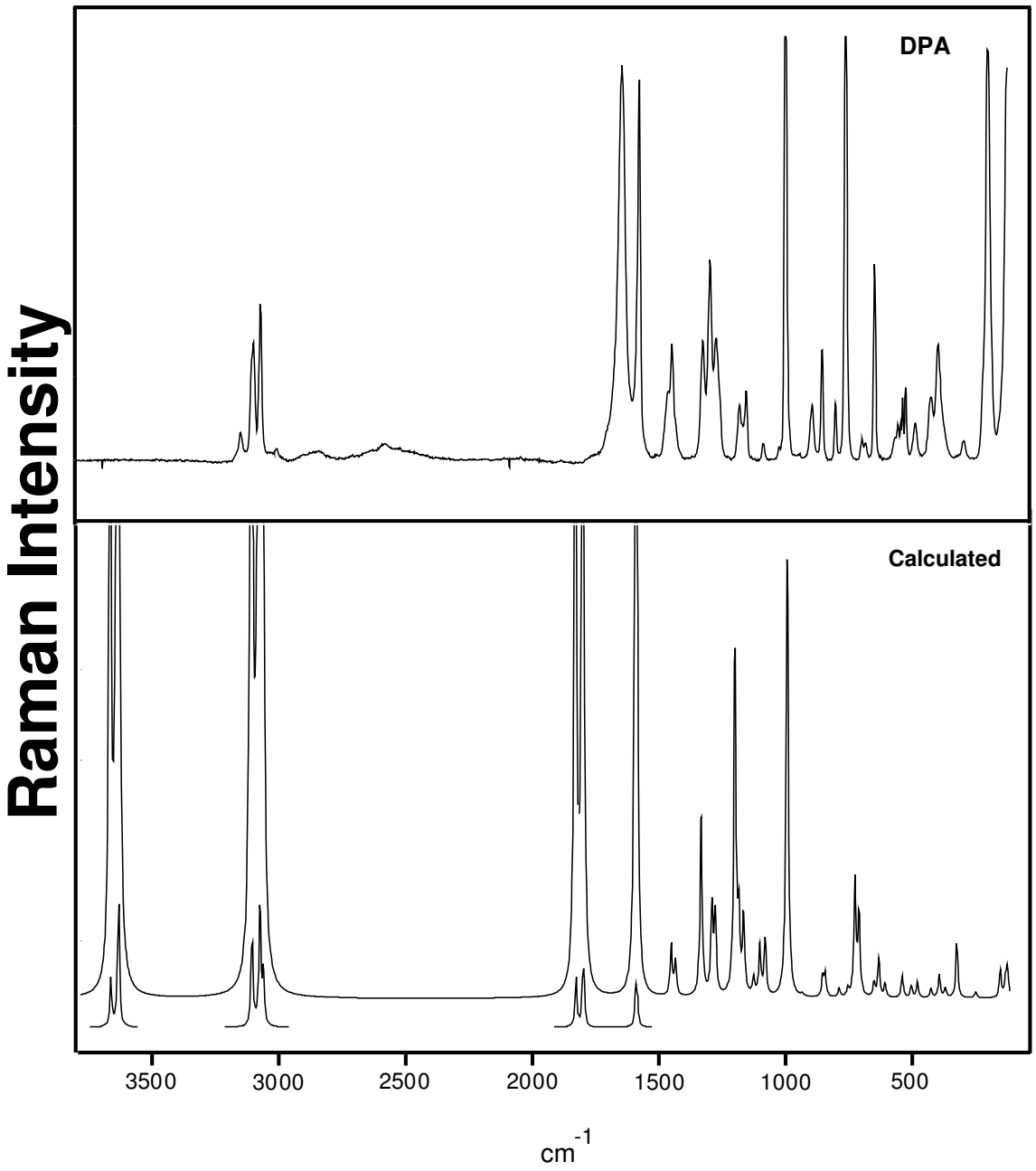

Figure 15. Raman spectrum of DPA powder compared to its computed spectrum.

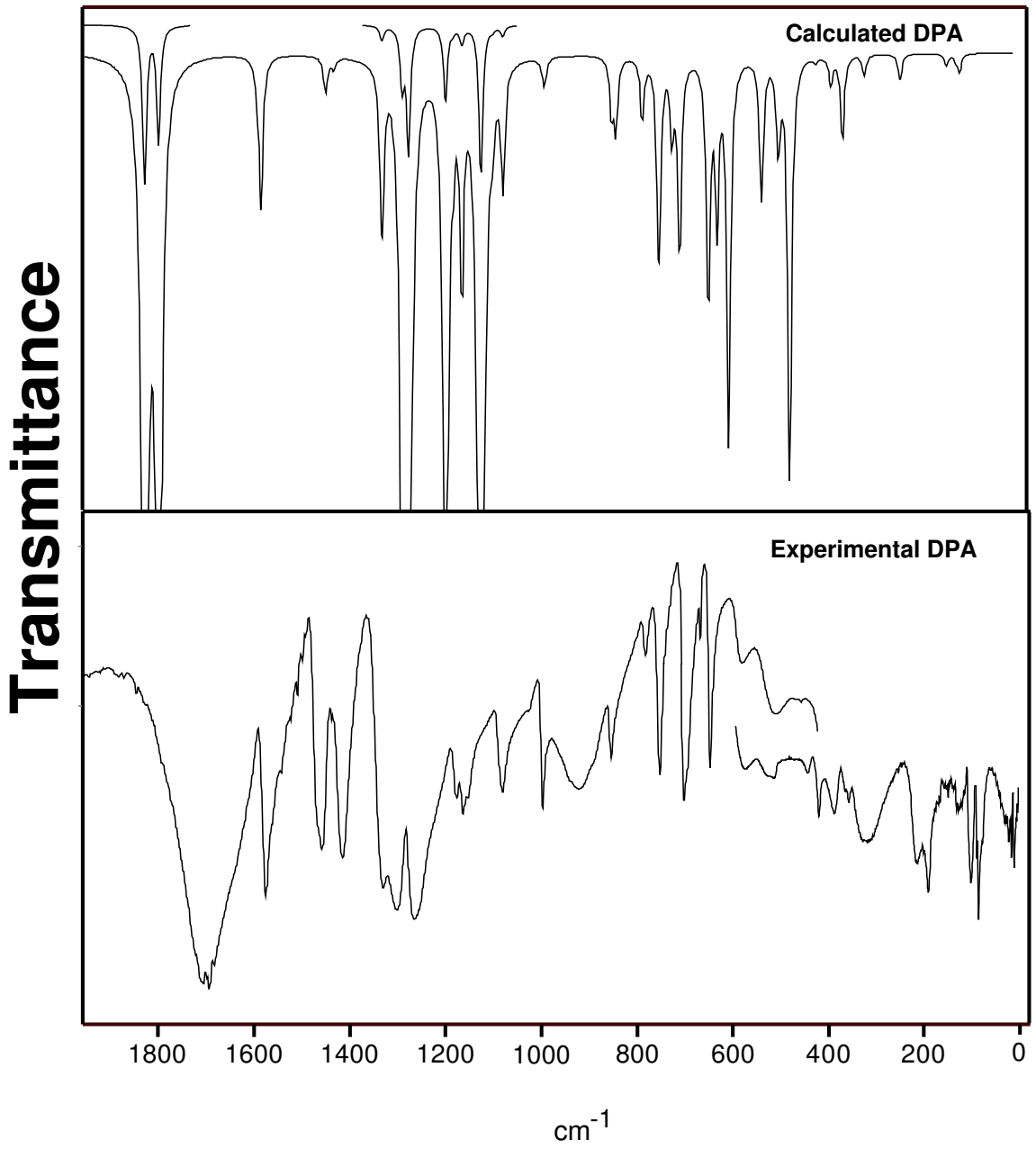

Figure 16. Infrared spectrum of DPA in a KBr pellet compared to its computed spectrum.

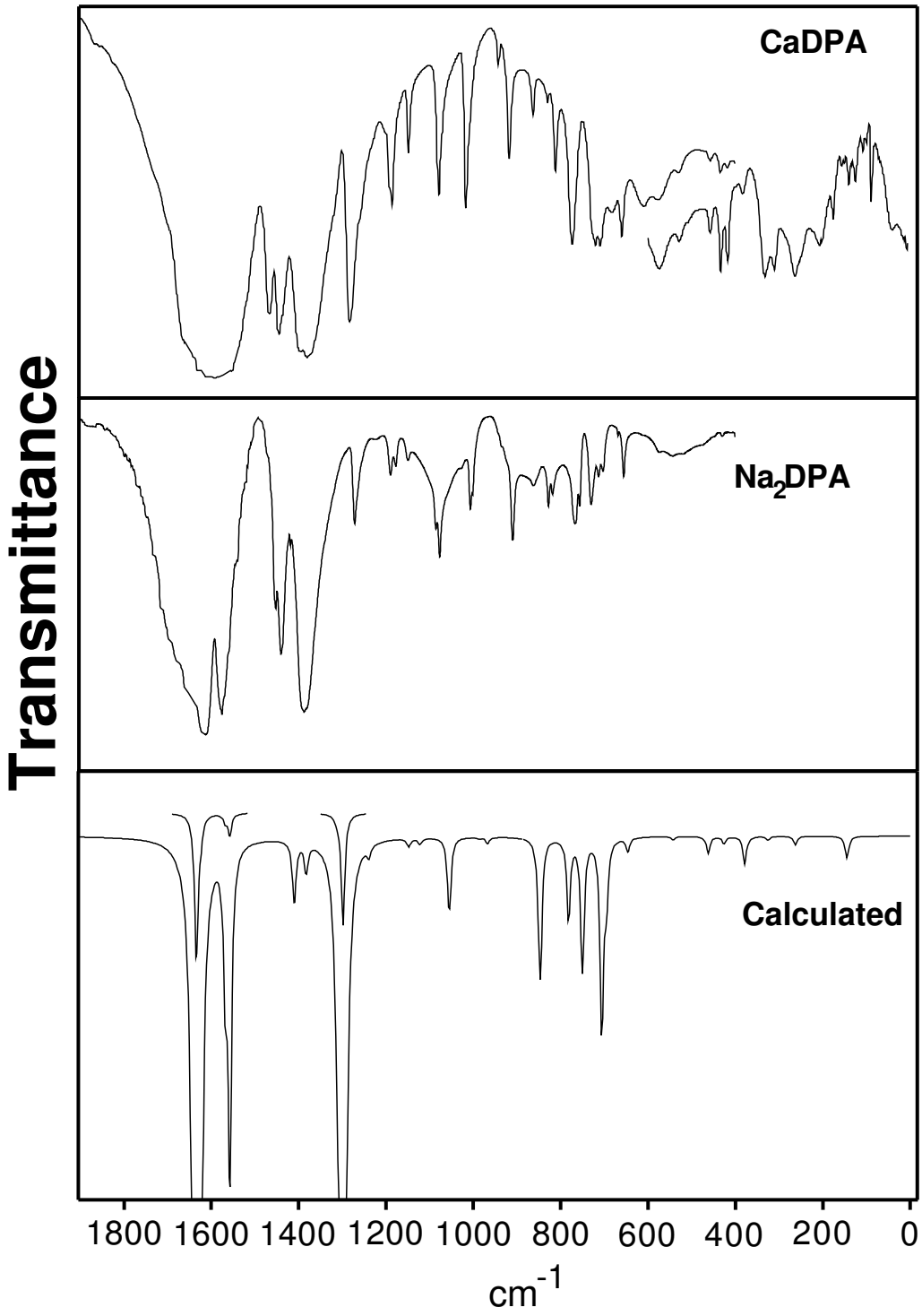

Figure 17. Raman spectra of the calcium and sodium salts of DPA^{-2} compared to the computed spectrum of free DPA^{-2}.

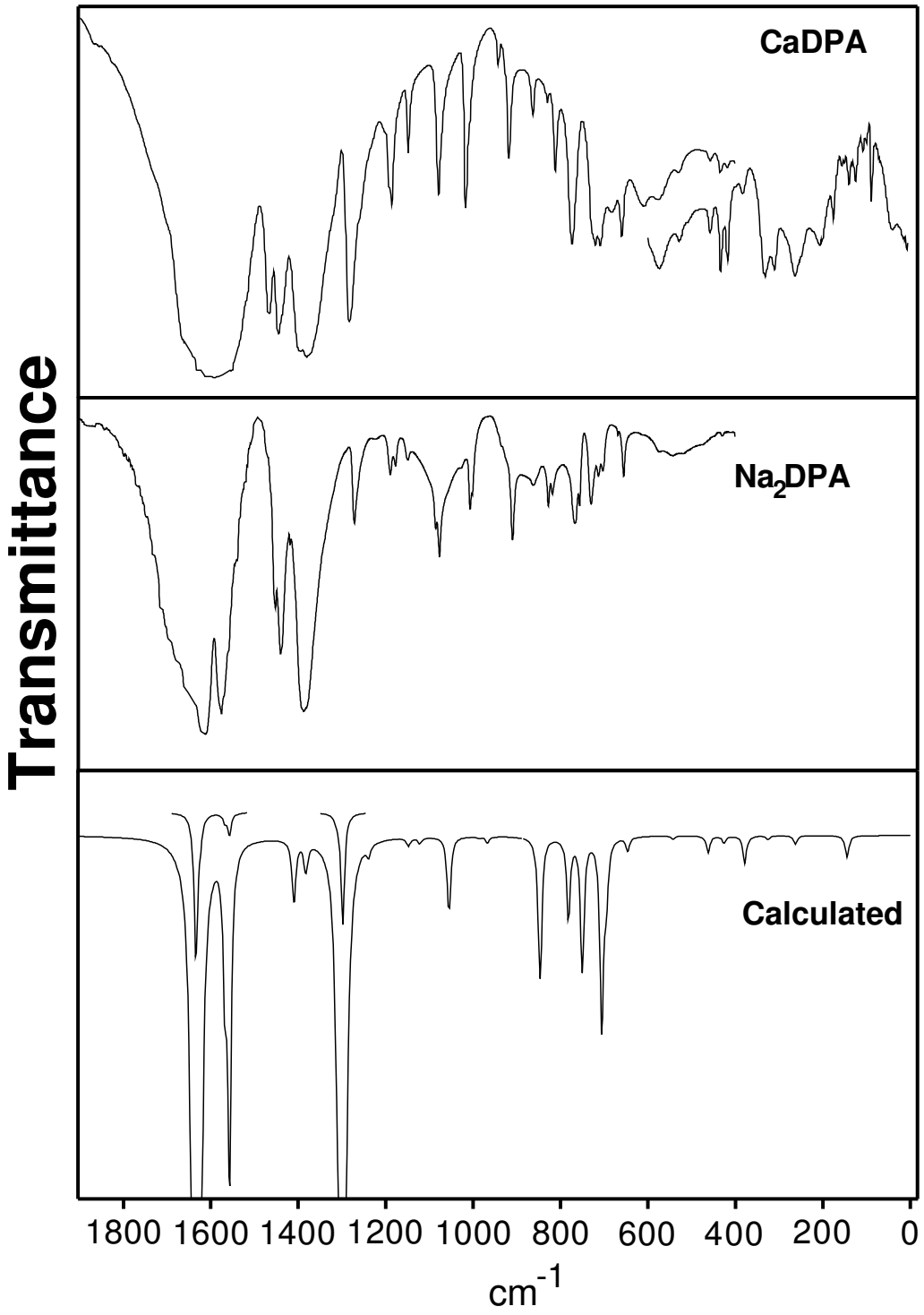

Figure 18. Infrared spectra of the calcium and sodium salts of DPA^{-2} compared to the computed spectrum of free DPA^{-2}.

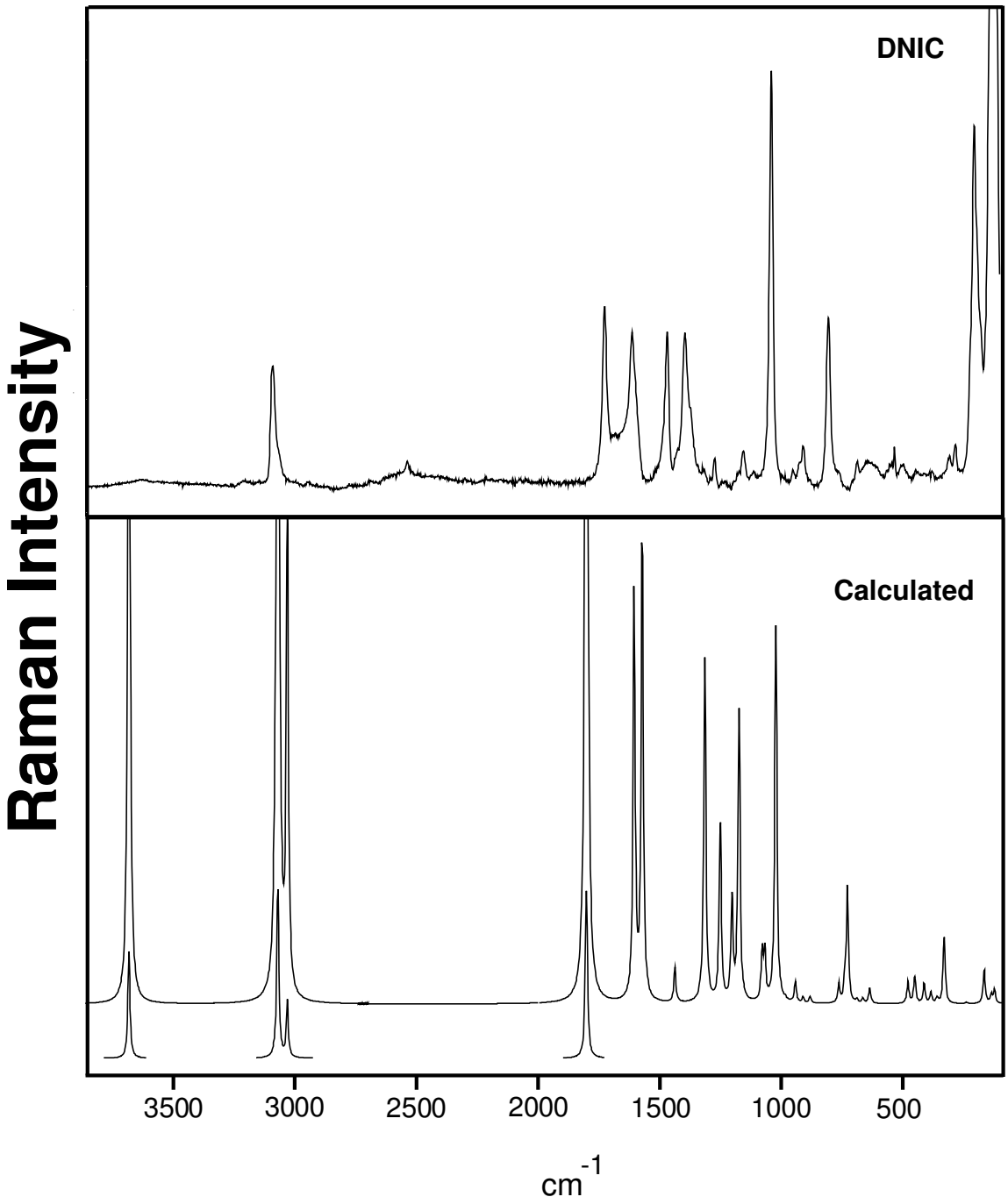

Figure 19. Raman spectrum of DNic powder compared to its computed spectrum.

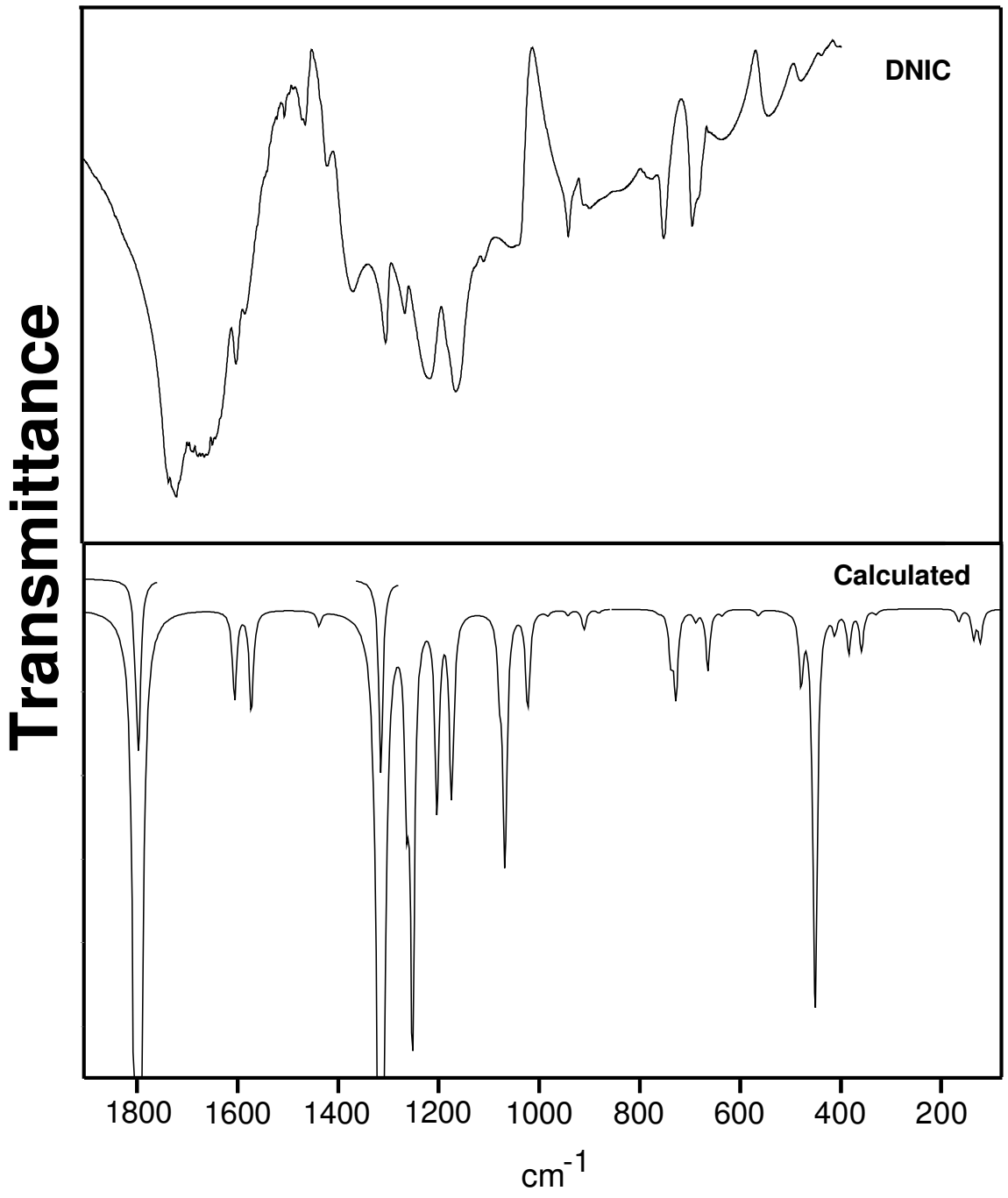

Figure 20. Infrared spectrum of DNic in a KBr pellet compared to its computed spectrum.

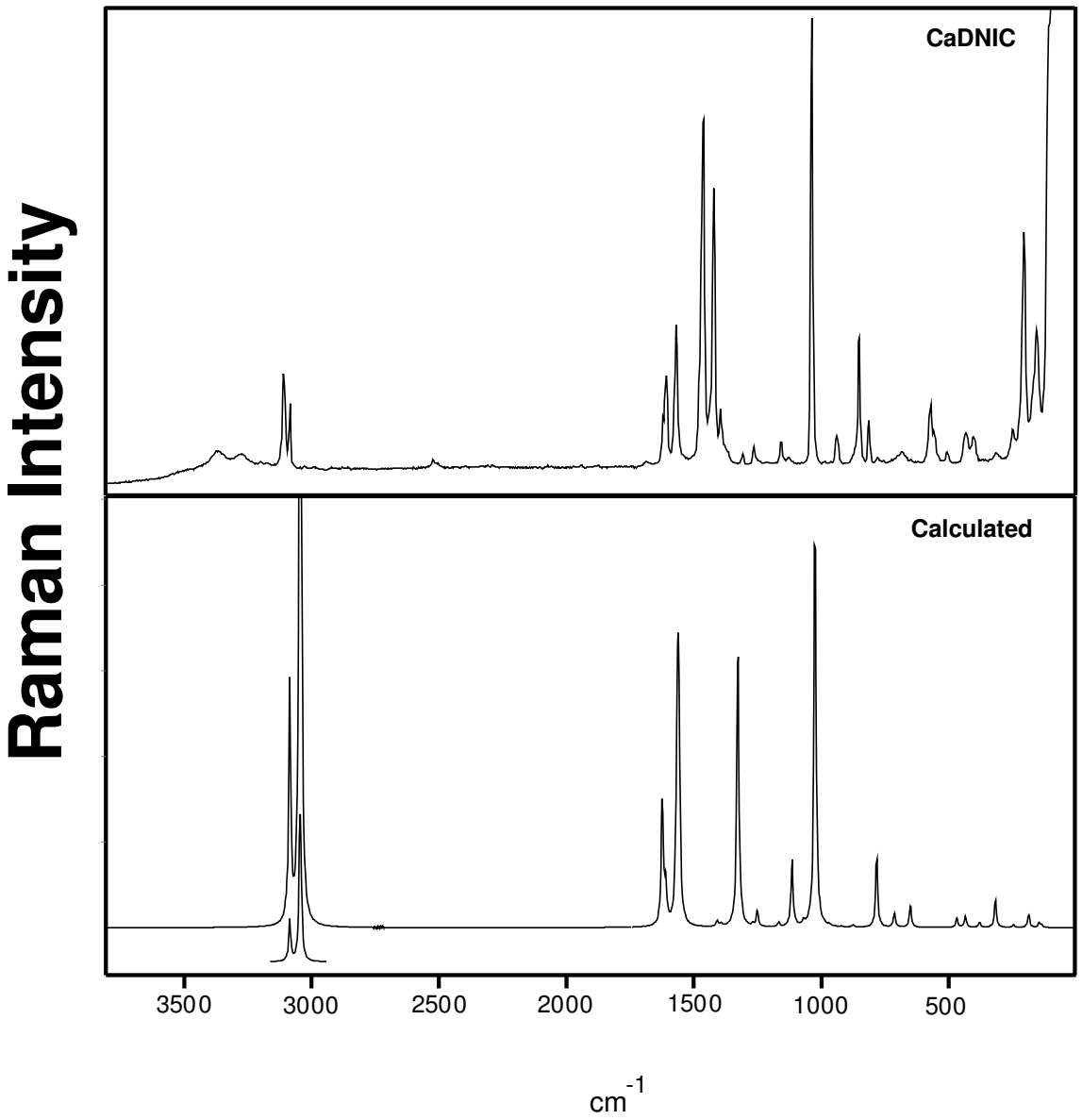

Figure 21. Raman spectrum of the calcium salt of $DNic^{-2}$ compared to the computed spectrum of free $DNic^{-2}$.

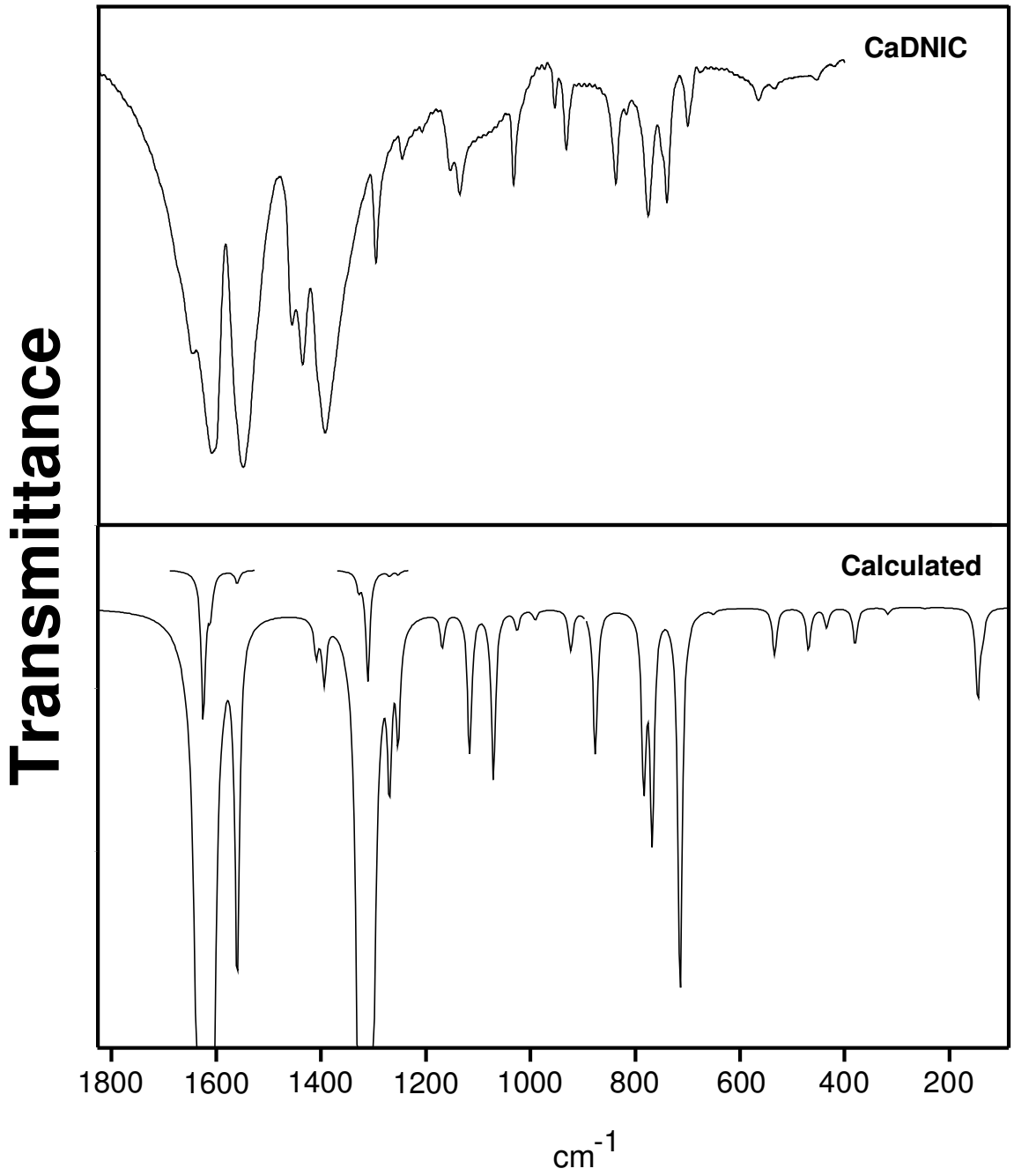

Figure 22. Infrared spectrum of the calcium salt of $DNic^{-2}$ compared to the computed spectrum of free $DNic^{-2}$.

vibrational assignments. Table 10 presents a comprehensive summary of our infrared and Raman assignments for DPA and these are compared to values reported by Carmona[17] as well as our calculated frequencies for a single, non-interacting molecule. Table 10 also includes the assignments for DNic. Table 11 presents the observed and calculated frequencies for CaDPA, NaDPA, and CaDNic. For CaDPA the experimental values are compared to those of Carmona.

Several comments should be made about the vibrational assignments. As noted previously, in the crystal structures the individual molecules exist in different environments so that the vibrations of one -CO_2H group, for example, will have somewhat different frequencies from another. This can give rise to doublets or broad bands in the spectra. In assigning the spectra, we have not attempted to list all the possible bands associated with such features, but have selected the principal bands that can be ascribed to the vibrations. These variations in the molecular environments will also lead to apparent infrared and Raman frequency differences. For example the ν_{35} skeletal stretching band of CaDNic is assigned as 837 cm^{-1} (IR) and 851 cm^{-1} (Raman), apparently and these are assumed to arise from this motion for the molecule in different crystal environments. Apparently, in one crystal arrangement the lower frequency is enhanced in the infrared spectrum while in another the Raman is enhanced. It should also be pointed out that the assignment of low-frequency modes below 200 cm^{-1} is rather arbitrary since these will be highly coupled to the lattice modes of the molecules. The DFT calculations are those for individual non-interacting molecules and the predicted frequencies will be very different from the experimental ones. It should also be noted

Table 10.Calculated (scaled) and observed frequencies (cm^{-1}) for solid DPA and solid DNic.

		Description	DPA					DNic		
			IR[a]	Raman[b]	$\overline{\nu}_{CALC}$ C_s[c]	C_{2v}[c]	Carmona[d]	IR[a]	Raman[b]	$\overline{\nu}_{CALC}$[c]
A_1	1	O-H stretch		3417 (31)	3665 (12,83)	3627	2800			3684 (6,60)
	2	C-H stretch (i.p.)	3108 vw	3104 (17)	3108 (0.1,145)	3100	3113	3092 m	3090 (29)	3072 (0.06,78)
	3	C-H stretch		3098 (10)	3062 (0.7,88)	3071	3070			3032 (0.6,35)
	4	C=O stretch	1640 m	1645 (31)	1830 (100,8)	1759	1640	1725 s	1725 (43)	1804 (24,100)
	5	Ring stretch	1565 m	1575 (39)	1587 (8,35)	1594	1580	1585sh	1611 (37)	1573 (6.2,30)
	6	Ring stretch(+Ring-C)	1457 vs	1454 (4)	1435 (0.6,3.7)	1435	1447	1459 mw	1469 (35)	1439 (0.4,2)
	7	O-H in-plane wag	1330 m	1324 (10)	1334 (9,20)	1382	1423		1394 (33)	1315 (100,22)
	8	Ring + CH wag	1269 m	1271 (10)	1201 (49,37)	1215	1262	1220 m		1204 (12,7)
	9	C-O stretch	1151 mw	1153 (5)	1102 (2.2,5)	1127	1304		1155 (8)	1175 (10,18)
	10	Ring + C-O	1080 m	1083 (2)	1081 (6,6)	1082	1082			1068 (15,3)
	11	Ring breathing	996 m	998 (100)	994 (1.6,47)	999	998	~1040 br	1039 (100)	1023 (16,25)
	12	Skeletal (Ring-C)		760 (66)	727 (3.8,12)	720	895		685 (5)	729 (5,7)
	13	Ring bending	648 m	647 (28)	633(9,4)	634	647	~630 br	~630 br	637 (0.3,1.0)
	14	Skeletal bend (O-C-O)		486 (3)	480 (23,1.6)	457	762	~535 br	532 br	452 (21,1.4)
	15	Skeletal bending (O-C-O)	358	397 (10)	325 (1.1,6)	351	298		307 (4)	330 (0.3,4.2)
	16	Skeletal bend (Ring-C)		202 (41)	126 (1.0,3.0)	131	495		124 (198)	123 (2,0.9)
A_2	17	C-H out-of-plane wag	889 vw	895 (17)	935 (0.1,1.4)	956	802		950 (3)	983 (0.3,0.2)
	18	Skeletal wag (o.p.)	784 w	801 (8)	789 (3.3,0.9)	797	630		(754)	764 (0.1,1.2)
	19	O-H wag (o.p.)			608 (21,1.4)	602	937			565 (0.4,0.02)
	20	Ring deformation (o.p.)	419	425 (4)	427 (0.3,1.0)	445	396			359 (2.4,0.34)
	21	Skeletal bend	190	193 (21)	153 (0.7,2.8)	158	365			166 (0.8, 2.2)
	22	O-C-O torsion			35 (0.3,1.6)	38	---			37 (0.2,0.3)
B_1	23	C-H wag (o.p.)	996 m	998	1006 (0.1,0.3)	1014	987	943 mw		943 (0.3,1.3)
	24	Skeletal-C inversion	854 mw	854 (11)	854 (2.9,2.1)	856	855	~908 br	907 (9)	911 (1.2,0.4)
	25	C-H wag	752 m		755 (12,0.9)	754	751	753 m	754 sh	739 (2.7,1.1)
	26	Skeletal twist	701 m	699 (2)	711 (10,9)	716	692	696 m		690 (0.6,0.2)
	27	O-H wag (o.p.)	577 m		540 (8,2.3)	574	583		496 (4)	480 (4,1.4)
	28	Skeletal twist	386		394 (1.6,2.5)	424	421	439 w	439 (2)	413 (1.2,1.3)
	29	O-C-O wag (o.p.)			133 (0.3,1.6)	145				136 (1.7,0.6)
	30	O-C-O torsion			40 (0.5,1.9)	46	226			52 (1.9,1.3)

Table 10. Continued.

		Description	DPA					DNic		
			IR[a]	Raman[b]	$\bar{\nu}_{CALC}$ C_s[c]	C_{2v}[c]	Carmona[d]	IR[a]	Raman[b]	$\bar{\nu}_{CALC}$[c]
B_2	31	O-H stretch		Hbond	3634 (32,210)	3627	2650			3681 (4,8)
	32	C-H stretch	3066 w	3070 (12)	3077 (1.3,202)	3097	3105	3067 sh	3065 sh	3069 (0.01,37)
	33	C=O stretch	1690 ms	1693 (4)	1801 (74,100)	1754	1700	(1725)	(1725)	1797 (81,9)
	34	Ring stretch	1574 m	1575 (39)	1594 (1.3,64)	1590	1576	1603 m	~1603 sh	1607 (5,26)
	35	Ring stretch	1465 vs		1452 (2.0,5)	1461	1470	1468 mw	(1469)	1438 (0.5,0.4)
	36	O-H in-plane wag	1377 s	1296 (15)	1291 (35,9)	1355	1387	1371 mw	1371 (14)	1331 (0.6,0.2)
	37	Ring stretch	1301 m	1302 (4)	1278 (79,8)	1302	1275	1268 mw	1273 (7)	1264 (9,0.03)
	38	C-H wag (in-plane)	1255 m	1255 (5)	1185 (2.3,7)	1200	1178	~1220 br	~1222 br	1252 (26,12)
	39	C-H wag	1175 mw	1167 (3)	1166 (11,8)	1157	1156	1165 m		1170 (2,0.3)
	40	C-O stretch	1162 mw	1162 (3)	1127 (96,1.8)	1115	1308	1111 w	1111 (2)	1079 (4,3)
	41	Skeletal stretch	889 w	888 (4)	844 (3.9,2.3)	871	890			882 (0.2,0.4)
	42	Skeletal bend (ring + C=O)	648 m	647 (28)	652 (13,1.5)	644	668	~630 br	~630 br	665 (4,0.3)
	43	Ring-$C(O)_2$ wag (in-plane)	514 m	522 (5)	504 (5,1.3)	553	752	475 mw		449 (4,0.4)
	44	Skeletal bend	366		370 (5,1.0)	381	330			385 (3,0.7)
	45	O-C-O wag	215	222 (6)	250 (1.5,0.7)	248	530		282 (6)	239 (0.4,0.1)

[a] Abbreviations: s – strong , m – medium , w – weak , v – very, br – broad , sh – shoulder.
[b] Values in parentheses are relative intensities.
[c] Scaled frequencies, values in parentheses are relative IR and Raman intensities, respectively.
[d] Values from ref. [18].

Table 11. Calculated (scaled) and observed frequencies(cm^{-1}) for solid CaDPA, solid Na_2DPA and solid CaDNic.

		Description	CaDPA			DPA^{-2}		Na_2DPA		CaDNic		
			IR[a]	Raman[b]	Carmona[c]	$\bar{\nu}_{CALC}$ C_s[d]	C_{2v}[d]	IR[a]	Raman[b]	IR[a,e]	Raman[b,e]	$\bar{\nu}_{CALC}$[d]
A_1	1	C-H stretch (i.p.)	3085 vw	3084 (68)	3084	3066 (24,896)	3079		3083 (91)		3105 (209)	3086 (0.005,608)
	2	C-H stretch		3027 (6)	---	2981 (133,5477)	2977				3083 (142)	3045 (12,633)
	3	C=O stretch	1620 w	1617 (109)	1589	1616 (650,600)	1635	1624 vs	1638 (67)	1607s	1607 (192)	1625 (1000,305)
	4	Ring stretch	1563 m	1549 (66)	1567	1560 (116,235)	1558	1541 m	1577 (466)		1570 (314)	1560 (85,452)
	5	Ring stretch(+Ring-C)	1447 vs	1445 (262)	1445	1390 (35,81)	1383	1441 ms	1447 (801)	(1456 ms)	1464 (769)	1410 (9,14)
	6	Ring + CH wag	1395 s	1392 (269)	1398	1337 (78,536)	1312	1386 s	1399 (996)	1392 s	1393 (117)	1329 (114,702)
	7	C-O stretch	1191 mw	1193 (86)	1186	1164 (17,365)	1148	1190 w	1194 (216)		1156 (51)	1168 (9,12)
	8	Ring + C-O	1078 s	1073 (22)	1084	1072 (20,152)	1055	1086 m	1090 (96)		1125 (19)	1116 (36,166)
	9	Ring breathing	1015 s	1016 (1000)	1015	985 (0.1,1000)	986	1007 mw	1011 (1000)	1033 mw	1036 (1000)	1026 (5,1000)
	10	Skeletal (Ring-C)			822	782 (26,274)	783		777 (40)	775 m	777 (12)	784 (42,173)
	11	Ring bending	659 m	655 (61)	728	650 (8,92)	647	668 vvw	659 (114)		650 (7)	652 (1,55)
	12	Skeletal bend (O-C-O)			662	356 (10,22)	463	654 mw			433 (70)	470 (11,23)
	13	Skeletal bending (O-C-O)			408	316 (2,36)	326				313 (18)	318 (1.6,67)
	14	Skeletal bend (Ring-C)			260	125 (2,22)	145				155 (231)	137 (5,5)
A_2	15	C-H out-of-plane wag	861 w	856 (25)	816	886 (3, 61)	927	861 w	868 (76)			970 (0,4)
	16	Skeletal wag (o.p.)	810 m	818 (123)	531	804 (24, 61)	812	817 mw	822 (277)	816 vw	812 (98)	803 (0,0.1)
	17	Ring deformation (o.p.)		608 (12)	185	609 (2, 6)	473		471 (17)		403 (56)	438 (0,10)
	18	Skeletal bend		526 (39)	347	508 (4,0.3)	155				205 (453)	187 (0,31)
	19	O-C-O torsion			170	25 (6,33)	*i*					36 (0,7)
B_1	20	C-H wag (o.p.)	916 m	917 (52)	1009	943 (1,15)	967	936 vvw	912 (31)	954 w		991 (2,0.8)
	21	Skeletal-C inversion	828 vw		924	844 (8,12)	852	827 mw	830 (500)	932 mw	938 (66)	923 (0.1,1.4)
	22	C-H wag	771 ms	768 (5)	763	751 (87,3)	751	766 m		742 m		768 (55,0.1)
	23	Skeletal twist	726 ms	731 (12)	185	730 (3,2)	696	729 m		700 mw		715 (96,35)
	24	Skeletal twist		416 (78)	437	408 (8,17)	427		425 (234)	421 vw		435 (5,19)
	25	O-C-O wag (o.p.)		---	534	134 (3,66)	145					146 (23,12)
	26	O-C-O torsion		---	170	28 (0.02,60)	*i*					43 (3,4)

Table 11. Continued.

		Description	CaDPA			DPA^{-2}		Na_2DPA		CaDNic		
			IR[a]	Raman[b]	Carmona[c]	$\bar{\nu}_{CALC}$ C_s[d]	C_{2v}[d]	IR[a]	Raman[b]	IR[a,e]	Raman[b,e]	$\bar{\nu}_{CALC}$[d]
B_2	27	C-H stretch	3098 vw	3098 (149)	3078	3064 (41, 3382)	3078				(3083)	3042 (23,1604)
	28	C=O stretch	1613 m	1610 (110)	1609	1613 (1000,254)	1625	1615 vs		(1607 s)	1608 (192)	1612 (254,94)
	29	Ring stretch	1573 m	1574 (196)	1556	1569 (100,819)	1568	1577 vs	1589 (272)	1549 s		1566 (5,531)
	30	Ring stretch	1461 vs	1464 (91)	1466	1418 (19, 8)	1410	1453 m		1456 ms	(1463 (769))	1394 (15,7)
	31	Ring stretch	1377 vs	1371 (124)	1382	1320 (896,131)	1298				1245 (607)	1253 (26,40)
	32	C-H wag (in-plane)	1279 s	1279 (12)	1277	1235(5,32)	1240	1271 mw			1263 (41)	1269 (35,6)
	33	C-H wag	1183 m	1182 (19)	1200	1152 (15, 3)	1141	1177 w				1071 (42,11)
	34	C-O stretch	1146 m	1144 (73)	1150	1133 (0.3,48)	1122	1150 w	1159 (201)		1307 (25)	1311 (14,0.8)
	35	Skeletal stretch	864 w	860 (181)	822	862 (38,0.9)	847			837 m	851 (281)	877 (36,6)
	36	Skeletal bend (ring+ C=O)	707 m	708 (12)	742	703 (117,10)	706	702 mw			680 (26) br	700 (1.4,0.7)
	37	Ring-$C(O)_2$ wag(in-plane)		395 (56)	696	362 (12, 2)	543			566 w	568 (134)	534 (12,0.3)
	38	Skeletal bend		249 (14)	269	261 (7,0.6)	379		383 (121)			381 (9,12)
	39	O-C-O wag		230 (29)	424	142 (8,33)	263				250 (68)	247 (0.3,7)

[a] Abbreviations: s – strong , m – medium , w – weak , v – very, br – broad , sh – shoulder.
[b] Values in parentheses are relative intensities.
[c] Values from ref. [18].
[d] Scaled frequencies, values in parentheses are relative IR and Raman intensities, respectively.
[e] Frequencies in parentheses have been used more than once.

that we consider the DNic and CaDNic assignments to be reasonable, but they are also tentative.

For the identification of anthrax spores it is important to be able to distinguish DPA and DPA^{-2} from DNic, $DNic^{-2}$, and other similar molecules. Figures 23 and 24 compare the calculated DPA Raman and infrared spectra to those of DNic while Figures 25 and 26 compare the calculated spectra of the two anions DPA^{-2} and $DNic^{-2}$. Figure 26 compares the recorded Raman spectrum of DPA to that of DNic in the 600 to 1800 cm^{-1} region, which is the most promising for the detection of anthrax spores. As can be seen, although the DPA and DNic spectra have a number of similarities, there are also sufficient spectroscopic differences to allow discrimination between the two molecules. The same is true for the DPA^{-2} and $DNic^{-2}$ which can be distinguished from their spectra. It might be noted that Wasylina and co-workers[43] in 1999 published a brief listing of infrared frequencies for DPA, DNic, and three other pyridinecarboxylic acids. This is shown in Table 12. Although the data appear only to have a $\pm$ 10 cm^{-1} accuracy and are only for infrared spectra, what they show is that all of these are spectroscopically sufficiently different to allow for selective identification.

SPECTROSCOPIC EFFECTS OF MOLECULAR INTERACTIONS

As discussed above, the intermolecular hydrogen bonding between DPA molecules or with water can significantly affect the spectra of the DPA. In order to better understand that, we have carried out DFT computations on a DPA dimer where hydrogen bonding occurs through the carboxylic acid groups. Such interactions are well

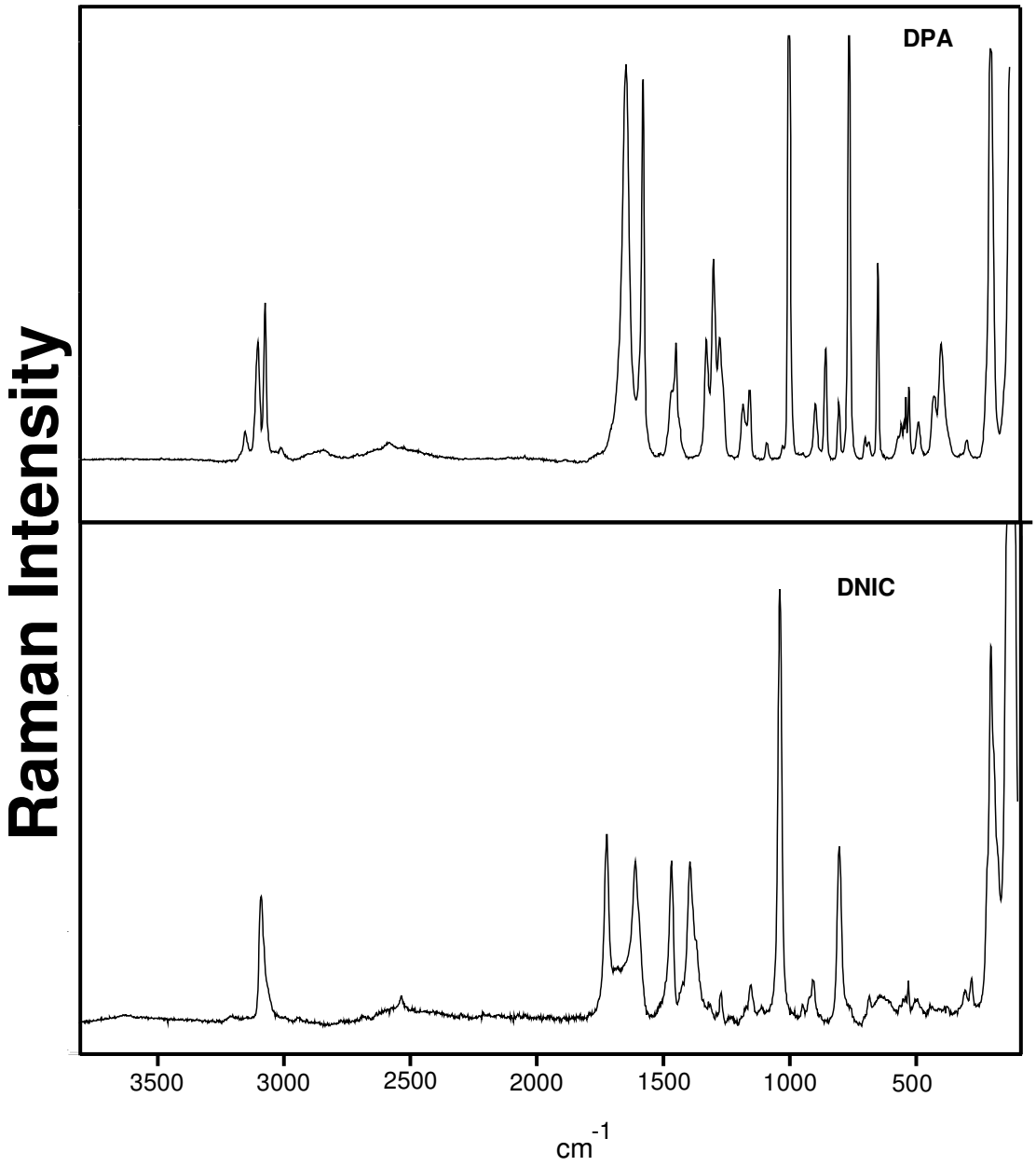

Figure 23. Comparison of the DPA and DNic experimental Raman spectra.

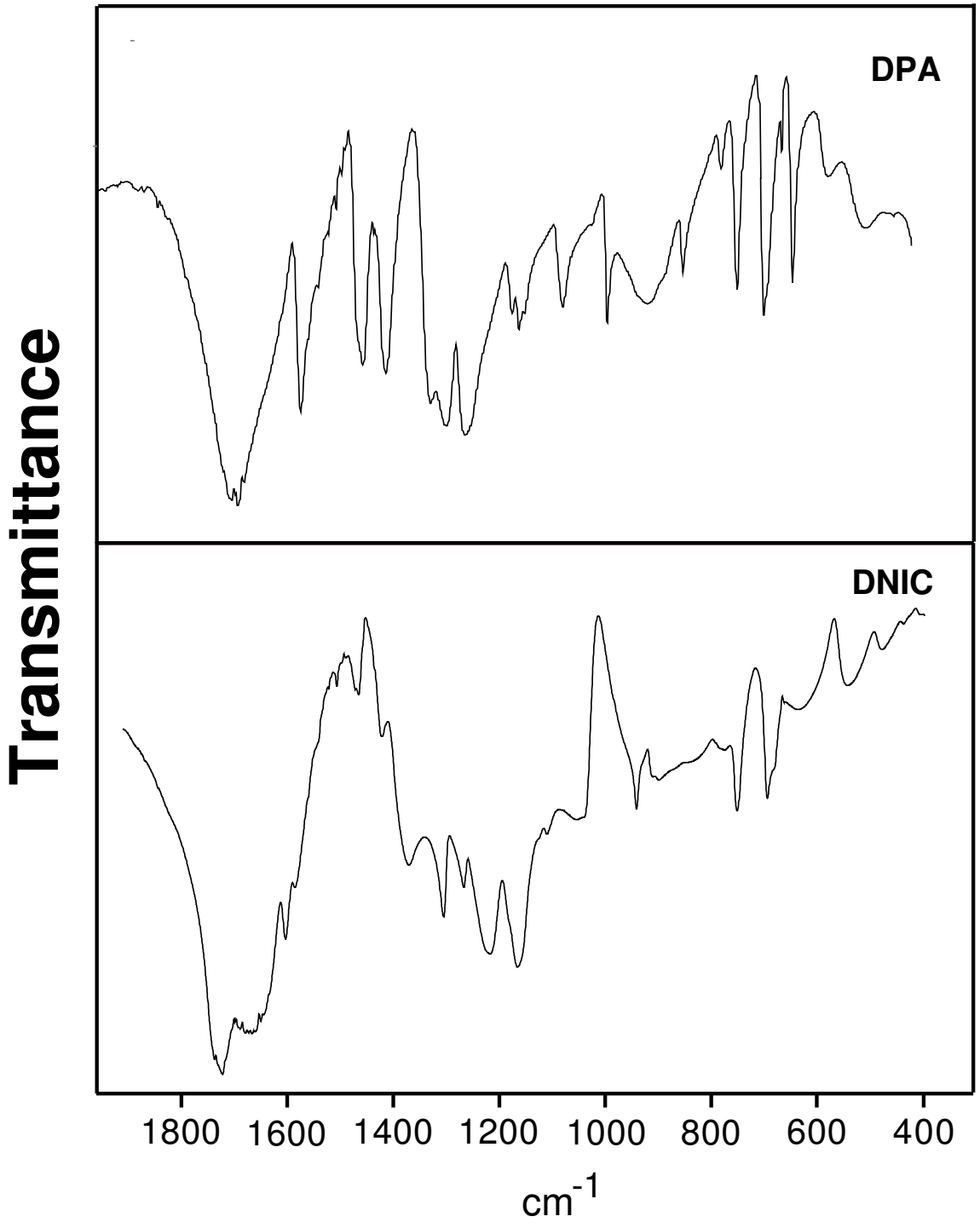

Figure 24. Comparison of the DPA and DNic experimental infrared spectra.

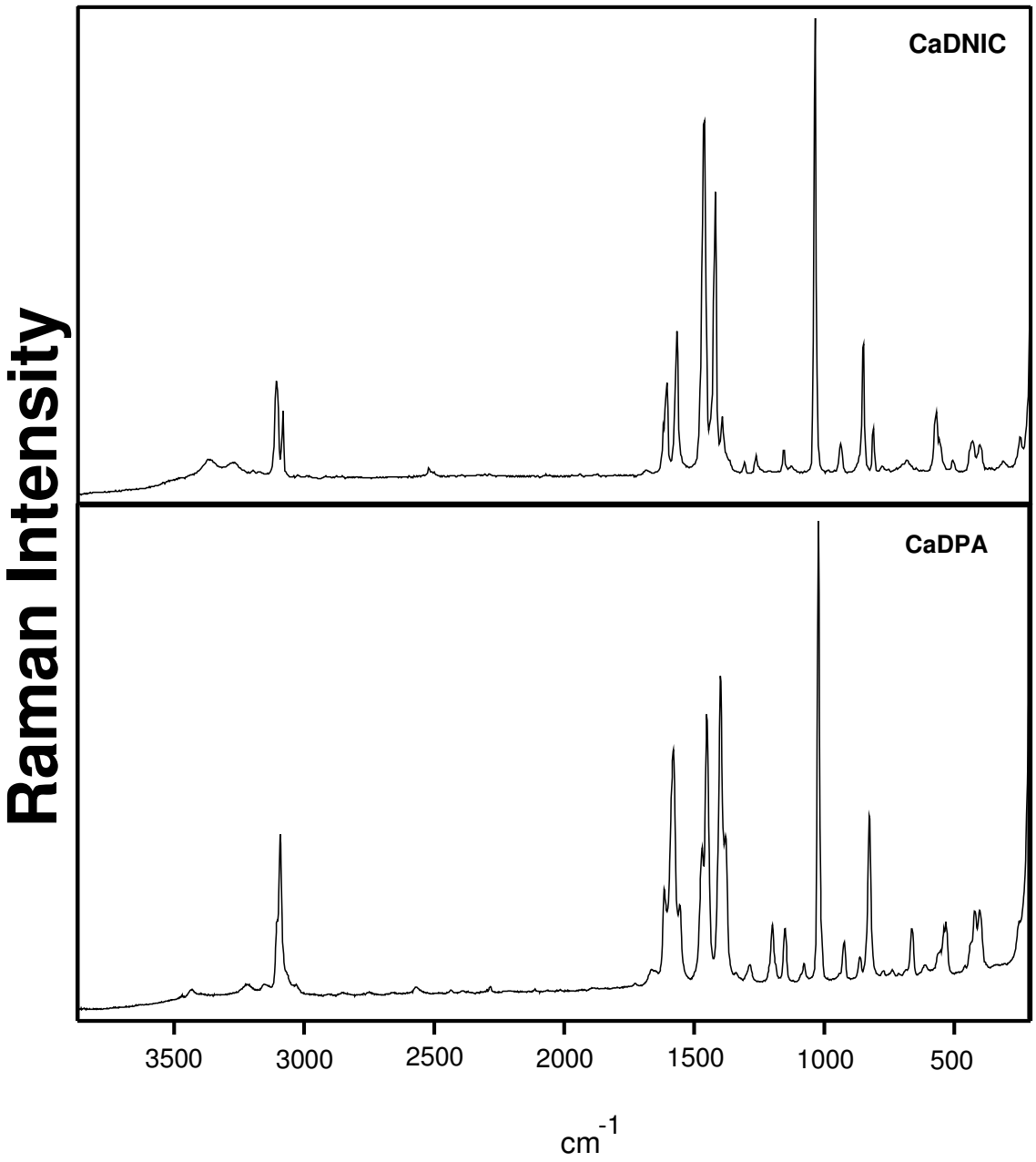

Figure 25. Comparison of the DPA^{-2} and $DNic^{-2}$ calcium salt Raman spectra.

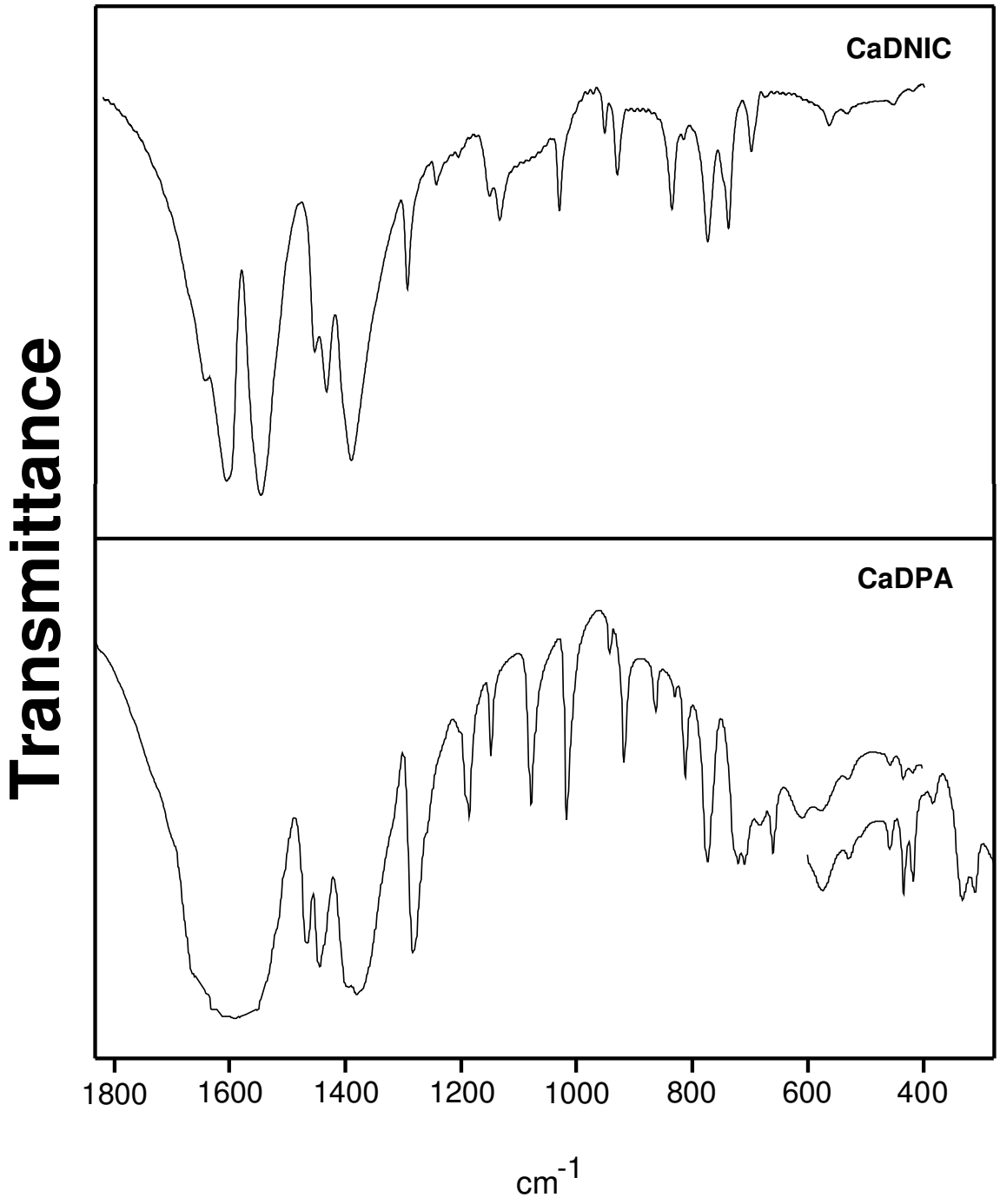

Figure 26. Comparison of the DPA^{-2} and $DNic^{-2}$ calcium salt infrared spectra.

Table 12. Reported infrared spectra (cm^{-1}) of pyridinedicarboxylic acids.

DPA (2,6) [a]	DNic (3,5) [a]	2,3 [a]	2,4 [a]	2,5 [a]	3,4 [a]
1710s	1730s		1730s	1730-1790s	1720s
1690s	1690m				
	1630m	1610s		1610s	1640s
	1590m	1580m	1590m		1600s
1470m		1480s	1500m	1470m	
1460m		1430m			
1420m		1420s	1390m	1420m	
1340m					1340-1370br
1300m		1310s	1310s	1130-1260br	
1270s	1270m	1280m	1270s		
	1220s	1240m			1250s
	1160s	1170s	1180m		
	1150m	1140s			
	1060m	1000-1060br	1080m		1040m
920-950br	950m		1000m	980m	990m
					940s
				810m	880m
760m	760s		760s	770s	760m
705s	690s	680m	700s	700s	725m
650m		660m	650m		660m
		620m			
		600s			

[a] Abbreviations: s – strong , m – medium , br – broad.

known. We have also carried out calculations for DPA + $2H_2O$ where each carboxylic acid group of the DPA is hydrogen bonded to a water molecule. The computations provide frequencies for all the vibrations, but we were particularly interested in the effects on the interacting carboxylic acid groups. Table 13 summarizes the frequency changes predicted by these interactions for several of the vibrational modes. As can be seen, both the calculations predict lowering of the C=O stretching mode as expected, but the dimer model does a much better job of predicting the effect of the interaction. A single DPA molecule would have a C=O stretching frequency at 1830 cm^{-1}, but anhydrous DPA in the crystal has it at 1645 cm^{-1}. Our DPA dimer model predicts it at 1668 cm^{-1}. The other vibrational frequencies in Table 13 can be seen to be little affected by the intermolecular interactions, except for the O-H stretching.

CONCLUSIONS

High level DFT calculations have been carried out on DPA, DPA^{-2}, DNic, and $DNic^{-2}$ to determine the structures and vibrational spectra of the independent molecules. The results for DPA and DPA^{-2}, however, differ from the crystal structures reported in the literature and the vibrational spectra which were recorded in the present study. This difference is caused by extensive intermolecular interaction involving hydrogen bonding between neighboring molecules or with the water in hydrated crystals. These interactions greatly affect the C-O bond distances of the carboxylic acid groups and also considerably reduce the frequencies of the C=O stretching vibrations. This effect could be simulated by calculations carried out on the DPA dimers and the DPA·$2H_2O$

Table 13. Calculated frequencies (cm^{-1}) of DPA in different environments.

			DPA	DPA · $2H_2O$	DPA_2
A_1	1	O-H stretch	3665	3274	3107
	2	C-H stretch (i.p.)	3108	3101	3101
	3	C-H stretch	3062	3069	3071
	4	C=O stretch	1830	1718	1668
	5	Ring stretch	1586	1594	1594
	6	Ring stretch(+Ring-C)	1435	1459	1456
	7	O-H in-plane wag	1334	1420	1325

complex. For the other vibrational frequencies there is less effect resulting from the intermolecular interactions.

Since DPA and DPA^{-2} are both present in anthrax spores, it is important to be able to distinguish these species from related molecules such as DNic and $DNic^{-2}$. For this reason the latter two molecules were also extensively studied by Raman and infrared spectra. Although there are spectroscopic similarities, there are also sufficient spectral differences to permit DPA to be distinguished from DNic and other related molecules. The same is true for the anions.

CHAPTER VI

RAMAN SIGNATURE OF THE NON-HYDROGEN-BONDED TRYPTOPHAN SIDE CHAIN IN PROTEINS: EXPERIMENTAL AND *AB INITIO* SPECTRA OF 3-METHYLINDOLE IN THE GAS PHASE*

INTRODUCTION

The effectiveness of Raman spectroscopy as a protein structural probe relies upon accurate vibrational assignments for the many spectral bands contributed by both the main chain and diverse side chains of the protein. Also required are definitive correlations linking key parameters of the Raman bands, such as spectral frequency (wavenumber), relative intensity and polarization, to the local environments of the protein moieties to which the bands are assigned. Because the main-chain peptide moiety is the most prevalent chemical group in every protein, its Raman markers (so-called amide bands) are typically the most prominent in the spectra. Accordingly, the Raman amide bands have been investigated extensively and are the best understood in terms of quantitative relationships between their spectral attributes and the local environment or conformation of the protein main chain. Pre-eminent among Raman amide bands is the carbonyl-related amide I mode, which generally occurs within the 1640-1700 cm^{-1} interval of the Raman spectrum[44-47].

---

*Reprinted with permission from "Raman signature of the non-hydrogen-bonded tryptophan side chain in proteins: experimental and *ab initio* spectra of 3-methylindole in the gas phase" by Amanda Combs, Kathleen McCann, Daniel Autrey, Jaan Laane, Stacy A. Overman, and George J. Thomas, Jr., 2005. Journal of Molecular Structure, 735-736, 271-278, Copyright 2005 by Elsevier.

Also prominent in Raman spectra of proteins are bands assigned to skeletal stretching modes of electron-rich groups, including vibrations associated with the aromatic rings of tyrosine (Tyr), tryptophan (Trp) and phenylalanine (Phe) side chains and vibrations of the sulfur-containing cysteine (Cys) side chain. Many structural correlations have been developed for Raman markers of these side chains and ongoing refinements continue to improve the usefulness of the Raman markers for diagnosis of side chain orientation, interaction or covalency[48-54]. Reviews and critical discussions have been given recently[46,55-57].

A previous collaboration between the Laane and Thomas laboratories[53] reported a combined infrared, Raman and *ab initio* analysis of the tyrosyl model compound *p*-cresol in the vapor phase. The objectives of that study were to refine earlier vibrational assignments for the *para*-substituted phenolic ring of Tyr [49,58] and more specifically to identify Raman markers diagnostic of the non-hydrogen-bonded state of the tyrosine phenoxyl group. The latter objective is particularly important for protein applications of Raman spectroscopy because of the well established sensitivity of Raman markers of the tyrosine side chain to the various donor and acceptor roles of the phenoxyl group[49]. The analysis by Arp et al.[53] identified the key Raman markers of tyrosine that were diagnostic of the non-hydrogen-bonded state of the phenolic OH group and demonstrated further that the non-hydrogen-bonded state could account for the unique tyrosyl signatures observed in Raman spectra of capsid protein subunits of filamentous viruses[59,60].

This chapter describes the results of a further collaboration with the Thomas laboratories. Here the tryptophan model compound 3-methylindole (3MI) in the vapor phase. 3MI serves as a convenient structural analog of the indolyl side chain of tryptophan (Figure 27). Raman spectra of 3MI and selected isotopic derivatives we investigated previously to reach reliable assignments for the indolyl moiety, as well as to identify the Raman spectral signature of the tryptophan residue in proteins, and to characterize the dependence of this signature on the local orientation and interactions of the indolyl ring[50,54,61-64]. The previous studies of the Harada and Takeuchi groups have provided a solid foundation upon which to develop more comprehensive vibrational assignments. Importantly, they facilitate probing the spectral consequences of eliminating (via the gas phase) both the indolyl N1–H donor group and the π-electron acceptor system from participation in significant intermolecular interaction, including hydrogen bonding. The biological significance of the non-hydrogen-bonded state of the tryptophan side chain derives from the frequent occurrence of this residue in the protein subunits of filamentous virus capsids, hydrophobic cores of globular proteins and hydrophobic transmembrane domains of membrane proteins[65]. It is also noteworthy that the π-electron system of the indolyl ring has been implicated as a robust hydrogen-bond acceptor in native proteins[66].

The present results confirm and extend earlier vibrational assignments for the indolyl moiety and demonstrate a remarkable sensitivity of many vibrational bands of the tryptophanyl side chain to intermolecular interaction.

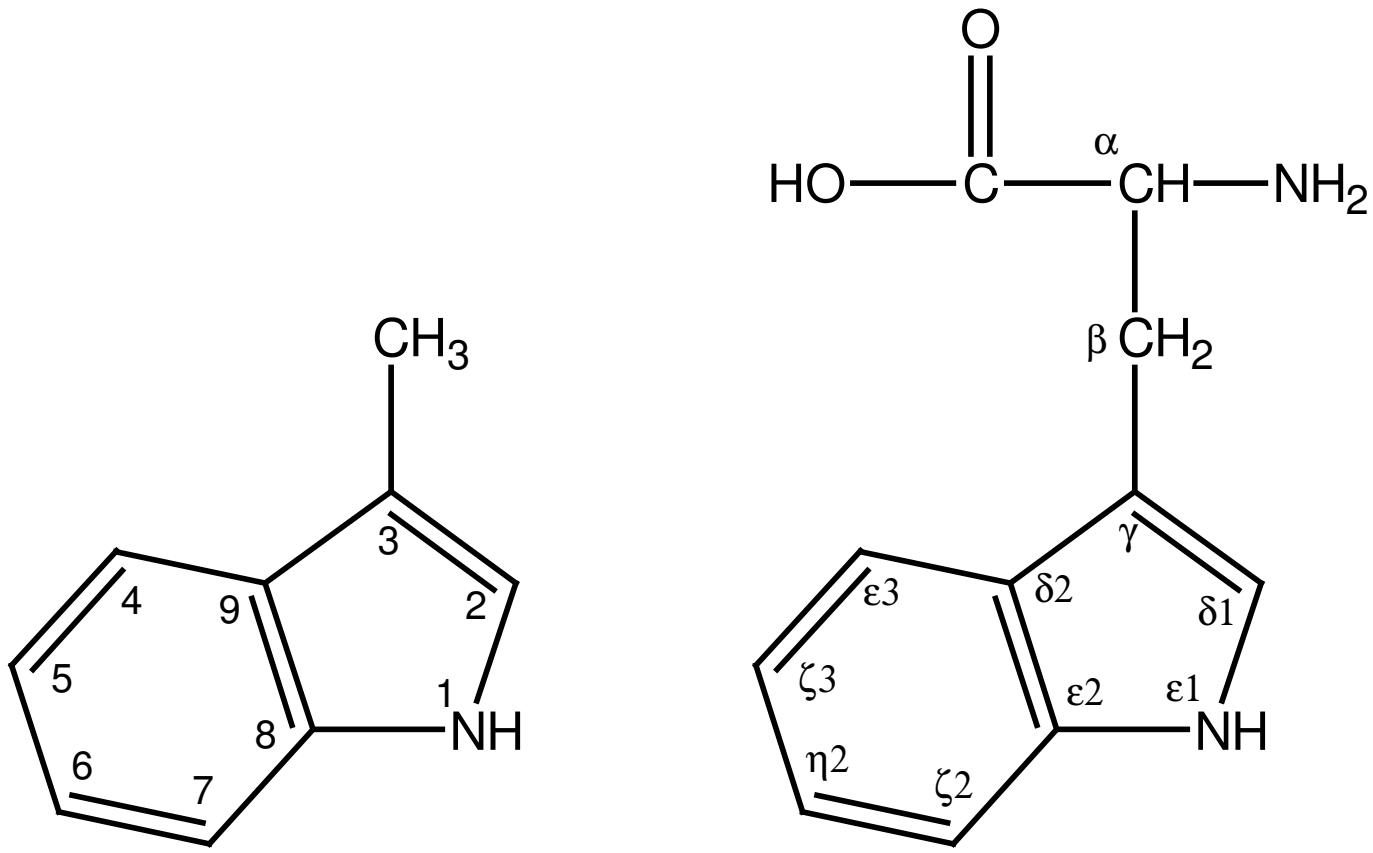

3-methylindole tryptophan

Figure 27. Structures of 3-methylindole (left) and tryptophan (right). The numbering of ring and exocyclic atoms follows IUPAC-IUPAB nomenclature[72].

MATERIALS AND METHODS

3-Methylindole (98%), m.p. 96°, b.p. 266°, was purchased from Aldrich Chemical (St. Louis, MO) and purified by trap to trap vacuum distillation. Raman spectra were collected on a Jobin Yvon U-1000 spectrometer (Instruments S. A., Edison, NJ) using excitation at 514.5 nm from an Innova 20 argon-ion laser (Coherent, Santa Clara, CA). The laser power at the sample cell was 2 W for vapor and 800 mW for liquid samples. Vapor phase spectra of approximately 1 atm of sample were obtained at 300 ± 5 °C using a custom-designed thermostatically controlled Raman cell[1] into which solid sample was transferred; the Raman cell was subsequently frozen with liquid nitrogen and sealed after evacuation on a vacuum line. Liquid phase spectra were obtained in a glass tube heated with nichrome wire to 100 °C. Solution spectra at 23± 3 °C in various solvents were recorded using quartz cuvettes to contain the samples. Either a charge-coupled device or a photomultiplier tube was used for detection of the Raman scattered light. The Raman spectra were collected and processed using standard software packages (SpectraMax and Bomem Grams).

Infrared spectra were recorded on either a Bomem DA8.02 or a BioRad FTS-60 instrument. Vapor phase spectra at 300 ± 10 °C were recorded using a heatable 10 cm metal cell with KBr windows. Spectra of solid samples (as Nujol mulls) between KBr plates were recorded at 25 °C.

Ab initio calculations were carried out using the GAUSSIAN 03[13] package at the density functional (B3LYP) level of theory. Structural parameters and vibrational frequencies with infrared and Raman intensities were obtained with the 6-311++G**

basis set. Scaling factors of 0.955 for the 2800 – 3500 cm^{-1} region and 0.985 for the region below 1700 cm^{-1} were used for both our calculations and those of Bunte et al.[67,68].

RESULTS

Experimental and Theoretical Vibrational Spectra of 3-Methylindole

Table 14 lists the full Raman (liquid and vapor) and infrared (solid and vapor) spectra of 3-methylindole (3MI) including both unscaled and scaled vibrational frequencies and their approximate vibrational descriptions calculated using the B3LYP/6-311++G** basis set. Figure 28 compares the experimental Raman spectra of the neat liquid (trace A) and vapor (trace B) with the calculated spectrum (trace C). As in a previous study of *p*-cresol[53], the agreement between observed and calculated values is excellent. The data of Table 1 are also in satisfactory agreement with corresponding data reported by Bunte et al.[67], although some refinements were necessary in the previous assignments and vibrational descriptions, particularly for low frequency modes. All of the vibrations have been classified in accordance with $\boldsymbol{C_S}$ symmetry, so that in-plane and out-of plane vibrations are of species $\boldsymbol{A'}$ and $\boldsymbol{A''}$, respectively. Because the hydrogen atom at the N^1 indolyl ring site (corresponding to $N^{\varepsilon 1}$ of tryptophan) does not lie precisely in the ring plane, the indole moiety lacks rigorous $\boldsymbol{C_S}$ symmetry. However, this non-planarity has such a small effect that the spectral characteristics are for the most part those of a planar skeleton with $\boldsymbol{C_S}$ symmetry. This is also evident in the work of Bunte et al.[67], i.e. vibrations classified here as $\boldsymbol{A''}$ are reported by Bunte et al. as depolarized (depolarization ratio $\rho = 0.75$). The vibrations have also been renumbered using the usual convention of high frequencies listed first.

Table 14. Experimental and calculated vibrational frequencies of 3-methylindole.

				Raman		Infrared		Bunte	ab initio		Bunte ab initio		p	
		approximate description		Liquid	Vapor	Solid	Vapor	exp.	Unscaled[a]	Scaled	Unscaled	Scaled	p	p(Bunte)
A'	1	N-H stretch		3425 m	3506 m	3507/3402 w	3515/3421 vs	3493	3678 [532,74]	3512	3682	3516	0.21	0.20
	2	=C-H stretch		3119 mw	3118 w	3190 vw	3090 sh w	3084	3240 [472,1]	3094	3243	3097	0.31	0.31
	3	C-H stretch (Bz)		3058 s	3065 vs	---	3061 vs	3060	3189 [1156,18]	3045	3192	3048	0.12	0.13
	4	C-H stretch (Bz)		---	3053 sh m	3053 w	3034 vvw	3039	3178 [208,30]	3035	3181	3038	0.75	0.75
	5	C-H stretch (Bz)		---	---	---	---	3017	3167 [540,3]	3025	3171	3028	0.63	0.60
	6	C-H stretch (Bz)		---	---	3033 vw	3015 vvw	2972	3161 [116,1]	3019	3165	3023	0.70	0.72
	7	CH_3 antisym. stretch		2921 ms	2934 s	2931 m	2931 ms	2923	3091 [944,22]	2952	3097	2958	0.66	0.66
	8	CH_3 sym. stretch		2861 m	2873 m	2858 ms	2870 m	2860	3013 [944,50]	2877	3021	2885	0.05	0.03
	9	Skeletal stretch (Bz-8b + Pyr)		1618 mw	1620 w	1619 m	1619 w	1617	1660 [68,4]	1635	1658	1633	0.74	0.74
	10	Skeletal stretch (Bz-8a + Pyr)	[W2]	1579 ms	1585 sh vw	1589 mw	---	1577	1617 [96,0]	1593	1616	1592	0.07	0.05
	11	Skeletal stretch (Bz + Pyr)		1559 s	1561 vs	1555 w	1559 w	1557	1595 [320,3]	1571	1594	1570	0.26	0.26
	12	Skeletal stretch (Bz-19a + Pyr)		1512 vw	---	1486 w	1488 w	1493	1522 [10,1.5]	1499	1526	1503	0.68	0.64
	13	CH_3 antisym. deformation		1489 w	---	--- mw	1472 mw	1488	1499 [48,9]	1477	1504	1481	0.67	0.66
	14	Skeletal stretch (Bz-19b)/ CH wag		1457 m	1454 mw	1455 s	1456 vs	1455	1480 [56,26]	1458	1485	1463	0.73	0.71
	15	N-H wag	[W6]	1418 ms	1409 ms	1422 w	1418 m	1420	1446 [216,14]	1424	1446	1424	0.53	0.53
	16	CH_3 deformation		1384 w	1388/1377 vvw	---	1383	1387	1420 [32,1.5]	1399	1424	1403	0.57	0.68
	17	Skeletal stretch (Bz-3)	[W7]	1352/1345 vs	1349/1341 vs	1344 vw	---	1345	1373 [240,16]	1352	1372	1351	0.14	0.17
	18	Skeletal str (Bz-14+Pyr)/CH/NH wag(Bz+Pyr)		1334 vvw	1324 sh vw	1334 vw	1333 s	1334	1365 [44,17]	1345	1366	1346	0.46	0.46
	19	Skeletal str (Bz+Pyr)/CH wag(Bz+Pyr)		1299 mw	1292 w	1299 mw	1297 w	1302	1319 [44,10]	1300	1322	1302	0.46	0.34
	20	CH NH wag(Bz+Pyr)/Ring Bend(Pyr)		1247 m	1245 ms	1247 vw	1247 m	1249	1270 [52,11]	1251	1274	1255	0.25	0.16
	21	Ring stretch(Pyr)		1227 m	1223 m	1228 w	1225 ms	1229	1242 [64,11]	1224	1245	1226	0.13	0.15
	22	C-H wag(Bz-15)		1153 w	1142 w	1149 w	1150 vw	1149	1176 [4,1]	1159	1180	1162	0.52	0.70
	23	C-H wag(Bz-9b)		1126 w	1142 w	1128 mw	1126 vw	1126	1148 [12,1]	1131	1150	1133	0.62	0.74
	24	=CH NH wag		1085 m	1089 sh vw	1086 ms	1096 sh w	1080	1106 [12,26]	1089	1107	1090	0.06	0.13
	25	Skeletal deformation/=CH/NH wag		1075 m	1078 m	1069 m	1080 s	1070	1090 [40,17]	1074	1091	1075	0.11	0.13
	26	Ring breathing(Bz-18b)		1010 vs	1012 vs	1008 m	1010 m	1009	1033 [100,11]	1018	1034	1018	0.05	0.04
	27	CH_3 rock		980 m	981 m	971 s	980 vvw	---	999 [48,6]	984	1001	986	0.07	0.08
	28	Skeletal deformation(Bz-12)	[W17]	875 m	881 ms	898 mw	---	876	888 [36,1]	875	891	878	0.08	0.09
	29	C-C stretch(Bz)		757 vs	755 vvs	756 m	---	758	773 [100,3]	761	774	762	0.05	0.04
	30	Ring bend(Bz)		707 m	707 mw	---	---	708	718 [28,0.1]	707	719	708	0.21	0.16
	31	Skeletal bending		559 m	559 mw	580 ms	---	565	570 [32,2]	561	571	562	0.72	0.72
	32	Ring bend(Bz)		530 m	530 ms	529 w	---	532	539 [24,2]	530	539	531	0.18	0.15
	33	Skeletal bending		460 w	463 vvw	497 s	---	462	470 [2.4,3]	463	471	464	0.58	0.72
	34	CH_3 wag		226 m	228 m	---	---	231	225 [8,0.6]	221	224	221	0.63	0.69
A"	35	CH_3 antisym. stretch		[2921] ms	[2934] s	[2931] m	[2931] ms	2889	3055 [360,22]	2918	3062	2924	0.75	0.75
	36	CH_3 antisym. deformation		1457 m	1454 mw	1455 s	1456 vs	1455	1483 [42,7.6]	1461	1486	1464	0.75	0.75
	37	CH_3 rock		1065/1026 sh vw	1048 vw	1039 w	---	---	1063 [0.12,0.1]	1047	1067	1051	0.75	0.74
	38	CH wag (Bz-5)		960 sh vw	963 sh vw	927 m	---	983	971 [0.8,0]	956	980	965	0.75	0.75
	39	CH wag (Bz)		924 vw	---	900 w	921 w	925	934 [1.2,1.4]	855	942	928	0.75	0.75
	40	CH wag (Bz)		844 w	842 vw	873/845 w	---	---	851 [1.6,0.3]	838	855	842	0.75	0.75
	41	=CH wag		799 w	789/807 vvw	804 m	782 w	780	792 [12,16]	780	796	784	0.75	0.75
	42	Ring twist(Bz)		[757] vs	[755] vvs	[756] vs	---	758	772 [0.4,1.2]	760	772	760	0.75	0.68
	43	CH wag (Bz-11)		736 w	755 vvs	738 vs	736 w	731	747 [1.6,88]	736	748	737	0.75	0.75
	44	Ring pucker(Pyr)		607 vw	---	605 vw	605 mw	601	616 [0.4,0.7]	607	618	609	0.75	0.75
	45	Ring twist(Bz-16a)		576 vvw	577 sh vw	564 vw	576 w	573	585 [0.4,6]	576	590	581	0.75	0.75
	46	Benzene oop wag(16a)		426 w	418 vvw	416 s	---	426	430 [1.6,4]	423	430	424	0.75	0.75
	47	N-H wag		377 vvw	---	---	---	347	372 [0.8,74]	366	351	346	0.75	0.75
	48	Skeletal twist		313 vw	304 vvw	---	---	231	284 [2.4,12]	279	248	244	0.75	0.75
	49	Skeletal flap		[226] m	---	---	---	---	223 [0.2,8]	220	222	219	0.75	0.71
	50	CH_3 wag		---	151 m	---	---	177	152 [8,5]	150	153	151	0.75	0.75
	51	CH_3 torsion		---	---	---	---	177	145 [0.8,0.1]	142	137	135	0.75	0.75

Bz - benzene ring vibration; Pyr - pyrrole ring vibration; oop - out of plane; values in brackets also assigned elsewhere; s-strong m-medium w-weak v-very

a) Relative Raman and IR intensities, respectively

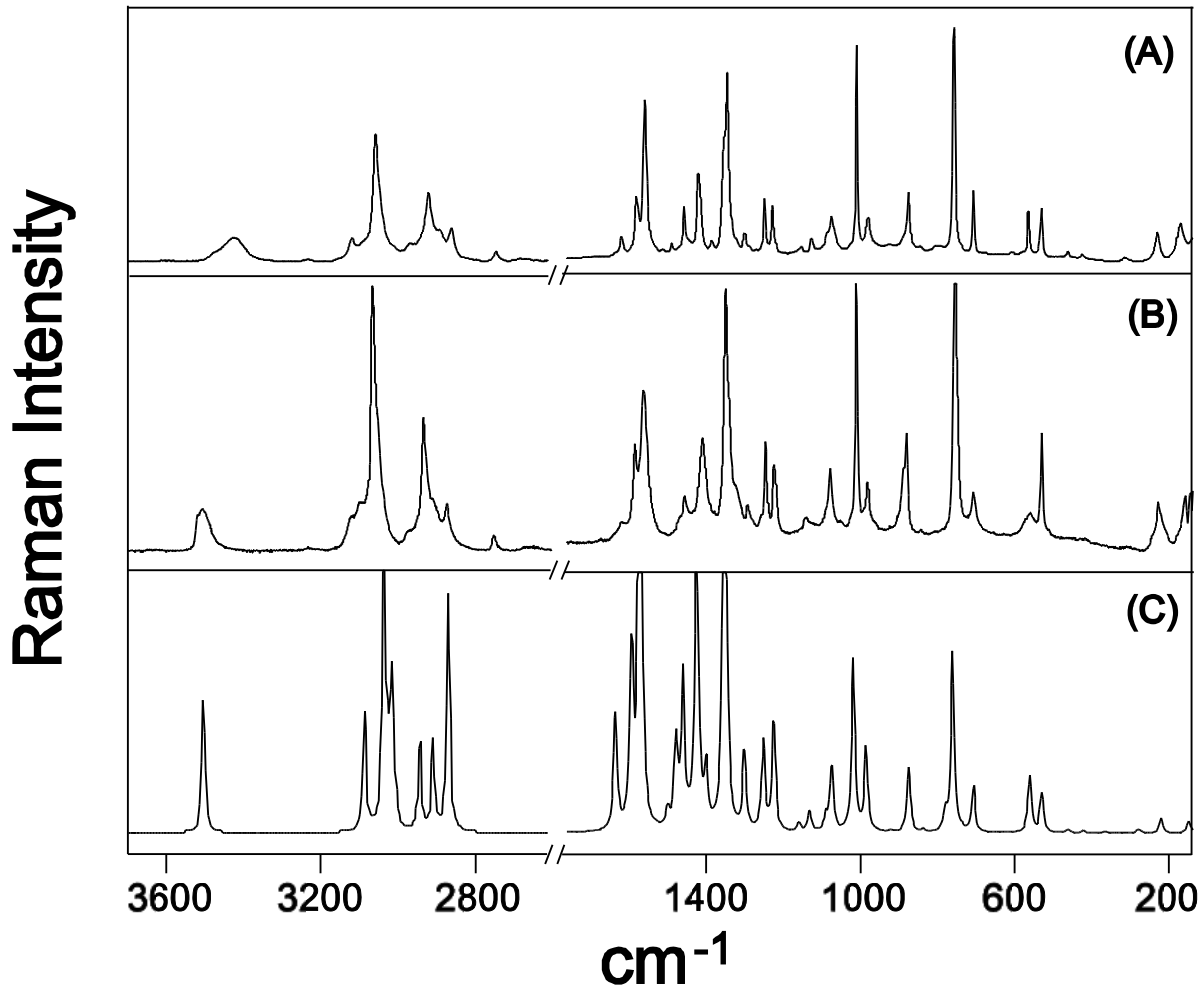

Figure 28. Raman spectra of 3-methylindole in the region 200-3600 cm^{-1}. (A) Neat liquid (melt at 100 °C). (B) Vapor at 300 °C. (C) Calculated (*ab initio*) using B3LYP/6-311++G**.

Ab Initio *Molecular Structure of 3-Methylindole*

The calculated structure of 3MI (6-311++G** basis set) is shown in Figure 29. The molecular skeleton lies totally within one plane and only the imidazolyl and methyl hydrogens lie outside this plane. The structure shows the expected delocalization of π electrons of the imidazole and phenyl ring systems, which results in a compression of the C^3–C^9 bond of Figure 27. Other bond lengths and angles are also as expected.

Raman Bands Diagnostic of the Isolated (Non-interacting) 3-Methylindole Molecule

Evidence for the absence of N^1–H hydrogen bonding by the 3MI molecule in the vapor phase comes from the very high frequency (3506 cm^{-1}) of the Raman band representing the NH stretching mode. The gas-phase 3MI molecule is also presumed to lack other types of intermolecular interactions. Accordingly, the spectrum of trace B in Figure 3 is considered to represent that of an isolated, non-interacting indolyl moiety.

Comparison of the Raman frequencies and intensities for neat liquid and vapor states of 3MI (Table 14) reveals numerous bands that are strongly sensitive to indolyl intermolecular interactions. For example, ~20 bands exhibit wavenumber shifts of at least 5 cm^{-1}. Of these, four bands are sufficiently intense to be of potential diagnostic value in protein Raman spectra. These are designated as the modes *W2* [1579 (*l*) and 1585 (*v*) cm^{-1}, for liquid and vapor, respectively)], *W6* [1418 (*l*) and 1409 (*v*) cm^{-1}], *W7* Fermi pair [1352/1345 (*l*) and 1349/1341 (*v*) cm^{-1}] and *W17* [875 (*l*) and 881 (*v*) cm^{-1}], in accordance with nomenclature employed previously for protein aromatic ring vibrations[46,69]. In addition, the Fermi doublet intensity ratio (I_1/I_2, where I_1 and I_2 are,

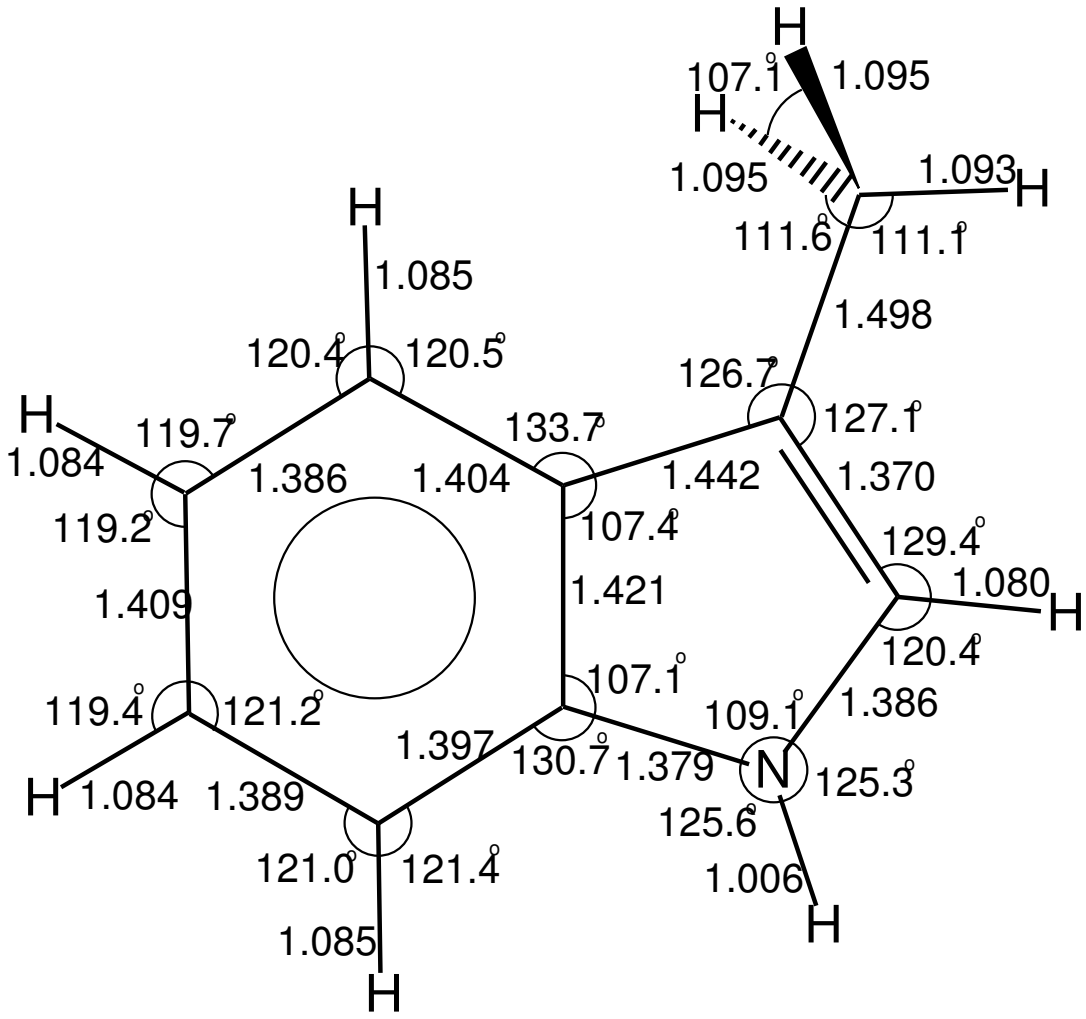

Figure 29. Calculated molecular structure of 3-methylindole using B3LYP/6-311++G**.

respectively, the Raman intensities of the higher and lower wavenumber components of the doublet) is highly sensitive to the state of condensation the 3MI molecule, consistent with the previously reported sensitivity of I_1/I_2 to solvent polarity. The observed ratios are $I_1/I_2 = 0.58$ for the liquid and $I_1/I_2 = 3.0$ for the vapor, after deconvolution of the overlapping members of the Fermi pair (Figure 30).

Effects of Indolyl Intermolecular Interactions on Key Raman Markers

The parameter I_1/I_2 of the *W7* band was also measured for solutions of 3MI in solvents of differing polarity and hydrogen-bonding capability. These measurements complement those of Harada and coworkers[50,54,61-64], who reported effects of solvent polarity on I_1/I_2 and developed several additional structural correlations applicable to spectral parameters of *W2*, *W6*, *W7* and *W17*. The combined results of this work and previously published data on I_1/I_2 of the *W7* band are summarized in Table 15. This table also lists the values of the dielectric constants ϵ_r for the different solvents. Solvents with higher ϵ_r values are expected to facilitate the intermolecular interactions

Harada and coworkers proposed that I_1/I_2 is diagnostic of the hydrophobicity of the indolyl ring environment. Specifically, I_1/I_2 increases with increasing hydrophobicity and has been referred to as a "hydrophobic interaction marker"[54]. This is evident from inspection of Table 15. In addition to *W7*, the sensitivity of the frequencies of the NH stretching and *W17* modes to indolyl NH hydrogen bonding have been noted[63] and confirmed by the present experiments (Figure 28 and related data not shown). These marker bands are further discussed in the following section.

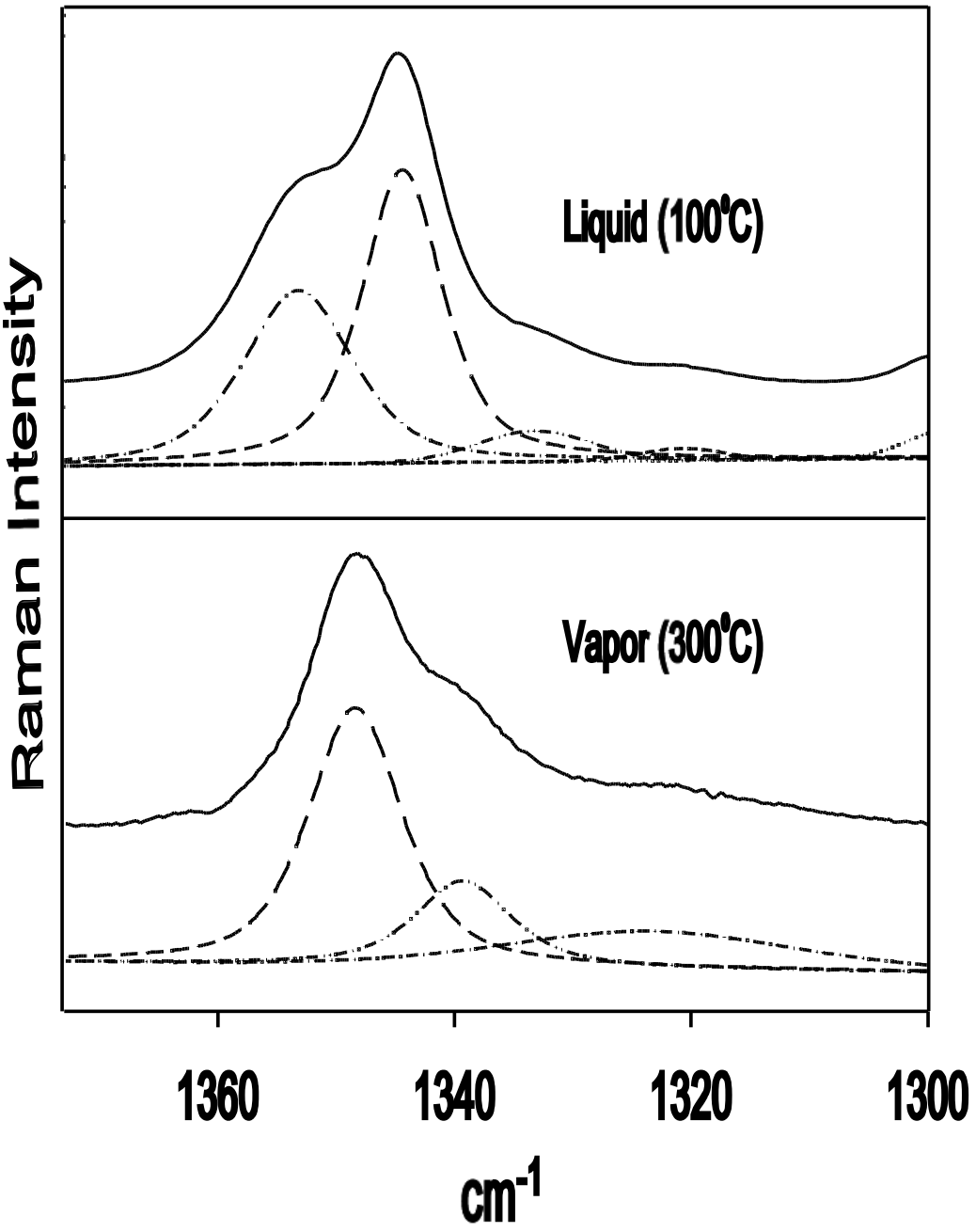

Figure 30. Raman spectra of 3-methylindole in the region 1300-1375 cm^{-1} showing the Fermi doublet (mode *W7*). Experimental data (solid line) and curve fits of the deconvolved data for the neat liquid at 100 °C and vapor at 300 °C are shown in the top and bottom panels, respectively. Data are from Figures 28A and 28B.

Table 15. Raman solution spectra frequencies of the *W7* band.

Phase	*Concentration (mM)*	*Raman Frequency* (cm^{-1})		*Ratio*[a] (I_1 / I_2)	*Dielectric Constant* [b]	*Reference*
Vapor	---	1349	1341	3.0	---	[c]
Solvent						
Cyclohexane	100	1352	1343	1.55	2.02	[c]
n-Hexane	100-200	1352	1343	1.50	1.89	[62]
Carbon disulfide	100-200	1350	1341	1.18	2.24	[62]
Methanol-d	500	1353	1346	1.18	---	[c]
Methanol-d	100	1354	1346	1.06	---	[c]
Toluene	100-200	1341	1343	1.04	2.38	[62]
Carbon tetrachloride	100	1353	1344	0.99	2.24	[c]
Benzene	100-200	1351	1343	0.96	2.28	[62]
Benzene	100	1353	1344	0.89	2.28	[c]
Benzene	500	1353	1344	0.83	2.28	[c]
o-Dichlorobenzene	100-200	1351	1343	0.83	10.12	[62]
Tetrahydrofuran	100	1354	1346	0.71	7.52	[c]
Methanol	100	1353	1346	0.48	33.0	[c]
Methanol	300	1355	1346	0.45	33.0	[c]
Chloroform	100	1354	1345	0.43	4.81	[c]
Neat Liquid(melt)	---	1352	1345	0.58	---	[c]

a) (I_1 / I_2) is the intensity ratio of the higher frequency band to the lower frequency band.
b) CRC Handbook of Chemistry and Physics, 85th Edition, p. **8**-141.
c) Data from this work.

DISCUSSION AND CONCLUSIONS

Miura and coworkers demonstrated that the *W17* mode of 3MI exhibits an apparent frequency dependence upon the strength of indolyl N–H···O hydrogen bonding[63]. This finding is based upon a close linear correspondence between *W17* and the frequency of the indolyl NH stretching mode when the hydrogen bonding environment of 3MI is varied. Raman and infrared spectral data collected from solutions of 3MI in solvents of diverse O-acceptor capabilities and from crystals of indolyl model compounds of known X-ray structure provide the experimental support[63]. The proposed structural correlation has been exploited recently to characterize tryptophan hydrogen bonding interactions in native proteins[50,70,71]. A keystone of the structural correlation is the observation that in a non-hydrogen-bonding solvent, such as CS_2 ($\epsilon_r = 2.24$) or cyclohexane ($\epsilon_r = 2.02$), the NH stretching and *W17* modes occur near 3476 (infrared) and 883 (Raman) cm^{-1}, respectively[63]. However, Raman frequencies of 3MI in the prototypical non-hydrogen-bonded state – viz. the vapor– were not reported previously.

In the present work it was determined that the NH stretching and *W17* modes of 3MI vapor occur at 3506 and 881 cm^{-1}, respectively, which constitute a data point only slightly deviant from the previously proposed linear relationship of Miura et al. (Figure 2 of reference[63]). Accordingly, the results are consistent with the proposition that the wavenumber value of the *W17* mode is a reliable indicator of indolyl N^1–H hydrogen bond donation. Specifically, it can be concluded that the non-hydrogen-bonded N–H group exhibits *W17* at 882 ± 1 cm^{-1}, while the very strongly hydrogen bonded N–H group exhibits *W17* at 871 ± 1 cm^{-1}. The former state is represented by the vapor (this

work) and both CS_2 and cyclohexane solutions of 3MI[63], while the latter is represented by the N–H···O bond in the crystal structure of N-acetyl-DL-tryptophan methylamide[63].

With respect to the relative Raman intensity ratio (I_1/I_2) of the components of the Fermi doublet (*W7*), the situation appears to be more complex (Table 15). The underlying hypothesis is again that the 3MI molecule in the vapor is devoid of any intermolecular interactions. Accordingly, in the absence of intermolecular contacts with either hydrophobic or polar molecules, including potential hydrogen bonding partners for the exocyclic (N^1–H) or aromatic (π-electron) groups of 3MI, I_1/I_2 achieves its maximum value of 3.0. This value falls sharply with the introduction of *any* intermolecular environment represented by the solvents of Table 2. For non-polar and non-hydrogen-bonding solvent environments the range observed is $0.8 < I_1/I_2 < 1.6$, which is twofold to threefold lower than the maximum observed for the vapor. In the case of polar and hydrogen bonding solvent environments, I_1/I_2 is further diminished by another factor of two, i.e. $0.4 < I_1/I_2 < 0.8$. Therefore, the I_1/I_2 ratio is strongly sensitive to factors other than simply NH or π hydrogen bonding, namely to the intermolecular environment of the indolyl ring and the relative hydrophobicity/hydrophilicity of that environment.

The results of this work show that the strength of Fermi coupling of *W7* is relatively weak for the noninteracting indolyl ring (vapor phase). This results in a relatively large intensity imbalance ($I_1/I_2 \sim 3.0$) between the two components of the Fermi doublet. Upon introducing interactions with hydrophobic molecular neighbors (apolar solvents), the Fermi coupling is strengthened and the doublet components

approach parity of intensity (I_1/I_2 ~ 1). Further, as the hydrophobicity of the local indolyl ring environment is diminished in favor of hydrophilicity (polar solvents), the strength of Fermi coupling again weakens and the parity of intensity of the doublet components is diminished (I_1/I_2 ~ 0.4).

Takeuchi and co-workers[54] have attributed the Fermi coupling to resonance between the *W7* in-plane fundamental vibration (mainly N^1=C^8 bond stretching) and one or more combination bands due to out-of-plane vibrations. These authors speculate that small changes in the hydrophobic character of the solvent could affect the frequencies of the out-of-plane components and impact the strength of Fermi coupling. While this may explain the solution results, it does not explain the persistence of Fermi coupling in the vapor phase spectrum of 3MI. The present results show that even in the absence of solvent interactions at the faces of the indolyl plane, Fermi coupling is sufficient to generate a recognizable doublet in the Raman spectrum.

The complexity of Fermi coupling in the 1330-1370 cm^{-1} region of the indole Raman signature is further complicated by recent data obtained on bacteriorhodopsin[71,72]. A tryptophan residue of this protein generates an apparent *W7* triplet (1370/1357/1339 cm^{-1}) in lieu of the doublet normally encountered in protein Raman and UVRR spectra. These results suggest the need for additional studies to elucidate the origins of *W7* Fermi coupling and factors affecting the intensities of the multiplet components.

CHAPTER VII

CONCLUSIONS

1,3-Benzodioxan has been investigated in both its ground, S_0, and excited, $S_1(\pi,\pi^*)$, electronic states. A detailed energy map of the vibrational levels involving the six lowest frequency vibrations was established and utilized to better understand the structural and conformational differences between the ground and excited electronic states. The energies of more than a dozen vibrational excited states involving the out-of-plane ring twisting (ν_{47}) and the out-of-plane ring bending (ν_{48}) modes were determined for both S_0 and S_1 electronic states. The data allowed for the calculation of one-dimensional potential energy functions. These show the molecule to have a twisting angle of 33° and a barrier to planarity of 4300 ± 500 cm^{-1} for the S_0 ground state and an angle of 24° and a barrier of 1500 ± 200 cm^{-1} for the $S_1(\pi,\pi^*)$ excited state..

In addition to the work completed on the low-frequency vibrations and conformation energetics, a complete vibrational assignment of 13BZN in its S_0 ground state and the assignment for a dozen vibrational modes in the $S_1(\pi,\pi^*)$ excited state has been completed. The vibrations of the very similar 1,4-benzodioxan have been included with the vibrations of 13BZN for comparison.

Ab initio and DFT calculations have allowed refinement of a previous vibrational assignment of DPA and CaDPA. Because of extensive intermolecular hydrogen bonding in the crystals of the molecules, the calculated structures and spectra for the individual molecules agree only moderately well with the experimental values. The

spectra do show that DPA and its calcium salt, which are present in anthrax spores, can be distinguished from the very similar DNic and CaDNic.

For the tryptophan side-chain structural model of 3-methylindole, the vapor phase molecule exhibits Raman bands at 3506, 1585, 1409, 1349/1341 (Fermi doublet) and 881 cm^{-1}, which differ greatly from their counterparts in the Raman spectrum of 3MI liquid and thus serve as spectral markers of the indolyl ring environment. The Fermi doublet relative intensity ration (I_1/I_2, where I_1 and I_2 are, respectively, the Raman intensities of the higher and lower wavenumber components of the doublet) is highly sensitive to the state of 3MI condensation, consistent with the previously reported sensitivity of I_1/I_2 to solvent polarity. The maximum value of the intensity ration (I_1/I_2 = 3.0) is observed for 3MI vapor, while the minimum value (I_1/I_2 = 0.43) is observed for 3MI in $CHCl_3$ solution. Implication of the present results for Raman analysis of hydrogen bonding states, hydrophilic interaction and hydrophobic interaction of tryptophan residues in proteins have been considered.

REFERENCES

1. J. Laane, K. Haller, S. Sakuri, M. Morris, D. Autrey, Z. Arp, W. Chiang, A. Combs. J. Mol. Struct. **650**, 57 (2003).
2. J. Laane in *Frontiers of Molecular Spectroscopy*, edited by J. Laane,, (Elsevier Publishing, Amsterdam, The Netherlands, 2008) pp. 63-132.
3. J. Laane, J. Phys. Chem. A, **104**, 7715 (2000).
4. J. Laane, Intl. Rev. in Phys. Chem., **18**, 301 (1999).
5. J. Laane in *Structure and Dynamics of Electronic Excited States*, edited by J. Laane, H. Takahashi, and A. Bandrauk, (Springer, Berlin, Germany, 1999) pp. 3-35.
6. J. Laane, Ann. Rev. Phys. Chem., **45**, 179 (1994).
7. J. Yang, M. Wagner, and J. Laane, J. Phys. Chem. A, **111**, 8429 (2007).
8. J. Yang, M. Wagner, and J. Laane, J. Phys. Chem. A, **110**, 9805 (2006).
9. J. Laane, E. Bondoc, S. Sakurai, K. Morris, N. Meinander, and J. Choo, J. Amer. Chem. Soc., **122**, 2628 (2000).
10. S. Lebowitz and J. Laane, J. Chem. Phys., **101**, 2740 (1994).
11. E. Cortez, R. Verastegui, J. Villareal, and J. Laane, J. Amer. Chem. Soc., **115**, 12132 (1993).
12. F. D. Chattaway and H. Irving, J. Chem. Soc., 2492 (1931).
13. M.J. Frisch, G.W. Trucks, H.B. Schlegel, G.E. Scuseria, M.A. Robb, J.R. Cheeseman, J.A. Montgomery, Jr., T. Vreven, K.N. Kudin, J.C. Burant, J.M. Millam, S. S. Iyengar, J. Tomasi, V. Barone, B. Mennucci, M. Cossi, G. Scalmani, N. Rega, G.A. Petersson, H. Nakatsuji, M. Hada, M. Ehara, K. Toyota,

R. Fukuda, J. Hasegawa, M. Ishida, T. Nakajima, Y. Honda, O. Kitao, H. Nakai, M. Klene, X. Li, J.E. Knox, H.P. Hratchian, J.B. Cross, V. Bakken, C. Adamo, J. Jaramillo, R. Gomperts, R.E. Stratmann, O. Yazyev, A.J. Austin, R. Cammi, C. Pomelli, J.W. Ochterski, P.Y. Ayala, K. Morokuma, G.A. Voth, P. Salvador, J.J. Dannenberg, V.G. Zakrzewski, S. Dapprich, A.D. Daniels, M.C. Strain, O. Farkas, D.K. Malick, A.D. Rabuck, K. Raghavachari, J.B. Foresman, J.V. Ortiz, Q. Cui, A.G. Baboul, S. Clifford, J. Cioslowski, B.B. Stefanov, G. Liu, A. Liashenko, P. Piskorz, I. Komaromi, R.L. Martin, D.J. Fox, T. Keith, M.A. Al-Laham, C.Y. Peng, A. Nanayakkara, M. Challacombe, P.M.W. Gill, B. Johnson, W. Chen, M.W. Wong, C. Gonzalez, and J.A. Pople, Gaussian 03, Revision C.02, Gaussian, Inc., Wallingford CT, 2004.

14. J. Yang and J. Laane, J. Mol. Struct., **798**, 27 (2006).

15. J. Laane, Appl. Spectrosc., **24**, 73 (1970).

16. J.Yang, Ph.D. Dissertation, Texas A&M University, 2006.

17. P. Carmona, Spectrochim. Acta A **36** 705 (1980).

18. S. Udo, J. Agr. Chem. Soc. Japan **12** 380 (1936).

19. J.F. Powell, R.E. Strange, J. Biochem. **54** 205 (1953).

20. E. Ghiamati, R. Mancharan, W. H. Nelson, and J.F. Sperry, Appl. Spectros. **46** 357 (1992).

21. A.A. Kolomenskii, S.N. Jerebtsov, T. Opatrny, H.A. Schuessler, M.O.Scully, J. Mod. Opt.**50** 2369 (2003).

22. A.A. Kolomenskii, H.A. Schuessler, Spectrochim. Acta A **61** 647 (2005).

23. H.F. Hameka, J.O. Jensen, J.L Jensen, C.N. Merrow, C.P. Vlahacos, J. Mol. Struct. **365** 131 (1996).

24. J.R. Xie, V.H. Smith, Jr., R.E. Allen, Chem. Phys. **322** 254 (2006).

25. F. Takusagawa, K. Hirotsu, A. Shimada, Bull. Chem. Soc. Jpn., **46** 2020 (1973).

26. V.C. Telléz, B.S. Gaytán, S. Bernès, E.G Vergara, Acta Crystallogr. C **58** o228 (2002).

27. G. Strahs, R.E. Dickerson, Acta Crystallogr. B **24** 571 (1968).

28. F. Takusagawa, K. Hirotsu, A. Shimada, Bull. Chem. Soc. Jpn., **46** 2292 (1973).

29. J.A. Cowan, J.A.K. Howard, G.J. McIntyre, S. M Lo, I.D. Williams, Acta Crystallogr. B **61**, 724 (2005).

30. W. Starosta, H. Ptasiewicz-Bąk, J. Leciejewicz, J. Coord. Chem., **55** 1 (2002).

31. W. Starosta, H. Ptasiewicz-Bąk, J. Leciejewicz, J. Coord. Chem., **56** 33 (2002).

32. D. Autrey, J. Laane, J. Phys. Chem., **105**, 6894 (2001).

33. D. Autrey, J. Choo, J. Laane, J. Phys. Chem., **105**, 10230 (2001).

34. D. Autrey, Z. Arp, J. Choo, J. Laane, J. Chem. Phys., **119** 2557 (2003).

35. D. Autrey, J. Yang, J. Laane, J. Mol. Struct., **661** 23 (2003).

36. D. Autrey, K. Haller, J. Laane, C. Mlynek, H. Hopf, J. Phys. Chem., **108** 403 (2004).

37. J. Yang, K. McCann, J. Laane, J. Mol. Struct., **695-696** 339 (2004).

38. C. Mlynek, H. Hopf, J. Yang, J. Laane, J. Mol. Struct., **742** 161 (2005).

39. A. Al-Saadi, J. Laane, J. Mol. Struct., **830** 46 (2007).

40. M. Z. M. Rishard, R. M. Irwin, J. Laane, J. Phys. Chem. A, **111** 825 (2007).

41. A.A. Al-Saadi and J. Laane, J. Phy. Chem. A, **111** 3302 (2007).

42. A.A. Al-Saadi and J. Laane, Organometallics, **27** 3435 (2008).

43. L. Wasylina, E. Kucharska, Z. Weglinski, A. Puszko, Chem. Heterocycl. Compd., **35** 186 (1999).

44. M. Berjot, J. Marx, A.J.P. Alix, J. Raman Spectrosc. **18**, 289 (1987)

45. J. Bandekar, Biochim. Biophys. Acta, **1120** 123 (1992).

46. J.C. Austin, T. Jordan, T.G. Spiro. *Biomolecular Spectroscopy, Part A*, edited by R.J.H. Clark, R.E. Hester (John Wiley and Sons, New York, 1993) pp 55-127

47. S.U. Sane, S.M. Cramer; T.M. Przybycien Anal.Biochem. **269**, 255 (1999)

48. R.C. Lord, N.T. Yu. J.Mol.Biol., **50**, 509 (**1970**).

49. M. N. Siamwiza, R. C Lord, M. C. Chen, T. Takamatsu,. I. Harada, H. Matsuura, T.Shimanouchi, Biochemistry **14**, 4870 (1975).

50. T. Miura, H. Takeuchi, I. Harada, Biochemistry **30**, 6074 (1991).

51. H. Li, G.J. Thomas,Jr., J.Am.Chem.Soc. **113**, 456 (1991).

52. S.W. Raso, P.L. Clark, C. Haase-Pettingell, J. King, G.J. Thomas,Jr., J.Mol.Biol. **307**, 899 (2001).

53. Z. Arp, D. Autrey, J.;Laane, S. A. Overman, G. J. Thomas, Jr., Biochemistry **40**, 2522 (2001).

54. H. Takeuchi, Biopolymers **72**, 305 (2003).

55. T. Miura, Subcell.Biochem. **24**, 55 (2003).

56. G. J. Thomas, Jr., Biopolymers **67**, 214(2002).

57. J. M. Benevides, S. A. Overman, G. J. Thomas Jr., *Current Protocols in Protein Science*, edited by J. E. Coligan, B. M. Dunn, H. L. Ploegh, D. W. Speicher, P. T. Wingfield, (2003) p 17.8.1-17.8.35.

58. H. Takeuchi, N. Watanabe, I. Harada, Spectrochim.Acta **44A**, 749 (1988).

59. S. A. Overman, K. L. Aubrey, N. S. Vispo, G. Cesareni, G. J. Thomas, Jr. Biochemistry **33**, 1037 (1994).

60. S. A. Overman, G. J. Thomas, Jr. Biochemistry **34,** 5440 (1995).

61. I. Harada, T. Miura, H. Takeuchi, Spectrochim.Acta **42**A, 307 (1986).

62. H. Takeuchi, H. Harada, Spectrochim.Acta **42**A, 1069 (1986).

63. T. Miura, H. Takeuchi, I. Harada, Biochemistry **27**, 88 (1988).

64. T. Miura, H. Takeuchi, I. Harada, J.Raman Spectrosc. **20**, 667 (1989).

65. S. K. Burley, G. A. Petsko, Adv.Protein Chem. **39**, 125 (1988).

66. J. P. Gallivan, D. A. Dougherty, Proc.Natl.Acad.Sci.US*A* **96**, 9459 (1999).

67. S. Bunte, G. Jensen, K. McNesby, D. Goodin, C. Chabalowski, R. Nieminen, S. Suhai, K. Jalkanen, Chem. Phys., **265** 13 (2001).

68. G. Jensen, D. Goodin, S. Bunte, J. Phys. Chem. **100** 954 (1996).

69. T. G. Spiro, *Biological Applications of Raman Spectroscopy. Volume 1: Raman Spectra and the Conformations of Biological Macromolecules,* (Wiley Interscience, New York, 1987).

70. S. Hashimoto, K. Obata, H. Takeuchi, R. Needleman, J. K. Lanyi, Biochemistry, **36** 11583 (1997).

71. S. Hashimoto, K. Obata, H. Takeuchi, R. Needleman, J. K. Lanyi, Biochemistry, **41** 6495 (2002).

72. J. L. Markley, A. Bax, Y. Arata, C. W. Hilbers, R. Kaptein, B. D.;Sykes, P. E. Wright, K. Wuthrich, J.Mol.Biol. **280** 933 (1998).

VITA

Kathleen Rae McCann received her Bachelor of Science degree in chemistry from Morningside College in Sioux City, Iowa in May of 2000. She entered the Chemistry Department at Texas A&M University in September of 2001 to begin her graduate studies. In November of that same year, she joined the research group of Dr. Jaan Laane.

Ms. McCann can be reached at the Department of Chemistry, Texas A&M University, College Station,TX 77843-3255.